

Computational Models for Design and Analysis of Compliant Mechanisms

A Dissertation
Presented to
The Academic Faculty

By

Chao-Chieh Lan

In Partial Fulfillment of the Requirements for the Degree of
Doctor of Philosophy in Mechanical Engineering

Georgia Institute of Technology

December 2005

Computational Models for Design and Analysis of Compliant Mechanisms

Approved by:

Dr. Kok-Meng Lee, Advisor
School of Mechanical Engineering
Georgia Institute of Technology

Dr. Aldo A. Ferri
School of Mechanical Engineering
Georgia Institute of Technology

Dr. Shreyes N. Melkote
School of Mechanical Engineering
Georgia Institute of Technology

Dr. Chen Zhou
School of Industrial and system Engineering
Georgia Institute of Technology

Dr. Bruce Webster
Department of Poultry Science
University of Georgia

Date Approved: 10/24/2005

[To my parents Kuo-Lien Lan and Chou-Mei Liao]

ACKNOWLEDGEMENTS

I would like to express my appreciation to those who supported me through my thesis research. First I would like to thank Dr. Kok-Meng Lee for giving me an opportunity to participate in this project. His inspiring advices and constant encouragement have so much influence on the accomplishment of my Ph. D. thesis. The most important thing that I learned from him is his philosophy on critical thinking and professional attitude. I would also like to thank him for giving me several chances to present my research topic in international conferences. Second, I would like to acknowledge the support and suggestions of my reading committee, Dr. Aldo A. Ferri, Dr. Shreyes N. Melkote, Dr. Chen Zhou, and Dr. Bruce Webster. I would like to give special thanks to Dr. Aldo A. Ferri. His lecture on variational methods is very helpful and gave me a lot of ideas in developing my thesis. Suggestions from Dr. Bruce Webster of the University of Georgia are greatly appreciated.

The author deeply appreciates the support of the GTRI staff Wiley Holcombe and Thomas Sean for system transportation and technical assistance. Most of the compliant structures are fabricated in the machine shop in MRDC building. I would like to thank Zi-Yen Ng for his assistance in programming the CNC code and Mati Chessin for finger bracket fabrication. Technical suggestions from machine shop staff, John Graham, Tommy, Jimmy, are also appreciated. I would like to extend my thankfulness to the following fellow students, Qiang Li, Hungson, Kuang-Ming Lee, and Yubin Chen, who give me valuable advices about my research.

Finally I would like to thank my parents Kuo-Lien Lan and Chou-Mei Liao, who

gave me support through all these years. My junior brother, Shau-Yu Lan, has accompanied me and gave me support on my research. I would like to express my deepest appreciation to my family.

This thesis research is funded by the research grants from US Poultry and Eggs Association (Project number USPE 446, USPE 381, ATRP N5410-430, -530, and -630). Equipment and experiment setup for the project are from the Georgia Agriculture Technological Research Program (ATRP).

TABLE OF CONTENTS

ACKNOWLEDGEMENTS	iv
LIST OF TABLES	ix
LIST OF FIGURES	x
LIST OF SYMBOLS	xiii
LIST OF ABBREVIATIONS	xvi
SUMMARY	xvii
CHAPTER 1 INTRODUCTION AND BACKGROUND	1
1.1 MOTIVATIONS AND BACKGROUND	1
1.2 PROBLEM DESCRIPTION AND OBJECTIVES	3
1.3 REVIEW OF PRIOR AND RELATED WORK	6
1.3.1 Compliant mechanism applications	6
1.3.2 Computational models for compliant mechanisms	11
1.3.3 Compliant contact problems.....	16
1.4 SUMMARY OF RESULTS.....	19
1.5 ORGANIZATION OF THIS DISSERTATION	19
CHAPTER 2 GENERALIZED SHOOTING METHOD	22
2.1 INTRODUCTION	22
2.2 FORMULATION OF GENERALIZED SM (GSM)	23
2.2.1 Unbounded Gauss-Newton method	26
2.2.2 Bounded Gauss-Newton method.....	28
2.3 APPLICATIONS TO COMPLIANT MECHANISMS.....	29
2.3.1 Governing equation of a flexible beam: <i>Initially straight</i>	30
2.3.2 Governing equation of a flexible beam: <i>Initially curved</i>	32
2.3.3 Beam as a member in a compliant mechanism	33
2.3.4 Formulation of constraint equations.....	34
2.4 NUMERICAL EXAMPLES	36
2.4.1 Compliant mechanisms with only initially straight links.....	38
2.4.2 Initially curved links.....	43

2.5 VERIFICATION OF GENERALIZED SM.....	46
2.5.1 Numerical verification.....	46
2.5.2 Experiment validation	50
2.6 CONCLUSIONS.....	52
CHAPTER 3 GLOBAL COORDINATE MODEL	54
3.1 INTRODUCTION	54
3.2 GLOBAL COORDINATE MODEL FOR COMPLIANT MECHANISMS.....	57
3.2.1 Global coordinate model (GCM) for a compliant link.....	57
3.2.2 Global coordinate model for serial compliant mechanisms	62
3.3 NUMERICAL APPROXIMATION	64
3.3.1 Temporal approximation: Newmark integration scheme.....	64
3.3.2 Spatial approximation: generalized multiple shooting method.....	66
3.3.3 Application to the global coordinate model	70
3.4 CONCLUSIONS.....	73
CHAPTER 4 ILLUSTRATIVE EXAMPLES AND VALIDATIONS.....	74
4.1 INTRODUCTION	74
4.2 ILLUSTRATIVE EXAMPLES.....	75
4.3 CONCLUSIONS.....	89
CHAPTER 5 DESIGN AND ANALYSIS USING GLOBAL COORDINATE MODEL	90
5.1 INTRODUCTION	90
5.2 GLOBAL COORDINATE MODEL FOR STATIC ANALYSIS.....	91
5.2.1 Governing equations for a link.....	91
5.2.2 Constraint (boundary) equations	94
5.2.3 Forward and inverse as a dual problem.....	96
5.3 FORWARD AND INVERSE ANALYSES	97
5.3.1 Forward and inverse models in state-space forms	97
5.3.2 Number of unknowns and constraint equations	98
5.4 ILLUSTRATIVE EXAMPLES AND APPLICATIONS	100
5.5 SOFTWARE DEVELOPMENT	105
5.6 A CASE STUDY: DESIGN AND OPTIMIZATION OF A COMPLIANT GRASPER	108
5.6.1 Shape optimization of a compliant link.....	109
5.6.2 Compliant grasper and experiment validations	112

LIST OF TABLES

Table 2.1 Clamped and pinned initial conditions	34
Table 2.2 Summary of unknown parameters in Examples 1 - 5	38
Table 2.3 Simulation parameters (uniform beam)	47
Table 2.4 Comparisons of computation time	49
Table 2.5 Experiment parameters (Aluminum beam, 6602-T6511)	51
Table 3.1 Constraint equations at a typical joint (1 to $\ell - 1$)	63
Table 3.2 Constraint equations at the 0^{th} joint	63
Table 3.3 Constraint equations at the ℓ^{th} joint	64
Table 4.1 Simulation parameters and values for a steel rod	75
Table 4.2 Simulation parameters and values for a spring steel rod	79
Table 4.3 Simulation parameters and values for the spinning rod	82
Table 4.4 Comparisons of global coordinate model and other models	82
Table 4.5 Simulation parameters and values for the compliant slider crank	84
Table 4.6 Parameters of the four-bar mechanism	86
Table 5.1 Number of constraint equations for a joint	98
Table 5.2 Unknowns for the forward and inverse problems	98
Table 5.3 Constraint equations for the double four-bar mechanism	103
Table 5.4 Polynomials that approximate the angle functions	104
Table 5.5 Constraint equations for the single four-bar mechanism	104
Table 5.6 Optimization problems and its corresponding variables	108
Table 5.7 Design variables for compliant grasper	111
Table 5.8 Optimal coefficients and required forces	112
Table 6.1 Simulation parameters and values	128
Table 6.2 Comparison of computation time	129
Table 6.3 Simulation parameters and values	131
Table 6.4 Comparison of computation time	131
Table D.1 Simulation parameters for the power series method	152

LIST OF FIGURES

Figure 1.1 Rigid-body (top) and compliant (bottom) mechanisms.....	2
Figure 1.2 Live bird transferring system.....	5
Figure 1.3 Applications of compliant mechanisms in MEMS.....	7
Figure 1.4 Flex-Foot products (Courtesy of Ossur).....	8
Figure 1.5 Biosensors.....	9
Figure 1.6 An EAP actuator placed between two electrodes.....	10
Figure 1.7 Grasping using EAP's	10
Figure 1.8 Snap-fits for micro assembly.....	17
Figure 2.1 Schematics of a series of compliant links.....	23
Figure 2.2 Schematics and coordinate systems of a flexible beam.....	31
Figure 2.3 A pair of connecting links	35
Figure 2.4 Illustrative examples.....	37
Figure 2.5 Numerical results for Example 1	39
Figure 2.6 Numerical results for Example 2	41
Figure 2.7 Deflection and contact forces for Example 3	42
Figure 2.8 Convergence result for Example 3	43
Figure 2.9 Planar spring mechanism.....	44
Figure 2.10 Force-displacement relationships	44
Figure 2.11 A compliant mechanism with initially curved links.....	45
Figure 2.12 Verification of GSM.....	48
Figure 2.13 %Error ($N=20$ for both FDM and FEM)	48
Figure 2.14 Experiment results	50
Figure 2.15 CAD model of the rotating indexer	51
Figure 2.16 Experiment setup	52
Figure 2.17 F - δY curve	52
Figure 3.1 Schematic of a compliant link	58
Figure 3.2 Schematic of an infinitesimal segment.....	58
Figure 3.3 A generic serial compliant mechanism.....	63
Figure 3.4 Multiple shooting method.....	68
Figure 4.1 Beam tip displacement in one cycle	76

Figure 4.2 Snapshot of a free-vibrating beam.....	76
Figure 4.3 Kinetic energy of the vibrating beam	77
Figure 4.4 Energy balance of the beam	77
Figure 4.5 Experiment setup	78
Figure 4.6 Period of a free vibrating steel rod	78
Figure 4.7 Experiment setup in Yoo <i>et. al.</i> [2003]	79
Figure 4.8 Comparison of simulation and experiment data with $m_0 = 20g$	80
Figure 4.9 Comparison of simulation and experiment data with $m_0 = 10g$	80
Figure 4.10 A spinning rod	81
Figure 4.11 The steady-state extension of the rod, 2.738×10^{-5} m.....	82
Figure 4.12 The displacement of the tip in the y direction	83
Figure 4.13 Compliant slider crank mechanism	83
Figure 4.14 Horizontal position of the slider block	84
Figure 4.15 Deformation of link 2	85
Figure 4.16 Initial four-bar mechanism configuration.....	85
Figure 4.17 Large deformations of the four-bar mechanism	87
Figure 4.18 Energy balance of the four-bar mechanism (GCM with $\Delta t = 0.001$).....	87
Figure 4.19 Internal forces at the joints	88
Figure 5.1 Generic compliant mechanisms.....	92
Figure 5.2 A joint that connects multiple links.....	92
Figure 5.3 The forward and inverse problems	96
Figure 5.4 Effect of shear on tip deflection with $\delta=0.2$	101
Figure 5.5 Effect of shear for link with large deflection ($E/G = 3$)	101
Figure 5.6 A compliant double four-bar mechanism	102
Figure 5.7 Deformed shape.....	103
Figure 5.8 Forward $F - \delta y$ curve	103
Figure 5.9 Deformed shape of a compliant mechanism	104
Figure 5.10 Original and deformed shape of the four-bar mechanism	105
Figure 5.11 Layout of the program	106
Figure 5.12 Compliant gripper.....	107
Figure 5.13 Compliant crimper [Saxena and Ananthasuresh, 2001]	107
Figure 5.14 Shortening effect of a link	109

Figure 5.15 Different initial shapes	110
Figure 5.16 Optimal grasper shapes.....	111
Figure 5.17 Grasping with compliant grasper.....	112
Figure 5.18 Experiment setup	113
Figure 5.19 Deformation of the grasper frame under different loads	113
Figure 5.20 Force-displacement relations.....	114
Figure 6.1 Compliant gripping contacts.....	117
Figure 6.2 Gripper assembly sequence	127
Figure 6.3 Simulation result of a gripper assembly ($\mu=0$)	128
Figure 6.4 Simulation result of a gripper assembly ($\mu=0.5$)	128
Figure 6.5 Simulation results from FEM	129
Figure 6.6 Schematics of a rotating gripper contacting an object.....	130
Figure 6.7 Snapshots of gripper-ellipse contact.....	131
Figure 6.8 Comparison of simulation results ($\mu=0$).....	132
Figure 6.9 Comparison of simulation results ($\mu=0.5$).....	132
Figure 6.10 Angle of rotation and shear angle at $x_e = -0.0254\text{m}$ and $\phi=108^\circ$	132
Figure C.1 Three dimensional link model	145
Figure C.2 XZX Eulerian angles	145
Figure C.3 Quasi-static grasping using compliant fingers.....	149
Figure D.1 Full circle bending of a cantilever beam	152
Figure D.2 A link under transverse load.....	153
Figure D.3 Quasi-static grasping using compliant fingers.....	153

LIST OF SYMBOLS

Upper case	Definition
A	Cross-sectional area
A_i	Cross-sectional area of the i^{th} link
A_ρ	Mass area
A_{ρ_i}	Mass area of the i^{th} link
E	Young's modulus
E_i	Young's modulus of the i^{th} link
E	Approximated value of e
G	Shear modulus
G_i	Shear modulus of the i^{th} link
H	Approximated values of reaction force h
I	Moment of inertia
I_i	Moment of inertia of the i^{th} link
I_ρ	Mass moment of inertia
I_{ρ_i}	Mass moment of inertia of the i^{th} link
K	Kinetic energy
L	Length of the link
L_i	Length of the i^{th} link
\mathbf{M}	Coefficient (mass) matrix of a set of ODE
M	Moment
N	Number of subdivisions of an integration interval
V	Potential (strain) energy or approximated values of internal force v
Lower case	Definition
e	Axial deformation
g	Constraint function

h	Internal force along the positive x direction
i	Index of the link
j	Index of the links connected to a floating joint
k	Index of joints
ℓ	Number of links
m	Number of unknown initial values
n	Number of 1 st order differential equations that govern the link
p	Number of terminal constraints
\mathbf{q}	A vector of state variables
q	State variables
r	Number of unknown parameters
s	Arc length
t	Time
u	Non-dimensional arc length
v	Internal force along the positive y direction
w	Number of links that connect to a floating joint or thickness of the finger
x	Global coordinate
y	Global coordinate
z	Global coordinate

Greek

Definition

E	Approximated value of e
Ψ	Approximated value of ψ
α	Angle of the force that applies at the tip of the link
ξ	Unknown parameters
σ	Damping ratio; Amplitude decay factor
θ	$\alpha + \psi$
ρ	Density
γ	Shear angle
κ	Shear correction factor

ν	Poisson's ratio
ψ	Angle of rotation
μ_u	Unknown initial values
η	Intrinsic curve function of a link

LIST OF ABBREVIATIONS

1-D	One dimensional
2-D	Two dimensional
3-D	Three dimensional
BFGS	Bryoden, Fletcher, Goldfarb, and Shanno
BVP	Boundary value problem
DAE's	Differential algebraic equations
FDM	Finite difference method
FEM	Finite element method
GCM	Global coordinate model
GSM	Generalized shooting method
GMSM	Generalized multiple shooting method
IVP	Initial value problem
NCO	Nonlinear constrained optimization
ODE's	Ordinary differential equations

SUMMARY

We consider here a class of mechanisms consisting of one or more compliant members, the manipulation of which relies on the deflection of those members. Compared with traditional rigid-body mechanisms, compliant mechanisms have the advantages of no relative moving parts and thus involve no wear, backlash, noises and lubrication. Motivated by the need in food processing industry, this paper presents the Global Coordinate Model (GCM) and the generalized shooting method (GSM) as a numerical solver for analyzing compliant mechanisms consisting of members that may be initially straight or curved.

As the name suggests, the advantage of global coordinate model is that all the members share the same reference frame, and hence, greatly simplifies the formulation for multi-link and multi-axis compliant mechanisms. The GCM presents a systematic procedure with forward/inverse models for analyzing generic compliant mechanisms. Dynamic and static examples will be given and verified experimentally. We also develop the Generalized Shooting Method (GSM) to efficiently solve the equations given by the GCM. Unlike FD or FE methods that rely on fine discretization of beam members to improve its accuracy, the generalized SM that treats the boundary value problem (BVP) as an initial value problem can achieve higher-order accuracy relatively easily.

Using the GCM, we also presents a formulation based on the Nonlinear Constrained Optimization (NCO) techniques to analyze contact problems of compliant grippers. For a planar problem it essentially reduces the domain of discretization by one

dimension. Hence it requires simpler formulation and is computationally more efficient than other methods such as finite element analysis.

An immediate application for this research is the automated live-bird transfer system developed at Georgia Tech. Success to this development is the design of compliant mechanisms that can accommodate different sizes of birds without damage to them. The feature to be monolithic also makes compliant mechanisms attracting in harsh environments such as food processing plants. Compliant mechanisms can also be easily miniaturized and show great promise in microelectromechanical systems (MEMS). It is expected that the model presented here will have a wide spectrum of applications and will effectively facilitate the process of design and optimization of compliant mechanisms.

CHAPTER 1

INTRODUCTION AND BACKGROUND

1.1 Motivations and Background

A mechanism, as defined by Reuleaux [1876], is an assemblage of resistant members, connected by movable joints, to form a closed kinematic chain with one link fixed and having the purpose of transforming motion. The purpose of a mechanism is to make use of its internal motions in transforming power or motion. Traditional mechanisms consist of rigid (non-deformable) members connected at movable joints. Actuators are applied at the joints to provide motion for rigid members. We refer these as rigid-body mechanisms. Examples include a reciprocating engine piston, a crane hoist, and a vice grip. Analyses of rigid-body mechanisms are well understood since closed form solution are available. However, there are many other applications where some of the members are intentionally designed to be relatively compliant compared with other members. We refer them as compliant mechanisms. As defined by Lobontiu [2002], a compliant mechanism is *a mechanism that is composed of at least one member (link) that is sensibly deformable (flexible or compliant) compared to other rigid links*. Figure 1.1 shows that a rigid-body mechanism (top) becomes a compliant mechanism (bottom) when the connecting rod is clamped at the sliding block.

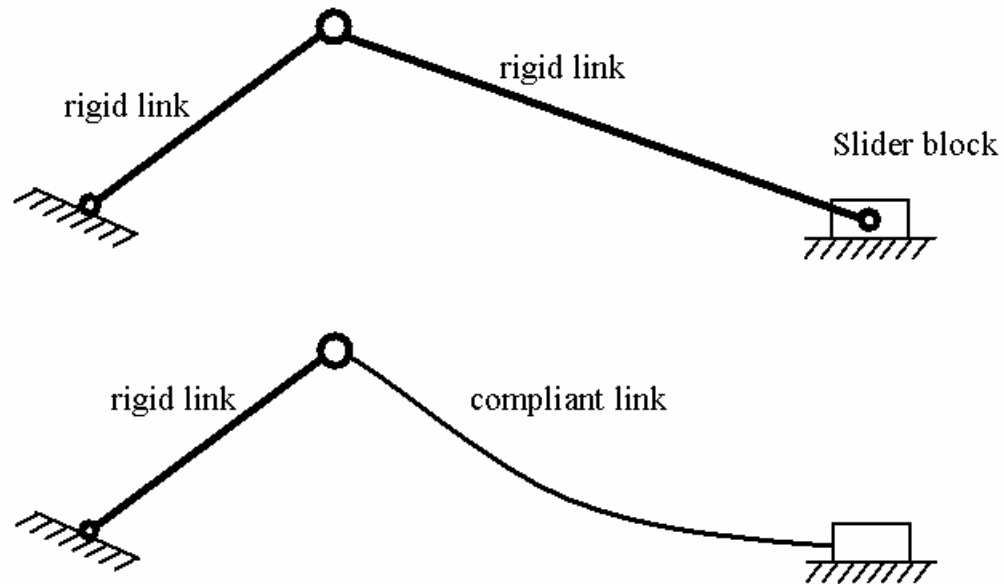


Figure 1.1 Rigid-body (top) and compliant (bottom) mechanisms

A compliant mechanism also transforms motion or power. Unlike rigid-body mechanisms, where actuations are applied at the joints connecting the rigid members, the manipulation of a compliant mechanism relies on the deflection of compliant members. The advantages of compliant mechanisms over rigid-body mechanisms include:

- (1) There are no relative moving parts and thus involve no wear, backlash, noises and lubrication. They are relatively compact in design and can be manufactured from a single piece to provide a monolithic mechanism.
- (2) Displacements and forces are smooth and continuous at all levels.

A specific application of compliant mechanisms is handling of live birds that come in a limited range of different sizes and shapes. In order not to cause damage to the birds, handling must be performed with care. While rigid-body mechanisms require actuators and sensors to manipulate live objects, the use of compliant mechanisms greatly

reduces the number of actuators and sensors needed and at the same time minimizes the damage.

The survey by Lee *et al.* [1996] shows that rubber fingers have been used for handling live birds over the past two decades. Among them are a singulating system developed by Berry *et al.* [1993] and a pickup system proposed by Briggs *et al.* [1994]. The rubber fingers were further explored by Lee *et al.* [1999] to position the bird for shackling and transferring. In order to design compliant fingers for transferring live bird, Joni [2000] performed a finite element analysis to predict the static contact force between compliant fingers and the live object. Yin [2003] studied the dynamical effect of high speed grasping of live birds. The study by Joni and Yin has verified that (1) the quasi-static model is sufficient to predict the contact force and (2) the bird is relatively rigid compared with soft fingers so that it can be treated as a rigid body.

Motivated by the previous work that use compliant fingers for handling and transferring live birds, the goal of this thesis is to develop a systematic yet general formulation and extend the analysis to general mechanisms so that it that can facilitate design and analysis of compliant mechanisms.

1.2 Problem Description and Objectives

With the emerging applications of compliant mechanisms, there is a need for developing a systematic formulation for design and analysis of compliant mechanisms. Although existing methods such as finite element method are widely available, there remain challenges in the computational model of compliant mechanisms:

- Many existing models are either inadequate to capture the geometric nonlinearity or too complicated that can not serve as basis for compliant mechanism design and optimization.
- There is not a single formulation that can directly deal with forward and inverse problems of compliant mechanisms.
- Compliant gripping problems, where manipulation of objects requires deflection of grippers, generally require intensive computation.

With the challenges stated above, the objectives of this thesis are to

- (1) Develop an efficient numerical solver to simulate the force-displacement relationships of compliant mechanisms.
- (2) Based on the solver in (1), develop a general forward/inverse model with systematic formulations for design and analysis of general compliant mechanisms.
- (3) Develop a numerical technique that can greatly facilitate the analysis of compliant grippers.

Throughout this thesis, we consider compliant mechanisms with the following characteristics:

- Since most compliant mechanisms are designed for planar manipulation, we focus in this thesis two dimensional problems. In other words, the compliant member can only bend in one direction. We expect that the outcome of this research can be extended to three dimensional problems as well.
- The compliant member is assumed to operate in the linear strain-stress range. Nonlinear elastic and plastic deformation are not considered here.

An immediate application of this research is to design a novel compliant live bird transfer system that can accommodate birds with various sizes and shapes. As shown in

Figure 1.2, the system consists of ten compliant fingers, four compliant graspers, and two compliant indexers.

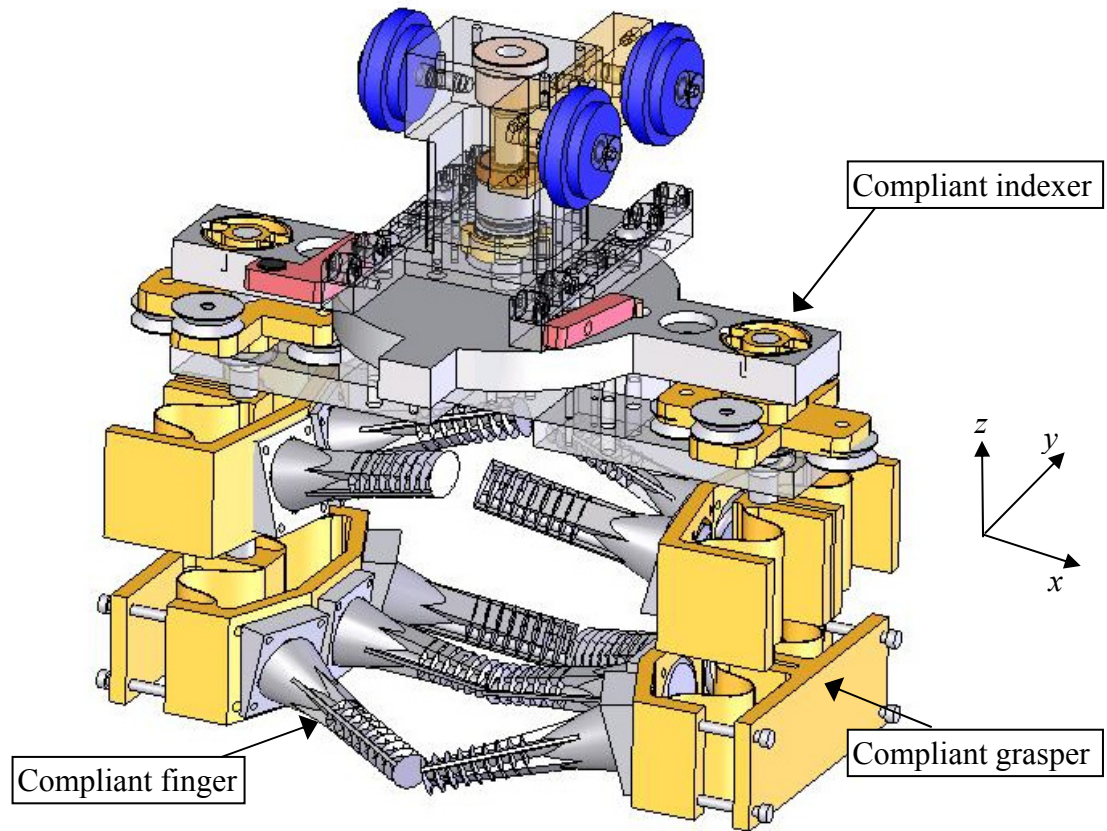


Figure 1.2 Live bird transferring system

The bird is supported between a pair of “compliant hands” that moves in the y direction. Each hand consists of lower fingers, upper fingers and two compliant graspers, whose functions are stated as follows:

- (1) The three lower fingers support the weight of the bird while transferring.
- (2) The two upper fingers prevent the bird from flapping and escaping the hands. Both the upper and lower fingers are designed to accommodate with a limit range of bird sizes in the z direction.
- (3) Compliant graspers are designed to accommodate with a limit range of bird sizes in the x direction.

In addition, the two compliant indexers are used to position a shaft that rotates the compliant grasper in the z direction every 90 degrees. They are compact in size and can replace traditional actuators. As will be shown, the proposed model can greatly simplify the design and analysis of these compliant mechanisms.

1.3 Review of Prior and Related Work

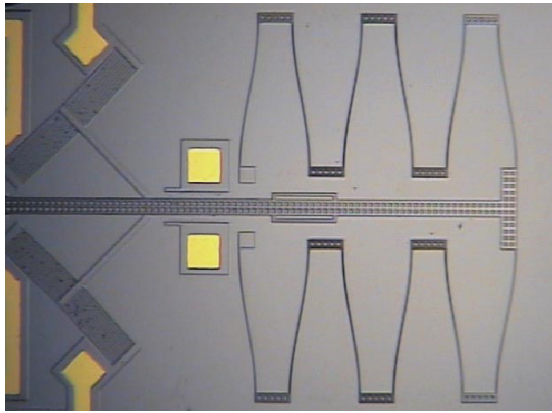
The literature review is divided into three parts. First we introduce applications then computational models for compliant mechanism. Finally, the compliant grippers, a special but important class of compliant mechanisms, will be reviewed.

1.3.1 Compliant mechanism applications

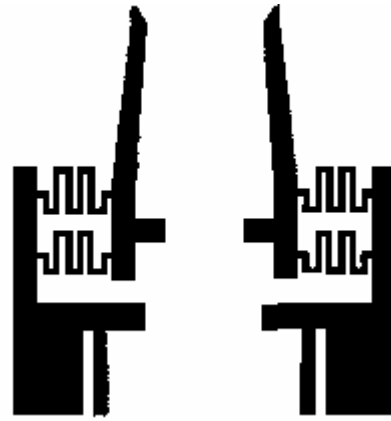
The idea of using compliant members to store energy and create motion has appeared thousands of years ago. Bows have been used as the primary weapon and hunting tools in many ancient cultures. Catapults are another example of early use of compliant mechanisms. Even nowadays we see compliant mechanism everywhere in our lives, such as binder clip, nail clipper, and snap-fits. In the following we introduce the applications in mechanical and biomechanical engineering areas.

Compliant mechanisms in mechanical applications

With the advance of manufacturing technology, compliant mechanisms have numerous applications in robotics/automation such as high precision manipulation [Lee and Arjunan, 1991], constant-force end effector [Evans and Howell, 1999], and micro electromechanical systems (MEMS). Figure 1.3(a) shows a series of compliant parallel mechanisms (also named serpentine) for linear motor drive [Maloney *et al.*, 2004] and Figure 1.3(b) shows a micro compliant gripper [Lee *et al.*, 2003].



(a) Serpentine



(b) Micro gripper

Figure 1.3 Applications of compliant mechanisms in MEMS

The reduction in the number of parts and joints offered by compliant mechanisms is a significant advantage in the fabrication of MEMS. Micro compliant mechanisms may be fabricated using technology and materials similar to those used in the fabrication of integrated circuits. Additional applications of compliant mechanisms in macro and micro scale can be found in [Howell, 2001] and [Lobontiu, 2002].

Compliant mechanisms in biomechanical applications

Motivated by the successful application of compliant mechanisms in robotics and automation, its extension to biomechanics are now emerging and several cutting-edge research topics are currently been studied. We introduce some of these topics in the following sections.

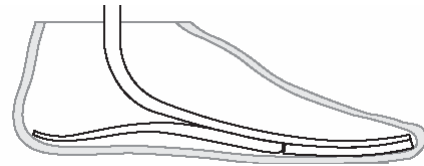
Flex-Foot

As shown in Figure 1.4, Flex-Foot was first introduced in 1984 by prosthetic user and research inventor Van Phillips. The advantages of Flex-Foot over conventional prosthetic feet are its light weight and compliance. Two critical breakthroughs made this product unique and revolutionized the everyday aspirations of amputees. First, energy

storage and release, is a function inherent in the patented carbon fiber design of Flex-Foot. Second, vertical shock absorption enables a more natural gait and protects the sound limb and remaining joints of the amputated limb from excessive shock. Today different functions are available within the Flex-Foot range to suit individual needs.



(a) Flex-Foot for running



(b) Side view



(c) Vari-Flex

Figure 1.4 Flex-Foot products (Courtesy of Ossur)

Biosensors

Micro cantilever beams have recently found their applications in the bio-medical research area. Wu *et al.* [2001] developed a cantilevered microscopic chip to detect prostate specific antigen (PSA) in human blood. As PSA sticks to the antibodies, the cantilevered chip bends like a diving board as shown in Figure 1.5(a), where the left cantilever bends as the protein PSA binds to the antibody. The other cantilevers, exposed to different proteins found in human blood serum (human plasminogen (HP) and human serum albumin (HSA)), do not bend because these molecules do not bind to the PSA antibody. The cantilevers themselves are about 50 microns wide (half the width of a human hair), 200 microns long (a fifth of a millimeter), and half a micron thick. The

micro-cantilever technique has applications beyond prostate cancer. Any disease, from breast cancer to AIDS, with protein or DNA markers in blood or urine could conceivably be assayed by arrays of these micro-cantilevers.

Another application of micro cantilever beams is shown in Figure 1.5(b). The array of micro cantilever beams, coated with a monolayer of edox-controllable [Huang, 2004] rotaxane molecules, undergoes controllable and reversible bending when it is exposed to chemical oxidants and reductants. Conversely, beams that are coated with a redox-active but mechanically inert control compound do not display the same bending. The capability of transferring chemical energy to mechanical energy in this micro cantilever has potential of reduced scale operations compared with traditionally micro scale actuators.

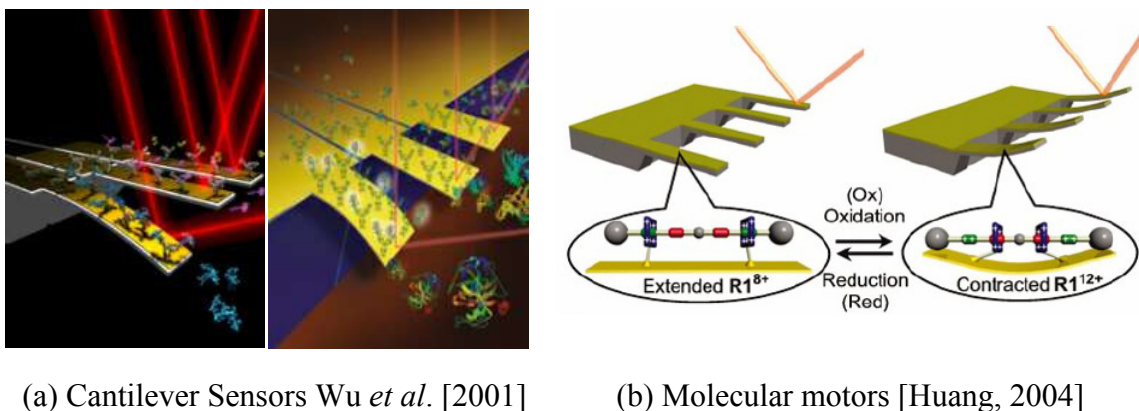


Figure 1.5 Biosensors

EAP as Artificial Muscles

As shown in Figure 1.6, Electroactive polymers (EAP) are large motion actuators that exhibit large bending deformation in response to electrical stimulation. They are divided into electronic (driven by electric field) and ionic (driven by diffusion of ions) EAPs [Bar-Cohen, 2004]. Electronic EAPs require high activation voltage ($\sim 150\text{V}/\mu\text{m}$) but they can sustain DC driven voltages and operate in air. Ionic EAPs, on the other hand,

require as low as 1~5V but cannot sustain DC driven voltage and must maintain their wetness. Compared with shape memory alloy and electroactive ceramics, EAP materials are superior in high actuation strain, low density and low drive voltage [Bar-Cohen, 2004].

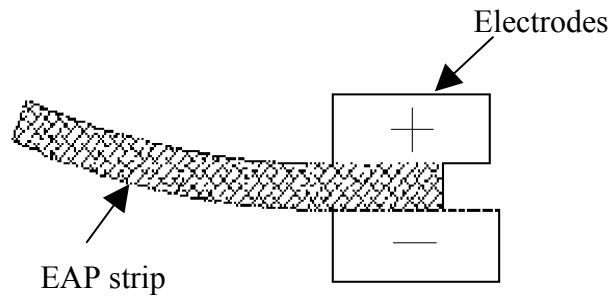
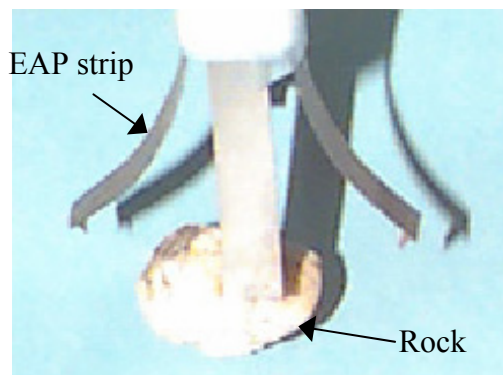


Figure 1.6 An EAP actuator placed between two electrodes

With the advantages stated above, EAPs have drawn attention in biomechanics because they can match the force and energy density of biological muscles. Various robotic applications using EAP have been developed. As shown in Figure 1.7, Shahinpoor *et al.* [1998] used EAP strips as multi-finger grippers for picking approximately 10 gram rocks.



(a) Actuated EAP



(b) Relaxed EAP

Figure 1.7 Grasping using EAP's

In addition, Nakabo *et al.* [2005] implemented a swimming robot using ionic EAP. Yamakita *et al.* [2005] developed a biped walking robot using ionic EAP. Although EAP appears as a cutting-edge material for actuation, there are still challenges need to overcome before transition to real applications [Bar-Cohen *et al.* 1999].

1.3.2 Computational models for compliant mechanisms

With the emerging technology utilizing compliant members, we introduce state-of-the-art computational models for design and analysis of compliant mechanisms. First we introduce static models and second dynamic models.

Static Analysis of Compliant Mechanisms

Four methods are commonly used to analyze a compliant mechanism; namely, elliptical integrals, finite element method (FEM), chain algorithm, and the pseudo-rigid-body model. The geometrical solution to the 2nd order, nonlinear differential equation that characterizes the large deflection of flexible beams can be found in [Frisch-Fay, 1962] but the derivation of the *elliptical integrals* is rather cumbersome and is useful for beams with relatively simple geometry, (see for example, [Mattiasson, 1981]). *FEM* can deal with complicated geometric shape by discretizing elastic members into small elements but the accuracy depends on the resolution of discretization. For nonlinear analysis, the formulation is often complicated with time-consuming computation. The *chain algorithm* [Hill and Midha, 1990] also discretizes the elastic member into small linearized elements. Unlike FEM, the elements in the chain algorithm are analyzed in succession and hence, the inversion of overall stiffness matrix is avoided. Shooting methods are then used to satisfy boundary conditions. However, the accuracy of the results computed using the chain algorithm still depends on the resolution of the discretization. The *pseudo-rigid-*

body model [Howell, 2001] finds the equivalent spring stiffness of a flexible link by means of approximation functions. The beam is then decoupled into a torsional spring and a rigid link. Thus this model essentially extends the rigid-body analysis to find the end-point deflection of a flexible link by approximating closed-form elliptical-integral solutions. However it is restricted to linear material properties and unable to predict the deflected shape of the entire link.

The fundamental member of a compliant mechanism is a flexible beam (where the axial dimension is much larger as compared to those in the cross-section). More recently, Yin *et al.* [2004] evaluated three numerical methods for computing the deflected shape of a flexible beam against the exact closed-form solution [Frisch-Fay, 1962] for a uniform beam; shooting method (SM), finite difference method (FDM), and FEM. The SM calculated shape (with “ode45” in MATLAB) perfectly matches the exact solution with only a few iterations. The results demonstrate that the SM has some advantages over FDM and FEM in solving the large-deflection beam equation; SM formulation is simple because it does not rely on discretization of compliant links and as a result, it is relatively easy to achieve higher order accuracy with incremental computational effort. In addition, SM can deal with unusual boundary conditions (for example, BC’s involve derivatives) without using approximation that often limits FDM. For design synthesis of mechanisms, it is superior to lumped-parameter methods (such as pseudo-rigid-body model) in that it can analyze compliant mechanisms with links of nonlinear material properties. These provide us the motivation to develop a generalized SM for analyzing compliant mechanisms.

The shooting method was originally suggested by Keller [1968]. By guessing the unknown initial values and then integrating the ODE’s, the SM “shoots” at the terminal

values iteratively until convergence. Like solving nonlinear equations, two major concerns of SM are the need for the reasonably close guesses and the convergence of solutions. Multiple-SM has been developed by Keller [1968] and Stoer *et al.* [1980] to overcome convergence problems, which divides the interval of independent variable into small subdivisions and then performs SM on each of the subdivisions such that after pieced together, the solution is continuous. Another technique is modified SM [Holsapple *et al.*, 2003] which shoots at intermediate values in succession until terminal value. A major application of SM has been the analysis of structural members. Wang *et al.* [1992] analyzes rectangular frames and circular rings using shooting-optimization techniques. Pai *et al.* [1996] use multiple-SM to solve the problem of flexible beams undergoing large 3-D deflections. Goh *et al.* [1991] extends shooting method to solve BVP with unknown eigenvalues. Most of these research efforts focused on the use of SM for solving the deflected shape of only one beam. Its use for analyzing compliant mechanisms with multiple beams remains under-exploited.

Dynamic Analysis of Compliant Mechanisms

Dynamic analyses of compliant mechanisms have been a subject of interest for simulation and control of flexible mechanical systems. Examples include space robot arms and high-speed robotic manipulators. These dynamic models are often based on the assumption of small deflection without considering shear deformation. This assumption is satisfactory provided that the link undergoes a small deflection such that the theory of linear elasticity holds. However, for mechanisms involving highly compliant links (such as rubber fingers in [Lee, 1996], light-weight arms, and high-precision elements), the effects of large deflection with shear deformation on the link motion cannot be ignored. In order to predict more accurately the deflected shape during transient, there is a need to

model the dynamics that capture the deflection of a compliant link.

In the last two decades, several approaches have been developed to analyze compliant links undergoing large deflection and overall rotation. Javier [1994] has divided this research field into three groups. The first is the *simplified elasto-dynamic method* originally proposed by Winfrey [1971]. This approach assumes that small deformation does not affect rigid body motion in order to decouple the rigid body motion from the link deformation. The second is the *floating frame method* based on defining the deformation relative to a floating frame which follows the rigid body motion of the link (see for example, [Laskin *et al.*, 1983] and [Book, 1984]). This method makes use of linear finite element (FE) theory since reliable FE packages are widely available. Although this method can account for shear deformation, the deflection is assumed to be small in order for the linear theory of elasticity to hold. The third is the *large rotation vector method* [Simo and Vu-Quoc, 1986] based on defining the overall motion plus deformation with respect to the inertial frame. Unlike the floating frame method, this method allows large deflection of the compliant link. As a result, nonlinear FE method (FEM) has to be used. This method, when solved using FEM, can lead to excessive shear forces known as shear locking [Bathe, 1996] as pointed out by Shabana [1998].

With the recent development of finite element software, two other popular methods capable of large deflection analysis are often used, namely the corotational procedure and the absolute nodal coordinate formulation. In the following paragraphs we introduce these two methods in more detail.

Corotational procedure

The corotational procedure was first presented by Rankin and Brogan [1986] and has been used by finite element software such as ANSYS. It has been

used to analyze many structural problems with large rotations. This procedure is independent of the element formulations used. Both the element and its nodes are attached with their own local coordinate frames. These frames are used to subtract the rigid body motion from the global displacement field to obtain the deformation of the element. Hsiao and Jang [1991] extended the corotational procedure to analyze flexible planar linkages using linear beam theory. Behdinan [1998] used the corotational procedure to study planar beams undergoing large deflections. Although this procedure is widely used by finite element software, Campanelli *et al.* [2000] pointed out the main restrictions as follows:

- (1) Local rotation of end sections has to be less than 30°
- (2) Small time/load steps

Absolute nodal coordinate formulation

The absolute nodal coordinate formulation [Shabana, 1998] is based on the finite element method. Compared with the floating frame or reference formulation, the element nodal coordinates are now defined in the inertia frame. Global slopes are also used instead of infinitesimal or finite rotations. These nodal coordinates and slopes are used with a global shape function that has a complete set of rigid body modes. This is an advantage over classical finite element formulations which do not describe an exact rigid body displacement [Shabana, 1996]. The resulting mass matrix of this formulation is constant. However, the trade-off is that the stiffness matrix and elastic forces are highly nonlinear.

This formulation has been extended to solve three dimensional beam problems [Shabana, 2001] and plate problems [Mikkola, 2001]. The comparison

between corotational method and the absolute nodal coordinate formulation can be found in [Campanelli *et al.*, 2000].

1.3.3 Compliant contact problems

Mechanical grippers have many applications in high-speed production automation. A typical robotic gripper with two or more rigid fingers is often actuated by an electrical or a pneumatic motor. Unlike grippers with rigid fingers, a compliant gripper is capable of large flexural deflection and is manipulated primarily by means of its contact with the object being handled rather than solely by an external actuator. The concept of compliant gripping has been widely used for snap-fit assembly. Bonenberger [2000] has a comprehensive description on design of snap-fit assembly. Lee *et al.* [1996] designed the compliant rubber grippers for singulating broilers for poultry meat production, and later [1999] exploited their application as graspers to automate transferring of live birds. As a compliant gripper requires no external actuators and sensors for feedback to accommodate a limited range of shapes/sizes of the live objects, it has been more attractive than traditional grippers for high-speed automation. In addition, compliant grippers are easy to fabricate, assemble, and maintain.

Advance in MEMS has realized the need for mass production of micro components. Various micromachining methods have been developed, such as IC-based silicon processing, LIGA, surface machining, and micro electro discharge machining (EDM). However, these techniques are only capable of two-dimensional (2-D) fabrication. In order to create broader applications based on MEMS devices, it is required to develop microgrippers for manipulating and assembling micro components for 3-D applications. The interest to reduce the complexity of 3-D assembly has motivated the

development of passive microgrippers. As compared to active microgrippers which may be driven by means of electro-thermal [Salim *et al.*, 1997], electrostatic [Kim *et al.*, 1992], electromagnetic [Suzuki, 1996] or piezoelectric [Ansel *et al.*, 2002] actuators, passive micro-grippers requiring no external actuators rely on contact between compliant fingers and the micro component to generate motion required for assembly; for examples, a micro-machined end-effector for MEMS assembly [Tsui *et al.*, 2004], a micro transformer [Dechev, 2004] shown in Figure 1.8(a), and a compliant microgripper for micro snap-fit connector [Oh *et al.*, 2003] shown in Figure 1.8(b).

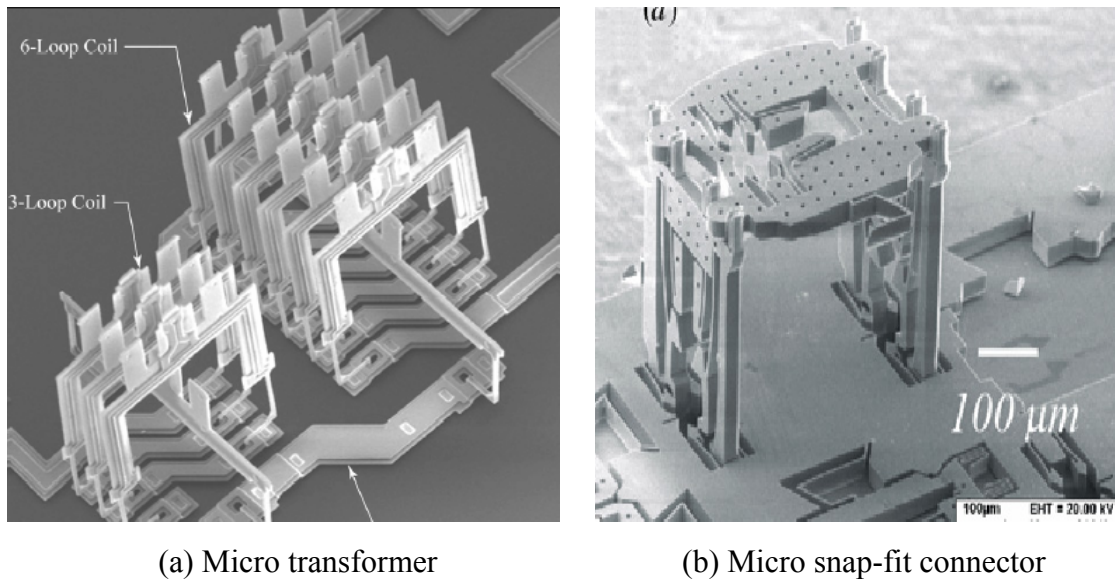


Figure 1.8 Snap-fits for micro assembly

Since uncertain actuator displacement does not exist in passive microgrippers, they have significant potential for very high precision applications. However, design of a compliant gripper is more challenging due to the difficulty in predicting the contact-induced deflection of its fingers.

Compliant fingers undergo large deflection when they contact the object. The essence of the analysis is to determine the normal and tangential contact forces that must

satisfy the boundary conditions at the interface. Since most contact problems involving large deformation do not permit analytical solutions, designers have resorted to the following two solutions.

Simple closed-form solution based on classical beam theory

Bayer Corporation [1996] and AlliedSignal Corporation [1997] have both provided guidelines for determining contact forces based on simple beam bending theory. Using these guidelines, Oh *et al.* [1999] developed a Java™-based calculator for designing snap-fits. The above solution is easy to use and provides designers quick results. However, it is limited to small deflection with simple contact geometry and uniform cantilever cross-sections.

Numerical methods for approximation solutions

Among them, the *matrix inversion method* satisfies boundary conditions at specified matching points. It has been used by Paul & Hashemi [1981] to calculate normal contact forces. Another method, the *variational inequality method*, determines the shape and size at contact by using well-developed optimization techniques. Fichera [1964] and Duvant & Lions [1972] have investigated on the existence and uniqueness of solution to contact problems. They show that the true contact area and surface displacement are those that minimize the total strain energy. From a numerical perspective, Kalker and van Randen [1972] formulate the minimization problem as a quadratic programming problem to solve frictionless non-Hertzian contact problems. The above two methods are based on the elastic half-space model [Johnson, 1987] so that linear elasticity theory holds. For contact problems involving large deformation such as compliant grippers, a more general approach, the *finite element method* (FEM), is widely used. However, its formulation is complicated and often requires intensive computation. Yin and Lee [2002] proposed a

numerical solver based on elliptical integrals to solve the problem of a large-deflected gripper contacting an elliptic object. By assuming only one contact point exists, the results agree well with those obtained by using FEM with less computation time. However, the solver models the gripper as a 1-D segment without considering the thickness of the finger. Hence it is not applicable to thick fingers.

1.4 Summary of Results

The contributions made in this dissertation are briefly summarized as follows:

- (1) The generalized shooting method is developed to serve as the computation basis for analyzing compliant mechanisms. The GSM is shown to be able to achieve higher order accuracy easily.
- (2) We develop the global coordinate model to provide systematic procedures for analyzing compliant mechanisms. This model captures bending, shear, and axial deformation of a compliant link at the same time. Compared with corotational procedure or floating frame formulation, the global coordinate model requires only the inertia frame and hence no coordinate transformation matrices are needed.
- (3) We proposed an efficient numerical technique to facilitate design and analysis of compliant grippers. This technique essentially reduces the dimension of discretization by one, and hence, is significantly faster than finite element method without losing accuracy.

1.5 Organization of This Dissertation

The reminder of this thesis is organized as follows. We start in Chapter 2 with the development of generalized shooting method for solving systems of boundary value

problems. We use Frisch-Fay's model as an illustration to demonstrate the application of generalized shooting method for analyzing compliant mechanisms. The generalized shooting method will be the basis for analyzing general compliant mechanisms in Chapters 3 and 5.

In Chapter 3, the global coordinate model will be developed to analyze the dynamic response of serial compliant mechanisms with numerical and experimental verifications performed in Chapter 4.

Chapter 5 presents the static analysis of compliant mechanisms using global coordinate model. Systematic procedures will be given to model general compliant mechanisms. Both forward and inverse examples will be given. A program will also be developed to allow graphical user interface. We post a case study at the end of Chapter 5 to illustrate the application of the global coordinate model.

Based on the global coordinate model, Chapter 6 will develop a gripping contact model for analyzing compliant grippers. The nonlinear constrained optimization technique will be applied to solve the model. As will be demonstrated, the technique can significantly improve the simulation of compliant gripping problems. Two types of gripping contact problems will be considered, namely direct and indirect contact. Numerical examples will be given to compare with the results of using finite element software.

Figure 1.9 shows the flow of this thesis. Specifically, two numerical solvers will be proposed. They respectively solve two different boundary conditions of compliant mechanisms (revolute/clamped and contact) that can be described by global coordinate model and compliant gripping model.

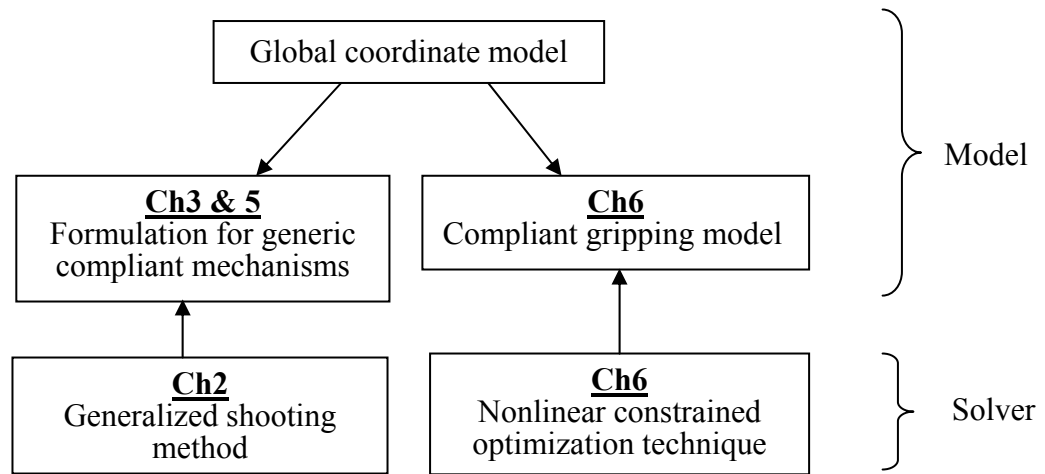


Figure 1.9 Flow chart of thesis

Finally, the conclusions and recommendations of the thesis are presented in Chapter 7. Several aspects of potential future work are addressed to increase the applicability of the analysis and modeling discussed in this thesis, and to facilitate the design of compliant mechanisms.

CHAPTER 2

GENERALIZED SHOOTING METHOD

2.1 Introduction

As mentioned in Subsection 1.3.2, several numerical methods have been previously compared for analyzing a large deflected compliant member. The shooting method (SM) has been demonstrated to have superior performance compared to its counterparts. This chapter extends the shooting method for analyzing compliant mechanisms. We organize the remainder of this chapter as following:

1. We generalize the SM for solving two-point BVP and extend it to analyze compliant mechanisms with distributed-parameter models.
2. Two numerical algorithms are given to implement generalized SM; namely, unconstrained Gauss-Newton method and constrained Gauss-Newton method.
3. We illustrate with five examples the formulation of the generalized SM for a broad spectrum of applications.
4. The numerical method will be validated by comparing against experiment results, and those obtained with using other methods; close-form solution, FEM, and FDM whenever possible. Advantages over FEM and FDM are also highlighted.

Note that the formulation introduced in this chapter will serve as the computation basis for the analytical models developed in Chapters 3 and 5.

2.2 Formulation of Generalized SM (GSM)

Consider a chain of compliant links connected together as shown in Figure 2.1 (either open-loop or close-loop). Each link is governed by n 1st order ordinary differential equations (ODE's) $\mathbf{q}'_i = \mathbf{f}_i$ with normalized independent variable u_i . As will be shown later in the examples, the variable u_i can be the axial coordinate or the path-length variable normalized to the length of the link. We are interested in the problem of a compliant mechanism where one or more of the links are connected to a fixed frame (or ground). The links can then be formulated as a system of ℓ coupled, normalized sets of 1st order nonlinear ordinary differential equations (ODE's):

$$\begin{bmatrix} \mathbf{q}'_1 \\ \vdots \\ \mathbf{q}'_\ell \end{bmatrix} = \begin{bmatrix} \mathbf{f}_1(u_1, \mathbf{q}_1, \boldsymbol{\xi}_1) \\ \vdots \\ \mathbf{f}_\ell(u_\ell, \mathbf{q}_\ell, \boldsymbol{\xi}_\ell) \end{bmatrix} \quad (2.1)$$

where $\mathbf{q}'_i = d\mathbf{q}_i / du_i$;

$0 \leq u_1, \dots, u_\ell \leq 1$ are independent variables;

$\mathbf{q}_i = [q_{i1} \ q_{i2} \ \dots \ q_{in}]^T$ is the state vector, $i = 1, \dots, \ell$; and

$\boldsymbol{\xi} = [\boldsymbol{\xi}_1^T, \boldsymbol{\xi}_2^T, \dots, \boldsymbol{\xi}_\ell^T]^T$ is a vector of r unknown parameters. As will be illustrated in the examples in Section 2.4, these unknown parameters provide the coupling among the ℓ sets of ODE's.

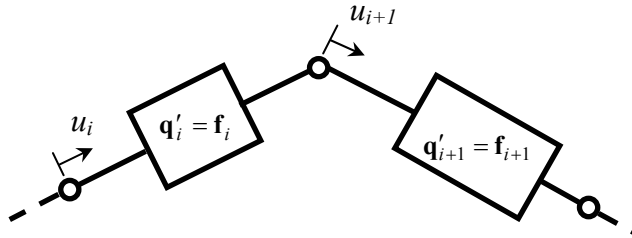


Figure 2.1 Schematics of a series of compliant links

Equation (2.1) is subject to the initial and terminal values (BV's) denoted as

$$\mathbf{q}(\mathbf{u} = 0) = \boldsymbol{\mu} \text{ and } \mathbf{q}(\mathbf{u} = 1) = \boldsymbol{\eta}$$

where $\mathbf{q} = [\mathbf{q}_1^T, \mathbf{q}_2^T, \dots, \mathbf{q}_\ell^T]^T$ is an $n \times \ell$ vector. We consider here a class of problems where only some of the initial values are known. The m unknown initial values of $\mathbf{q}(\mathbf{u}=0)$ are denoted by an $m \times I$ unknown vector $\boldsymbol{\mu}_u$. It is worth noting that *the original formulation in the conventional SM does not involve unknown parameters* and thus, can only deal with a special case of Equation (2.1) where all the parameters (ξ 's) are known.

SM transforms a boundary value problem (BVP) to an initial-value-problem (IVP). It generally requires making guesses on the unknown initial values $\boldsymbol{\mu}_u$ in order for the nonlinear ODE's to be solved. Since $\boldsymbol{\xi}$ is an unknown vector, additional guesses on the values of the parameters are also needed. These guesses must together satisfy two sets of constraints after solving the ODE's; namely, the terminal constraints and the physical constraints. In order to solve this class of problems, these constraints must together form $r+m$ nonlinear algebraic equations after integrating the ODE's. They are expressed mathematically in Equations (2.2a) and (2.2b):

Constraint Set I: Satisfying (known) terminal constraints

$$g_i(\boldsymbol{\mu}_u, \boldsymbol{\xi}) = \sum_{j=1}^n c_{ij} \eta_j^*(\boldsymbol{\mu}_u, \boldsymbol{\xi}) + d_i = 0, \quad i = 1, 2, \dots, p \quad (2.2a)$$

where the function $\eta_j^*(\cdot)$ calculates the j^{th} terminal values η_j for any given $\boldsymbol{\mu}_u$ and $\boldsymbol{\xi}$; c_{ij} and d_i are constant coefficients.

Constraint Set II: Satisfying (known) physical constraints

$$g_i(\boldsymbol{\mu}_u, \boldsymbol{\xi}) = 0, \quad i = p + 1, p + 2, \dots, r + m \quad (2.2b)$$

Note that similar constraint sets has been proposed by Goh *et al.* [1991]. However, their formulation only consists of one set of ODE's in Equation (2.1), which is a special case of the GSM presented here. It is assumed that the solution of the BVP represented by Equations (2.1) and (2.2) exists and is unique. For the existence and uniqueness theorem of BVP, please refer to Stoer *et al.* [1980].

A general system of nonlinear algebraic equations (NAE) requires that the number of initial guesses equals the number of nonlinear equations. The BVP, Equations (2.1) and (2.2), shares this property and can be treated as implicit NAE. Numerical solvers for NAE can thus be used to solve the BVP. However, unlike a typical NAE, the exact derivatives of the BVP are unavailable and must be approximated numerically. We choose to use Gauss-Newton method that requires only the 1st derivative, as opposed to Newton's method that requires both the 1st and 2nd derivatives. The following section discusses two Gauss-Newton based solvers to solve the BVP.

The Gauss-Newton method begins with a set of initial guesses \mathbf{x}_0 for the unknown initial values and parameters, and solves for \mathbf{x} iteratively. In any (say k^{th}) iteration, we approximate the constraint vector $\mathbf{g}(\boldsymbol{\mu}_u, \boldsymbol{\xi})$ at iteration in terms of the guesses \mathbf{x}_k by the 1st-order function:

$$\mathbf{g}(\mathbf{x}) \cong \mathbf{m}(\mathbf{x}) = \mathbf{g}(\mathbf{x}_k) + \mathbf{J}(\mathbf{x}_k)(\mathbf{x} - \mathbf{x}_k) \quad (2.3)$$

where $\mathbf{x} \in R^{r+m}$ is a vector of the guessed initial values and parameters,

namely $\mathbf{x} = [\boldsymbol{\mu}_u^T \quad \boldsymbol{\xi}^T]^T$;

$\mathbf{J}(\mathbf{x}_k)$ is the Jacobian matrix evaluated numerically (for example, finite-difference-method) at \mathbf{x}_k ; and

$\mathbf{g}(\mathbf{x}) \in R^{r+m}$ is the constraint vector given by Equations (2.2a) and (2.2b). The vector function $\mathbf{g}(\mathbf{x})$ should be zero if the problem is solved.

The remaining problem is then to find a vector \mathbf{x} that minimizes the approximation function:

$$\min \sum_{i=1}^{r+m} [m_i(\mathbf{x})]^2 \quad (2.4)$$

In the following two subsections, we consider two different cases; namely, with and without bounds on the unknowns. Case I (unbounded) is solved as a least square (L-S) problem. Case II is formulated as a quadratic programming (QP) problem, which allows the bounds to be imposed on the unknowns. Computational steps will be given for each case.

2.2.1 Unbounded Gauss-Newton method

No bound imposed on the unknowns –solved as an L-S problem.

Equation (2.4) is essentially a linear least-square (L-S) problem because the approximation functions can be expressed as

$$\sum_{i=1}^{r+m} [m_i(\mathbf{x})]^2 = \|\mathbf{J}_k \mathbf{x} - \mathbf{b}_k\|^2 \quad (2.5)$$

where $\mathbf{J}_k = \mathbf{J}(\mathbf{x}_k)$ and $\mathbf{g}_k = \mathbf{g}(\mathbf{x}_k)$ are defined to simplify the notation; and

$$\mathbf{b}_k = \mathbf{J}(\mathbf{x}_k) \mathbf{x}_k - \mathbf{g}(\mathbf{x}_k) = \mathbf{J}_k \mathbf{x}_k - \mathbf{g}_k \quad (2.6)$$

The L-S problem has a formal solution via matrix algebra

$$\mathbf{x} = \mathbf{x}_{k+1} = (\mathbf{J}_k^T \mathbf{J}_k)^{-1} \mathbf{J}_k^T \mathbf{b}_k \quad (2.7)$$

which replaces \mathbf{x}_k for the next iteration until

$$\|\mathbf{g}(\mathbf{x})\| \leq \textit{tolerance} .$$

Using Equation (2.6), Equation (2.7) can be written as

$$\mathbf{x}_{k+1} = (\mathbf{J}_k^T \mathbf{J}_k)^{-1} \mathbf{J}_k^T (\mathbf{J}_k \mathbf{x}_k - \mathbf{g}_k) = \mathbf{x}_k - (\mathbf{J}_k^T \mathbf{J}_k)^{-1} \mathbf{J}_k^T \mathbf{g}_k .$$

It is assumed here that $(\mathbf{J}_k^T \mathbf{J}_k)^{-1}$ exists. This is a line search procedure along the descent direction \mathbf{v} defined as

$$\mathbf{v} = -(\mathbf{J}_k^T \mathbf{J}_k)^{-1} \mathbf{J}_k^T \mathbf{g}_k \quad (2.8)$$

In order to know how far \mathbf{x}_k should go along the descent direction, a positive step-length factor β is introduced here

$$\mathbf{x}_{k+1} = \mathbf{x}_k + \beta \mathbf{v} \quad (2.9)$$

such that $\mathbf{g}(\mathbf{x}_k + \beta \mathbf{v})$ is minimum. In order to obtain the value of β , we choose three numbers $\beta_1 < \beta_2 < \beta_3$ that are close to β . We then construct a quadratic interpolation polynomial $p(z)$ from the three numbers. The minimum of $p(z)$ can be obtained at $\hat{\beta} \in [\beta_1, \beta_3]$, which approximates the minimum of $\mathbf{g}(\mathbf{x}_{k+1})$. The steps for the unbounded

Gauss-Newton method are outlined below:

Computational steps for Case I:

Given initial \mathbf{x}_0 , tolerance ε and $(\beta_1, \beta_2, \beta_3)$, repeat the following steps until ε is met:

Step 1: Evaluate $\mathbf{v} = -(\mathbf{J}_k^T \mathbf{J}_k)^{-1} \mathbf{J}_k^T \mathbf{g}_k$.

Step 2: Calculate the optimal $\hat{\beta}$ from $p(z)$.

Step 3: If $\|\mathbf{g}(\mathbf{x}_k + \hat{\beta} \mathbf{v})\| \leq \varepsilon$ return \mathbf{x}

else $\mathbf{x}_{k+1} = \mathbf{x}_k + \hat{\beta} \mathbf{v}$

End

2.2.2 Bounded Gauss-Newton method

Bounded unknowns– solved as a quadratic programming (QP) problem.

The drawback of SM for solving nonlinear BVP, however, is that initial guesses are needed to shoot for the specified terminal BV's on the other side of the domain. Bad initial guesses could lead to wrong solution or even divergence. Most practical physical problems, however, have bounded BV's and often these bounds are one-sided, positive or negative. For this reason, we offer an alternative formulation using knowledge of the problem to impose a bound on the unknowns in solving Equations (2.1), (2.2a) and (2.2b). Hence any initial guesses within the bound will lead to the true solution.

Expanding the approximation function in Equation (2.5),

$$\min \|\mathbf{J}_k \mathbf{x} - \mathbf{b}_k\|^2 = \min (\mathbf{x}^T \mathbf{J}_k^T \mathbf{J}_k \mathbf{x} - 2\mathbf{b}_k^T \mathbf{J}_k \mathbf{x} + \mathbf{b}_k^T \mathbf{b}_k) \quad (2.10)$$

Since $\mathbf{b}_k^T \mathbf{b}_k$ is a constant in every k^{th} step, it can be dropped from the minimization problem. The least square problem can be recast as a QP problem

$$\min (\mathbf{x}^T \mathbf{J}_k^T \mathbf{J}_k \mathbf{x} - 2\mathbf{b}_k^T \mathbf{J}_k \mathbf{x}), \quad \mathbf{x}_{lb} \leq \mathbf{x} \leq \mathbf{x}_{ub} \quad (2.11)$$

where \mathbf{x}_{lb} and \mathbf{x}_{ub} defines the lower and upper bounds of the initial guesses respectively.

Equation (2.11) is a standard QP problem that can be solved using various methods [Bazaraa *et al.*, 1993]. After solving the QP, the optimal solution will be the next step \mathbf{x}_{k+1} . The descent direction \mathbf{v} can be calculated as

$$\mathbf{v} = \mathbf{x}_{k+1} - \mathbf{x}_k \quad (2.12)$$

The procedure for finding β that minimize $\mathbf{g}(\mathbf{x}_{k+1})$ is the same as the previous section.

Computational steps for Case II:

Given initial \mathbf{x}_0 such that $\mathbf{x}_{lb} \leq \mathbf{x}_0 \leq \mathbf{x}_{ub}$, tolerance ε and $(\beta_1, \beta_2, \beta_3)$, repeat the following steps until ε is met:

Step 1: For every k^{th} step, solve the QP or Equation (2.11) for optimal \mathbf{x}_{k+1} .

Step 2: Evaluate $\mathbf{v} = \mathbf{x}_{k+1} - \mathbf{x}_k$.

Step 3: Calculate the optimal $\hat{\beta}$ from $p(z)$.

Step 4: If $\|\mathbf{g}(\mathbf{x}_k + \hat{\beta}\mathbf{v})\| \leq \varepsilon$ return \mathbf{x}

else $\mathbf{x}_{k+1} = \mathbf{x}_k + \hat{\beta}\mathbf{v}$

End

The formulation and solution method of bounded Gauss-Newton method offers two advantages:

- (1) The QP avoids inverting $\mathbf{J}_k^T \mathbf{J}_k$, which may be singular.
- (2) Some knowledge on the bounds of the unknown BV parameters ensures that the solution is always in the feasible region.

While developed for GSM, it is worth noting that bounded Gauss-Newton method can also be used to solve general nonlinear equations. As long as we know the upper bounds and lower bounds of the true roots, we can apply bounded Gauss-Newton method to avoid inverting $\mathbf{J}_k^T \mathbf{J}_k$.

2.3 Applications to Compliant Mechanisms

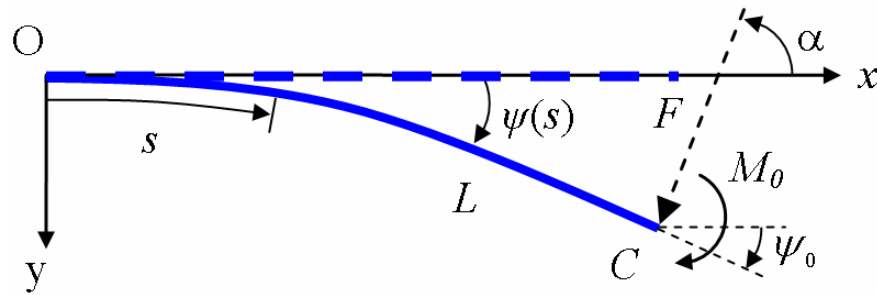
A general compliant mechanism includes multiple compliant links connected by pinned or clamped joints, the formulation of which is represented in the form suggested

by Equation (2.1). We offer here a systematic approach leading to a set of guidelines for formulating a compliant mechanism. The approach begins with the governing equations for a flexible beam capable of large deflection; for clarity, we divide beams into two categories; namely, beams that are initially straight and curved. This is followed by formulating the flexible beam as a member of a compliant mechanism, along with the method for identifying the unknowns and the complete set of constraint equations.

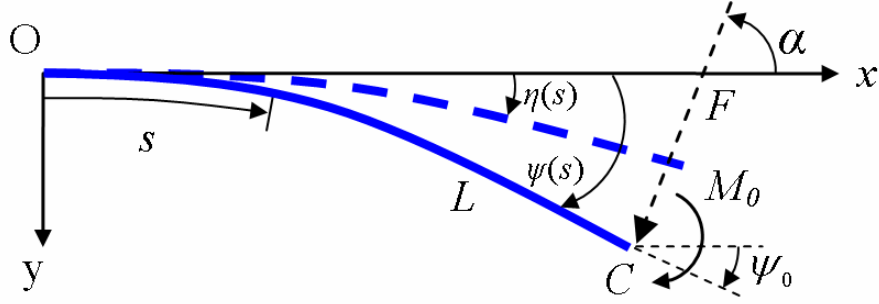
In the following discussion, we introduce in Subsections 2.3.1 and 2.3.2 a flexible beam model based on [Frisch-Fay, 1962] for characterizing large deflection of straight and curved compliant members respectively. These governing equations, which offer a means to analyze compliant mechanisms where the effect of axial deformation is negligible, will be recast as 1st order ODE's with $n=2$ in Subsection 2.3.3 and used for all examples in this chapter (except in Subsection 2.5.1 where the effect of axial deformation is examined). We also provide two alternative models (with $n=4$ and $n=6$) in Appendix A that can predict axial deformation of compliant members with large deflection.

2.3.1 Governing equation of a flexible beam: *Initially straight*

Figure 2.2(a) shows an initially straight beam of length L deflected under a point force F along the direction α and an external bending moment M_0 at location C .



(a) Initially straight beam



(b) Initially curved beam

Figure 2.2 Schematics and coordinate systems of a flexible beam

In Figure 2.2(a), the coordinate frame O is attached at one end of the beam, where the x axis lies on the un-deflected beam that deflects in the y direction. The location of C is denoted as $\mathbf{P}_C = [x_C \ y_C]^T$.

The bending moment M at a point (x, y) on the beam is given by

$$EI(s) \frac{d\psi}{ds} = M = F \sin \alpha (x_C - x) + F \cos \alpha (y_C - y) + M_0 \quad (2.13)$$

where s is the arc length of the beam as shown in Figure 2.2(a);

E is Young's modulus of the beam material;

$I(s)$ is the moment of area of the beam;

ψ is the angle of rotation;

M is the bending moment (positive when it produces compression in the lower part of the beam);

F is the applied force (positive when pointing towards the positive y -direction.); and

M_0 is the applied moment at the end of the beam.

In order to express Equation (2.13) explicitly in terms of s , we differentiate it with respect to s leading to the following 2nd order differential equation:

$$EI(s)\frac{d^2\psi}{ds^2} + E\frac{dI(s)}{ds}\frac{d\psi}{ds} = -F\sin\alpha\cos\psi - F\cos\alpha\sin\psi \quad (2.14)$$

where $\cos\psi = dx/ds$ and $\sin\psi = dy/ds$. Note that the constant M_0 vanishes after differentiation. We then normalize Equation (2.14) leading to a dimensionless nonlinear differential equation of θ with respect to u ,

$$\frac{1}{L^2}\frac{d}{du}\left[I(u)\frac{d\theta}{du}\right] + \frac{F}{E}\sin\theta = 0 \quad (2.15)$$

$$\text{where} \quad u = s/L \in [0,1] \quad (2.15a)$$

$$\text{and} \quad \theta = \psi + \alpha \in [\alpha, \alpha + \psi_0] \quad (2.15b)$$

2.3.2 Governing equation of a flexible beam: *Initially curved*

If the un-deformed beam is initially curved (neither straight nor parallel to x axis) as shown in Figure 2.2(b). Then, the intrinsic curve function $\eta(s)$ must be included. The dashed line represents the free shape of the beam described by $\eta(s)$ while the solid line represents the deformed shape of the beam described by $\psi(s)$.

The initial curvature has no effect on bending moment and is subtracted from Equation (2.13) to obtain Equation (2.16):

$$M = EI(s)\left[\frac{d\psi}{ds} - \frac{d\eta}{ds}\right] \quad (2.16)$$

Following the same procedure as described in Subsection 2.3.1, the governing equation of an initially curved beam can be described as follows after normalization.

$$\frac{1}{L^2}\frac{d}{du}\left[I(u)\left(\frac{d\theta}{du} - \frac{d\eta}{du}\right)\right] + \frac{F}{E}\sin\theta = 0 \quad (2.17)$$

Clearly, Equation (2.15) is a special case of Equation (2.17) with $\eta(s)=0$. Hence, we will refer to Equation (2.17) and Figure 2.2(b) as the general governing equation for the

flexible beam hereafter. Once Equation (2.17) is solved, the position C can be obtained from Equation (2.18):

$$\begin{bmatrix} x_C \\ y_C \end{bmatrix} = L \int_0^1 \begin{bmatrix} \cos \psi \\ \sin \psi \end{bmatrix} du = L \int_0^1 \begin{bmatrix} \cos(\theta - \alpha) \\ \sin(\theta - \alpha) \end{bmatrix} du \quad (2.18)$$

It is worth noting that the beam formulation derived here allows for non-uniform cross-section, which can be incorporated through the moment of inertia $I(u)$ as shown in Equation (2.17). This ability to model beams with non-uniform cross-section would serve as an essential basis for dealing mechanisms with links of arbitrary geometry.

2.3.3 Beam as a member in a compliant mechanism

Consider the flexible beam in Figure 2.2(b) as the i^{th} link of a compliant mechanism. Equation (2.17) that governs the large deflection of the link can be written in the form as Equation (2.1) by defining $\theta_{i1} = \theta$ and $\theta_{i2} = d\theta / du = \theta'_{i1}$:

$$\boldsymbol{\theta}'_i = \mathbf{f}_i(u_i, \boldsymbol{\theta}_i, \boldsymbol{\xi}_i) \quad (2.19)$$

where $\mathbf{f}_i = [f_{i1} \quad f_{i2}]^T$,

$$f_{i1} = \theta_{i2} \quad (2.19a)$$

$$f_{i2} = -\frac{I'_i(u_i)}{I_i(u_i)} \theta_{i2} + \frac{I'_i(u_i) \eta'_i(u_i)}{I_i(u_i)} + \eta''_i(u_i) - \frac{F_i L_i^2}{E_i I_i(u_i)} \sin \theta_{i1} \quad (2.19b)$$

The initial values needed to solve Equation (2.19) are $\theta_{i1}(0)$ and $\theta_{i2}(0)$. For a general compliant link as shown in Figure 2.2(b), the known and unknown initial values (presented in Table 2.1) depend on the type of joints at O. As shown in Table 2.1, the i^{th} compliant link has one unknown initial value for either clamped or pinned end. Similarly, a compliant mechanism composed of k compliant links has $m=k$ unknown initial values.

Table 2.1 Clamped and pinned initial conditions

Conditions at O	Initial Values	
	Known	Unknown
Clamped	$\theta_{i1}(0) = \alpha_i + \eta_i(0)$	$\theta_{i2}(0)$
Pinned	$\theta_{i2}(0) = \eta'_i(0)$	$\theta_{i1}(0)$

The unknown parameters are consequences of connecting compliant links together. For example, the applied forces F_i and F_{i+1} to the i^{th} and $(i+1)^{th}$ link are essentially the reaction forces when the two links are connected at the joint. Hence, these “hidden” variables must be treated as unknowns. In general, the unknown parameter vector ξ_i for the i^{th} link includes the force F_i and its direction α_i . Initial guesses have to be made about these unknown parameters in order to integrate Equation (2.1). The number of unknowns (initial values and parameters) then has to match the number of constraint equations in the following subsection so they can be solved using Gauss-Newton method.

2.3.4 Formulation of constraint equations

As shown in Figure 2.3(a), the constraint sets Equations (2.2a) and (2.2b) for a compliant mechanism can be obtained by applying Newton’s 3rd law and geometrical constraints at joint C , which connects one link to another by a pinned or clamped condition.

Constraint Set I: For a pinned joint connection at C , there is no moment. Hence,

Equation (2.2a) becomes

$$\theta_{i2}(1) = \eta'_i(1) \quad i = 1, 2 \quad (2.20)$$

For a clamped joint at C , the constraints have the following form:

$$c_{11}\theta_{11}(1) + c_{13}\theta_{21}(1) + d_1 = 0 \quad (2.21a)$$

$$c_{22}\theta_{12}(1) + c_{24}\theta_{22}(1) + d_2 = 0 \quad (2.21b)$$

Equation (2.21a) states that link 1 and 2 form a constant clamped angle at C while Equation (2.21b) is a moment balance equation at C. Coefficients c and d are determined by the above angle/moment equations.

Constraint Set II: The physical constraints are derived from the free body diagram as shown in Figure 2.3(b) with Newton's 3rd law:

$$F_1 - F_2 = 0 \quad (2.22a)$$

$$\alpha_1 - \alpha_2 - \phi = 0 \quad (2.22b)$$

where ϕ is the relative orientation between frame 1 and frame 2. Since C is a common point for both links, its location in both links is the same after transformation

$$\mathbf{R}_2 \mathbf{P}_C + {}_2\mathbf{P}_1 = \mathbf{P}_C \quad (2.22c)$$

where \mathbf{R} is the transformation matrix from frame 2 to frame 1; \mathbf{P}_C is the position vector of C in frame i , $i=1,2$; and ${}_2\mathbf{P}_1$ is the position vector of O_2 expressed in frame 1.

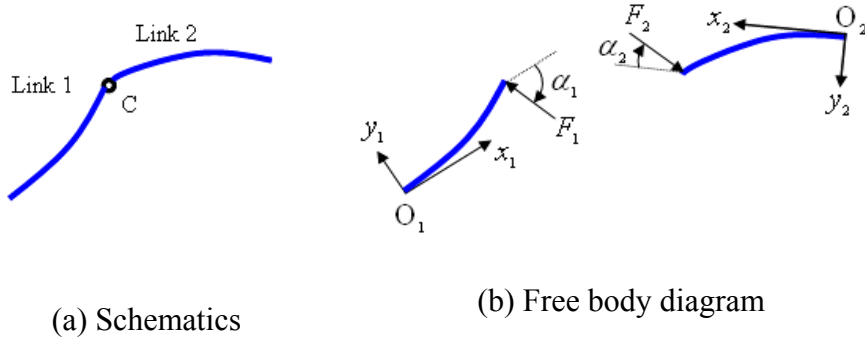


Figure 2.3 A pair of connecting links

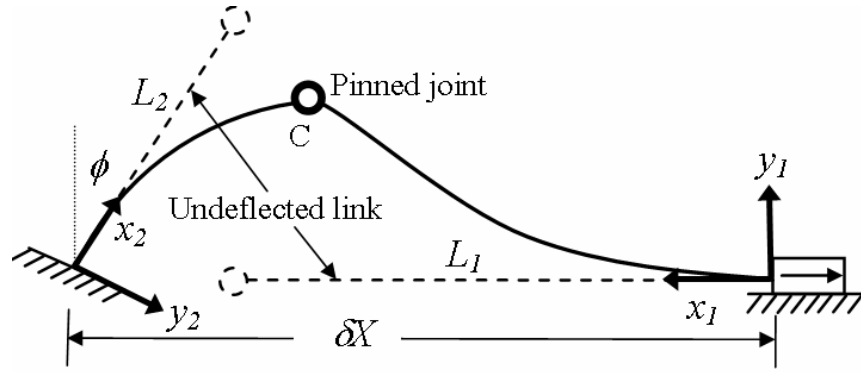
The above formulation shows that the basic procedures for solving compliant-mechanism problems are (1) identifying unknown initial values and parameters needed for solving the ODE of the compliant links, (2) next, identifying constraint equations

from joints and rigid links, (3) then matching the number of unknowns to the number constraint equations, and (4) finally solving using Gauss-Newton method.

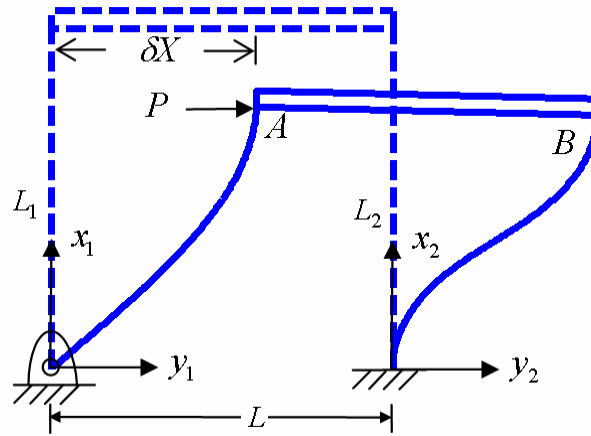
2.4 Numerical Examples

Five examples (shown in Figures 2.4 2.9 and 2.11) are considered here to illustrate the formulation in Section 2.3 for a broad spectrum of applications. The examples are divided into two classes based on their initial shapes; namely, initially straight and initially curved links.

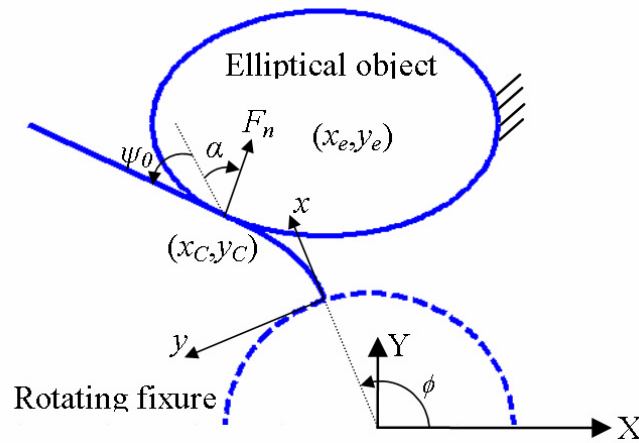
- *Compliant mechanisms with initially straight links.* Example 1 shows a pair of compliant links directly connected by a pinned joint as shown in Figure 2.4(a), where the linear motion δX is controlled by the link deflection. Unlike Example 1, the two flexible links in Example 2 are clamped to a rigid member and the input displacement is applied at the joint as shown in Figure 2.4(b), where the constraint equations come from the rigid link. A special case of Example 2, where both links are clamped to a fixed frame is commonly used for precision manipulation of camera lens. Example 3 is a special class of compliant mechanisms where the link is in contact with a smooth object as shown in Figure 2.4(c). Unlike Examples 1 and 2, the contact problem in Example 3 involves no joints. In addition, the point where the force applies is not known in advance and hence, the length L from origin to contact point must be treated as an unknown.
- *Compliant mechanisms with initially curved links.* Examples 4 and 5 show that the formulation can be extended to compliant mechanisms involving initially curved beams. The schematics of these examples (with non-constant and constant radius of curvature) are shown in Figures 2.9 and 2.11 respectively.



(a) Example 1: Compliant slider mechanism



(b) Example 2: Compliant parallel mechanism



(c) Example 3: Compliant contact mechanism

Figure 2.4 Illustrative examples

Table 2.2 summarizes the unknown parameters/initial values for the five examples.

Table 2.2 Summary of unknown parameters in Examples 1 - 5

Ex.	ℓ	r	ξ	m	μ_u	p
1	2	4	$F_1, \alpha_1, F_2, \alpha_2$	2	$\theta_{12}(0), \theta_{22}(0)$	2
2	2	5	$F_1, \alpha_1, F_2, \alpha_2, P$	2	$\theta_{12}(0), \theta_{22}(0)$	2
3	1	3	F, α, L	1	$\theta_2(0)$	1
4	1	1	α	1	$\theta_{12}(0)$	1
5	2	4	$F_1, \alpha_1, F_2, \alpha_2$	2	$\theta_{12}(0), \theta_{22}(0)$	2

These unknowns are formatted with notations in Subsections 2.3.3 and 2.3.4. The constraints I and II that correspond to terminal and physical constraints respectively, and selected numerical results are given for each example.

2.4.1 Compliant mechanisms with only initially straight links

Example 1: Compliant Slider Mechanism (CSM)

We expect $r+m=6$ constraint equations; namely, $p=2$ terminal and $r+m-p=4$ physical constraint equations:

Constraint Set I: The two equations are given by Equation (2.20) for a pinned joint.

Constraint Set II: They are written in similar forms as Equation (2.22),

$$F_1 - F_2 = 0 \quad (2.23a)$$

$$\alpha_1 - \alpha_2 - \pi/2 + \varphi = 0 \quad (2.23b)$$

$$\begin{bmatrix} \cos(\pi - \phi) & -\sin(\pi - \phi) \\ \sin(\pi - \phi) & \cos(\pi - \phi) \end{bmatrix} \begin{bmatrix} x_{2C} \\ y_{2C} \end{bmatrix} + \begin{bmatrix} \delta X \\ 0 \end{bmatrix} = \begin{bmatrix} x_{1C} \\ y_{1C} \end{bmatrix} \quad (2.23c)$$

where $[x_{1C} \ y_{1C}]$ and $[x_{2C} \ y_{2C}]$ are locations of C expressed in frame 1 and 2 respectively;

ϕ is the angle between x_2 and y_1 axes; and

δX is the distance between the origins of frame 1 and 2.

Hence, the numerical solver in Section 2.2 can be used to solve for the six $(r+m)$ unknowns and the deflected shape of the links from the two ODE's in Equation (2.1) and the six constraint equations given by the constraint sets. Figure 2.5 shows the results of varying δX , where the displacement of the slider along the x_1 direction is chosen as input.

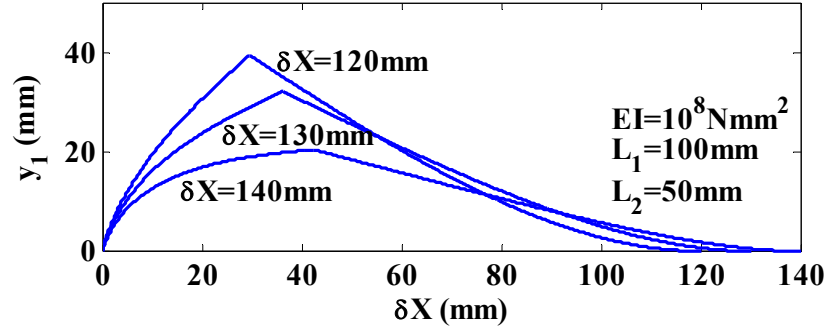


Figure 2.5 Numerical results for Example 1

Example 2: Compliant Parallel Mechanism (CPM)

We expect to have $r+m=7$ constraint equations from the rigid member connecting the two flexible links. The constraint equations, which are similar to Equations (2.20)~(2.22), are obtained as follows:

Constraint Set I ($p=2$): Two terminal constraints must be satisfied after integrating Equation (2.1):

$$g_i = [\theta_{i1}(1) - \alpha_i] - \phi = 0 \quad i = 1, 2 \quad (2.24)$$

where $\phi = \tan^{-1} \frac{x_A - x_B}{y_B + L - y_A}$; L is the length of rigid link AB whose end positions $[x_A$

$y_A]$ and $[x_B \ y_B]$ are expressed in frame 1 and 2 respectively.

Constraint Set II ($r+m-p=5$): The equations are as follows. The deflected position of point A on link 1 is the same as the displacement input δX .

$$g_3 = y_A - \delta X = 0 \quad (2.25a)$$

Since the member AB is rigid, we have

$$g_4 = (x_A - x_B)^2 + (y_B + L - y_A)^2 - L^2 = 0 \quad (2.25b)$$

Summing the forces applied to link 1 at point A leads to g_5 and g_6 ,

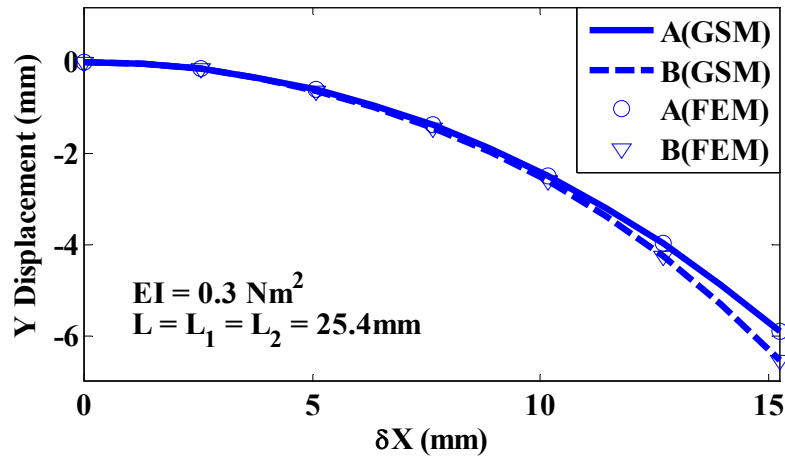
$$F_1 = [(P - F_2 \sin \alpha_2)^2 + (F_2 \cos \alpha_2)^2]^{1/2} \quad (2.25c)$$

$$\alpha_1 = \pi/2 - \tan^{-1} \left(\frac{P - F_2 \sin \alpha_2}{F_2 \cos \alpha_2} \right) \quad (2.25d)$$

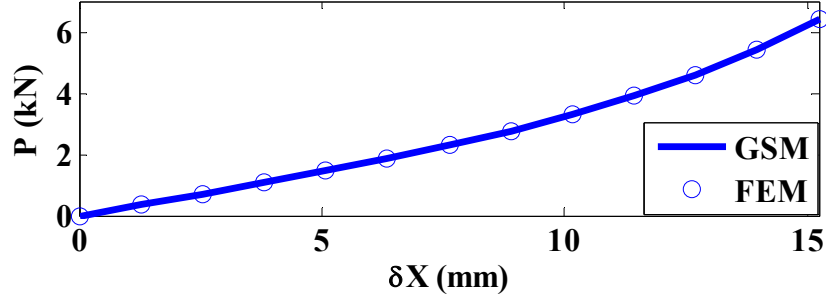
In addition, balancing the moment on the rigid link AB , we have g_7 as

$$\frac{EI}{L_1} \theta_{12}(1) + \frac{EI}{L_2} \theta_{22}(1) + F_2 L \cos(\alpha_2 + \phi) = 0 \quad (2.25e)$$

Figure 2.6(a) shows the displacement of A and B in x_1 and x_2 direction while Figure 2.6(b) shows P - δX curve. Both results are compared with those computed using FEM (BEAM3 in ANSYS is used to model the compliant link). As δX increases, the rigid link would tilt (A is higher than B) from horizontal. It is worth noting that the pseudo-rigid-body model [Howell *et al.*, 1996] is unable to predict such a rotation.



(a) Vertical displacement of points A and B



(b) Force required at point A

Figure 2.6 Numerical results for Example 2

Example 3: Compliant Contact Mechanism

We consider here a rotating link in contact with a moving, frictionless elliptical object. The $r+m=4$ constraint equations at the contact point C are obtained as follows:

Constraint Set I ($p=1$): The terminal constraint equation is

$$g_1 = \theta_2(1) = 0 \quad (2.26)$$

Constraint Set II ($r+m-p=3$): Three physical constraints imposed at C which lies on the object peripheral. First, its location (x_C, y_C) must satisfy the ellipse equation f_e described in the link frame:

$$g_2 = f_e(x_C, y_C) = 0 \quad (2.27a)$$

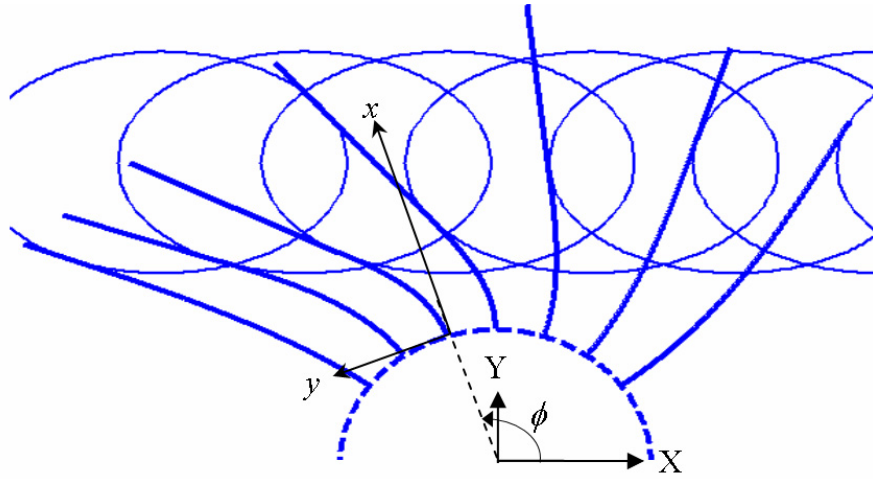
Next, the link and the object share the same slope at the contact point, and since $\psi_0 = \theta_1(1) - \alpha$. We have

$$g_3 = \left. \frac{\partial f_e / \partial x}{\partial f_e / \partial y} \right|_{(x=x_C, y=y_C)} + \tan \psi_0 = 0 \quad (2.27b)$$

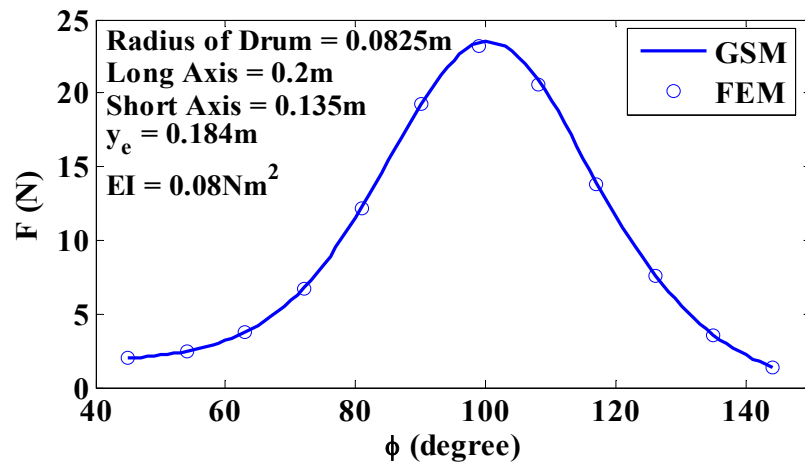
Finally, for frictionless contact, the contact force F_n will be normal to the link at C.

$$g_4 = \theta(1) - \pi/2 = \alpha + \psi_0 - \pi/2 = 0 \quad (2.27c)$$

The shapes and contact forces of the deflected link at various contact states are shown in Figure 2.7. In Figure 2.7(a), $\phi = -236.22x_e + 102^\circ$ where x_e (in m) is the center of the ellipse. Figure 2.7(b) compares the predicted forces against those computed using FEM with ANSYS. These FEM results were obtained by using TARGET169 and CONTACT172 contact pair for the ellipse and link respectively. Figure 2.8 also shows one particular convergence result of GSM with $[\phi \ x_e] = [\pi/2 \ 0.0508]$. The norm of constraints equations $\|g\|$ is less than 10^{-12} after 8 iterations.



(a) Deflection of compliant links at contact



(b) Contact forces and comparison against FEM

Figure 2.7 Deflection and contact forces for Example 3

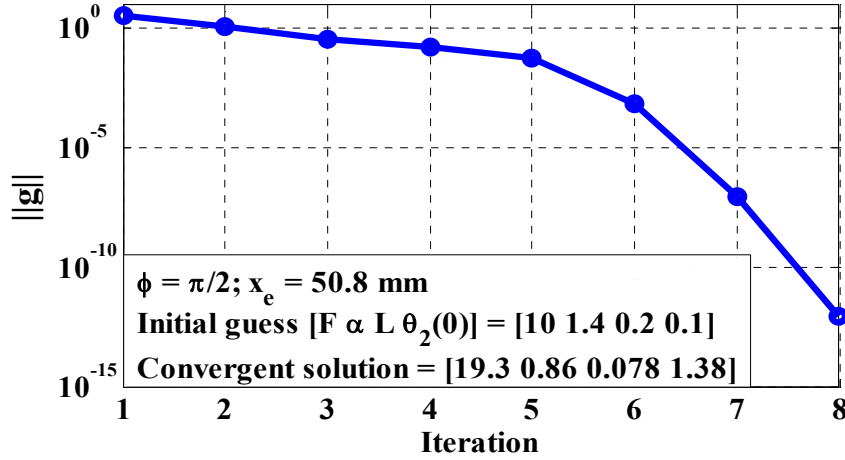


Figure 2.8 Convergence result for Example 3

2.4.2 Initially curved links

Example 4: Planar spring - non-constant radius of curvature

For initially curved beams that do not have a constant radius of curvature, the intrinsic curve function can be obtained by approximation functions. An example is given in Figure 2.9; a linear force-displacement mechanism consists of a pair of planar springs that can be characterized by the intrinsic curve function:

$$\eta = 1.6 \cos 5\pi u \quad (2.28)$$

Planar springs can be used where large linear strokes are needed, and in situation such as in MEMS where 3-D spiral springs are difficult to fabricate. Quevy *et. al* [2002] has implemented the planar spring mechanism for scratch drive actuator. As shown in Figure 2.9, the two springs are mirror images of each other and thus only one of them needs to be considered. The vertical input force F on the rigid link AB causes a δX displacement.

Following the same procedure as before, we have the unknowns of this problem

$$\xi = \alpha \text{ and } \mu_u = \theta_{12}(0)$$

Constraint Set I ($p = 1$): For a constant clamped angle,

$$[\theta_{11}(1) - \alpha_1] + 1.6 = 0$$

Constraint Set II ($r+m-p=1$): Due to the vertical force F and rigid link AB , point A will have no displacement in the y_1 direction and hence

$$y_A = 0.$$

Figure 2.10 shows the force-displacement curve of the planar spring mechanism. Since the relationship is linear, we can approximate the spring constant to be 3.2667×10^4 N/m.

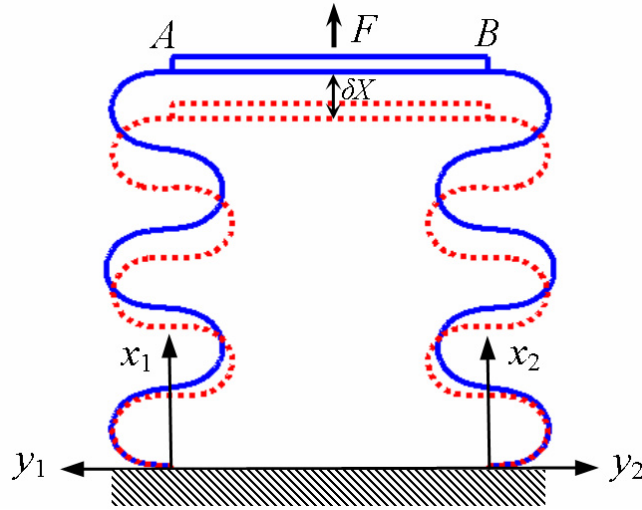


Figure 2.9 Planar spring mechanism

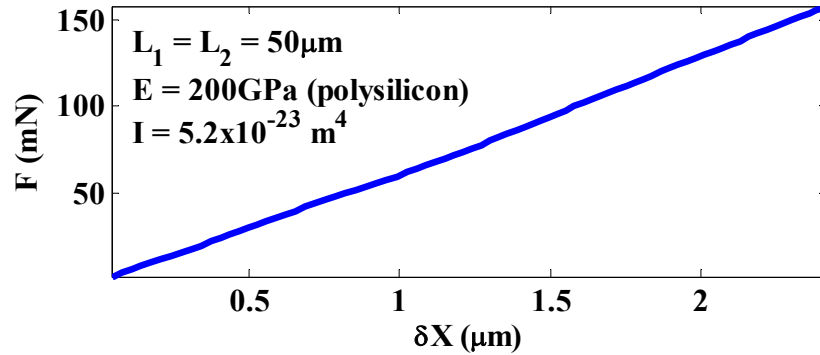


Figure 2.10 Force-displacement relationships

Example 5: Compliant mechanism with constant radius of curvature

When an initially curved link of length L forms the arc of a circle of radius R , the intrinsic curve function has the following properties:

$$\eta'(u) = L/R \text{ and } \eta''(u) = 0 \quad (2.29)$$

We consider a compliant mechanism with arcs as shown in Figure 2.11(b), an application of which is given in Subsection 2.5.2. Due to the symmetry of the mechanism, we only need to consider a quarter segment as shown in Figure 2.11(a). Link 1 is initially curved (with $\eta'_1 = L_1 / R_1$) and has length L_1 . Link 2 is initially straight and has length L_2 . Frame 1 and 2 are both attached to the clamped ends of the two links. The other ends of the links are also clamped together at C . The origin of frame 1 is under a vertical displacement load δY . In order to investigate the force-displacement relationship, we have to know the action and reaction forces at C along with initial slope at the deformed state. Specifically, the unknowns of this problem are $\xi = [F_1 \quad \alpha_1 \quad F_2 \quad \alpha_2]^T$ and $\mu_u = [\theta_{12}(0) \quad \theta_{22}(0)]^T$.

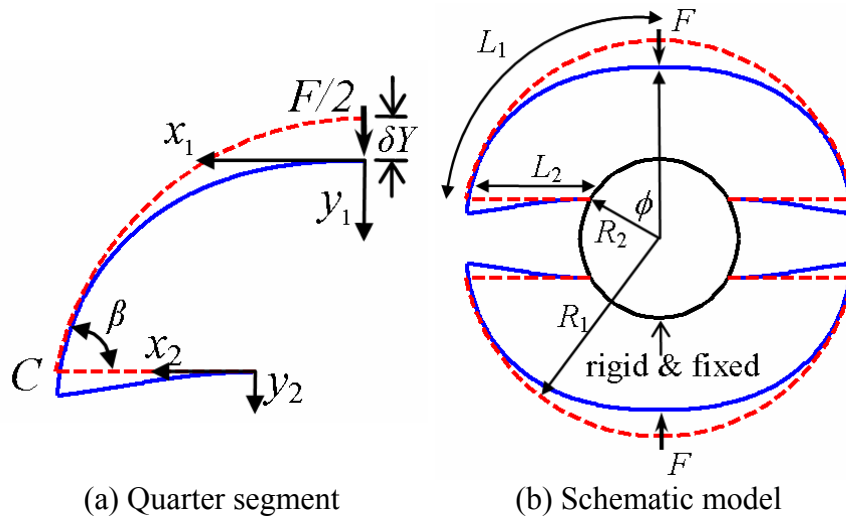


Figure 2.11 A compliant mechanism with initially curved links

The $r+m=6$ constraint equations are given as follows:

Constraint Set I ($p = 2$): The clamped angle β can be obtained by the relationship $\beta = L_1 / R_1 - \phi$ geometrically.

$$(\theta_{11}(1) - \alpha_1) - (\theta_{21}(1) - \alpha_2) - \beta = 0 \text{ (constant clamped angle)}$$

$$\theta_{12}(1) - \frac{L_1}{R_1} + \theta_{22}(1) = 0 \text{ (Newton's 3rd law)}$$

Constraint Set II: ($r+m-p=4$)

(1) From Newton's 3rd law, $F_1 = -F_2$; and $\alpha_1 = \alpha_2$.

(2) The location of joint C in both links is the same after transformation.

$$\begin{bmatrix} x_{2C} \\ y_{2C} \end{bmatrix} + \begin{bmatrix} R_2 \sin \phi \\ R_1 - R_2 \cos \phi - \delta Y \end{bmatrix} = \begin{bmatrix} x_{1C} \\ y_{1C} \end{bmatrix}$$

After solving the unknowns by GSM, the normal force F can be obtained from the equation $F = 2F_1 \sin \alpha_1$. The simulation and experiment results are compared in Section 2.5.

2.5 Verification of Generalized SM

By investigating the deflection shape of a uniform cantilever beam under a point force at the end as shown in Figure 2.1, the objectives of this section are (1) to verify GSM by comparing the result with close-form solution (2) to compare GSM with FDM and FEM and (3) to validate GSM by comparing with experiment results.

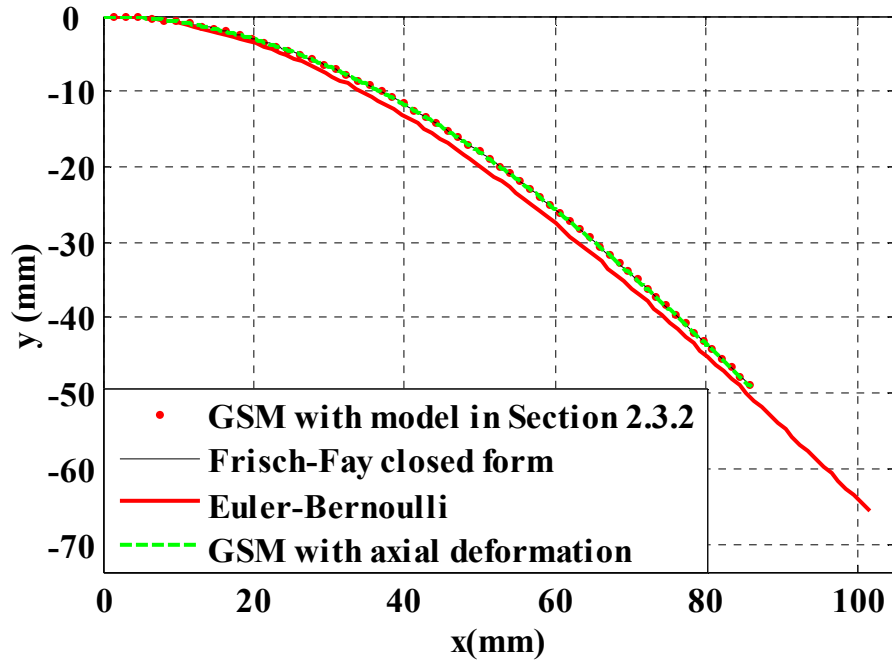
2.5.1 Numerical verification

Since exact solutions are only available for a uniform beam, we verify the numerical model by comparing the deflected shape of a uniform beam against published solutions. Table 2.3 lists the simulation parameters.

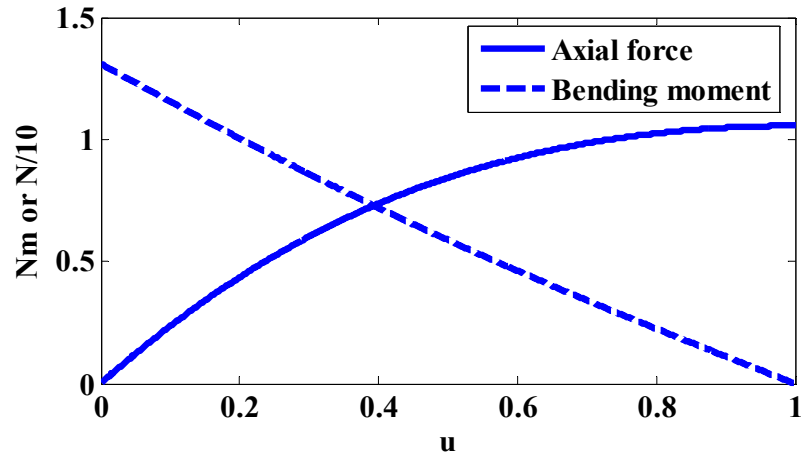
Table 2.3 Simulation parameters (uniform beam)

$EI = 0.08 \text{ Nm}^2$	$EA = 2146 \text{ N}$	$F = 15 \text{ N}$	$N = 20$	$L = 101.6 \text{ mm (4 inches)}$	$\alpha = 90^\circ$
--------------------------	-----------------------	--------------------	----------	-----------------------------------	---------------------

Since the force F and its direction α are given, the formulation of GSM consists of only one unknown initial value $\mu_u = \theta_2(0)$ and one constraint equation $\theta_1(1) = 0$. After several iterations of Gauss-Newton method, the predicted shape of the beam can be computed by using Equation (2.18). The results are compared in Figure 2.12(a) against the exact solution given by Frisch-Fay [1962], Euler-Bernoulli beam model (a special case of Appendix A.2), and the model that accounts for the axial deformations in Appendix A.1. The corresponding axial forces and bending moments calculated using Appendix A.1 are shown in Figure 2.12(b). In order to characterize the error of GSM, we also solve Equation (2.17) using FDM and FEM [Yin *et al.*, 2004]. The percentage errors, which are defined as $\% \text{ error} = 100[\theta - \theta(\text{exact})]/\theta(\text{exact})$, are compared in Figure 2.13.



(a) Deflected shape of a uniform beam



(b) Axial force and bending moment (uniform beam)

Figure 2.12 Verification of GSM

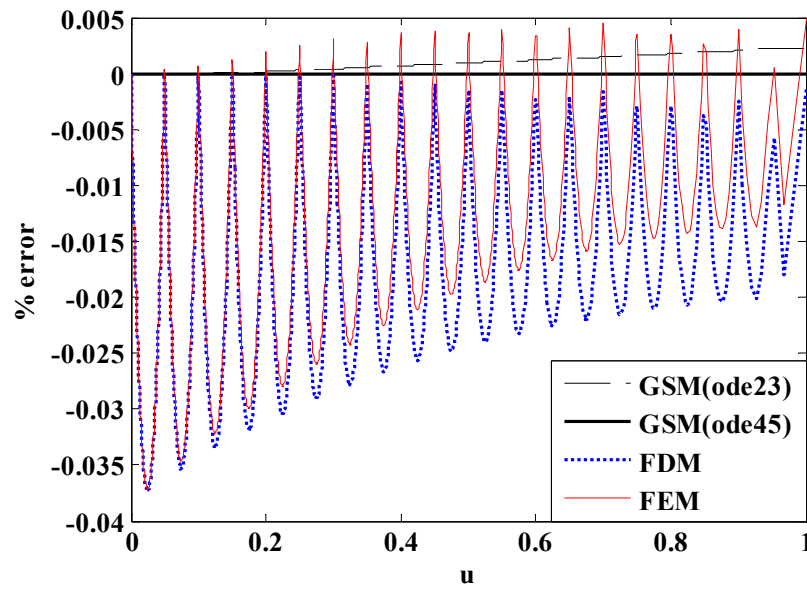


Figure 2.13 %Error ($N=20$ for both FDM and FEM)

The following observations can be made from the comparison between GSM and other existing methods.

1. As compared in Figure 2.12(a), both models of GSM (with and without accounting for the effect of axial deformation) yield the same deflected shape and fully agree with Frisch-Fay's closed-form solution; the effect of axial forces on the deflected

shape is small. The Euler-Bernoulli beam theory (modeled on the assumption of small deflection) fails to predict the deflected shape especially at the free end as expected.

2. Figure 2.13 illustrates the accuracy of GSM (that converges after 5 iterations) depends on the scheme integrating the ODE; it is relatively easy to achieve higher-order accuracy. The calculated shapes using GSM (with “ode45” in MATLAB) perfectly match those calculated using the Frisch-Fay solution.
3. The non-uniform link as defined by $I_i(u_i)$ in Equation (2.19b) and the derivative BC's $[\theta_2(0) \theta_2(1)]$ in Table 2.1 need not be discretized as required by FDM. Hence the solutions can be more accurate.
4. The FDM and FEM satisfy the boundary condition (BC) automatically and thus, do not need a recursive algorithm to estimate for the BC, which is the basis of GSM. However, these methods (FDM and FEM), which are often referred to as a global method, interpolate between nodes. Their accuracy depends on the mesh number N , and thus need more computation time in order to improve accuracy. The errors for both the FDM and FEM are less than 0.05% when $N=20$ as shown in Figure 2.13. Due to the singularities in the FEM formulation [Yin *et al.*, 2004], the number of divisions N of FEM can hardly go beyond 20. The times required for GSM and FDM computation using MATLAB on a Pentium 4 PC (1.5 GHz with 512 MB memory) are compared in Table 2.4. GSM is computationally more efficient as it relies on the order of the numerical integration scheme rather than N to improve its accuracy.

Table 2.4 Comparisons of computation time

Method	Time(s)	Iteration	Method	Time(s)	Iteration
GSM(ode23)	0.938	5	FDM($N=100$)	1.187	7
GSM(ode45)	1.031	5	FDM($N=500$)	12.281	7

In general, the computation time depends on ℓ , ξ , and μ_u . For $\|g\| = 10^{-8}$ as the convergence criteria, the computation time of Examples 1 to 5 are 3.37, 3.43, 3.76, 4.06, 3.45 seconds respectively.

2.5.2 Experiment validation

In this section, GSM will be validated by comparing computed results against those obtained experimentally. Two experiments are considered; namely, a flexible beam and a compliant mechanism with curved members.

Experiment 1: Uniform beam under a point load at the end

The schematic of this experiment is shown in Figure 2.1, where the parameters of the beam are given in Table 2.5. Specifically, the aluminum beam was clamped at one end and a vertical load was applied at the other end using a static weight. The deflection was then determined from images taken using digital camera (OLYMPUS C-700uz, 1600x1200 pixels resolution) along with an edge detection algorithm. The field-of-view was made such that the image provides a resolution in the order of 0.1mm for a tip deflection of 50mm. The deflected shapes for two different lengths are plotted in Figure 2.14; the computed results are within 5% of those measured experimentally.

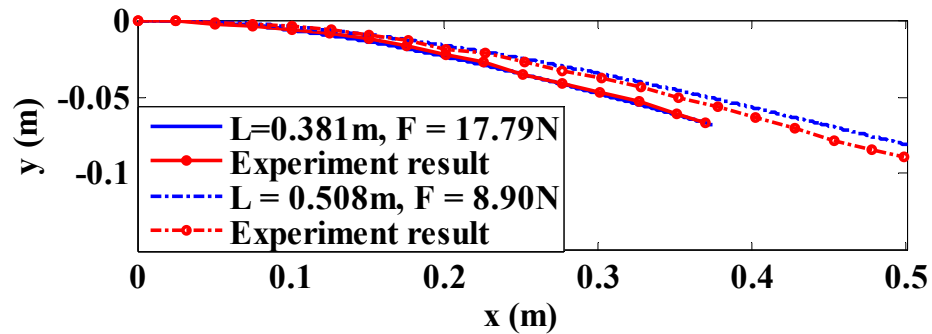


Figure 2.14 Experiment results

Table 2.5 Experiment parameters (Aluminum beam, 6602-T6511)

$E=68.9\text{GPa}$
Thickness=3.175 mm (1/8 inch)
$\alpha=90^\circ$
Width=25.4mm (1 inch)

Experiment 2: Rotating indexer

Figure 2.15 shows a practical application of Example 5, which has been used as an indexer to position a rotating shaft at pre-determined locations. As the shaft rotates, the curved compliant mechanism deforms inside the housing. The two convexes and four concaves are designed to snap-fix the shaft position every 90° . Effective design of such an indexer relies on the ability to predict normal forces between the convexes and the housing.

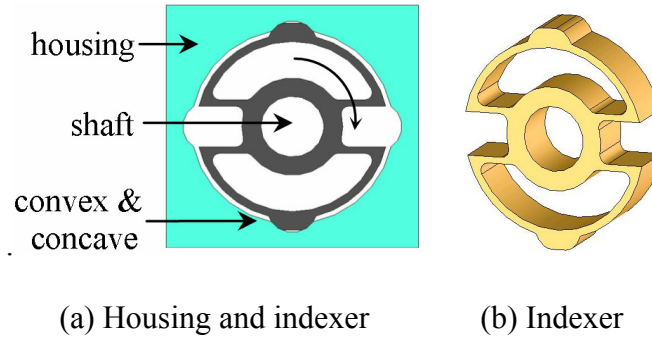


Figure 2.15 CAD model of the rotating indexer

The F - δY relationship of the indexer was measured using the force tester from TESTRESOURCES (Model 650M). As shown in Figure 2.16, the indexer was clamped between the two slightly flattened convexes as shown in Figure 2.16. Reaction forces were taken as displacement loads were applied along the convexes. The experimentally measured F - δY relationship and the analysis of Example 5 are compared in Figure 2.17; the excellent agreement shows that Generalized SM can facilitate the design of the rotating indexer.

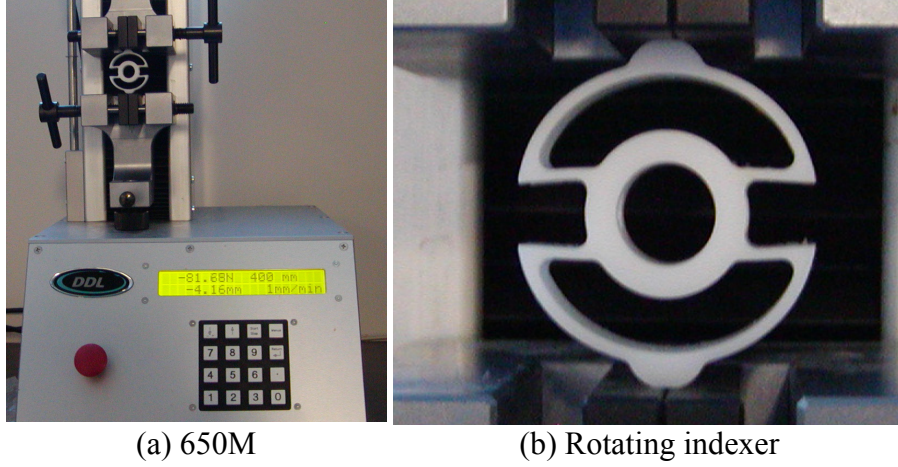


Figure 2.16 Experiment setup

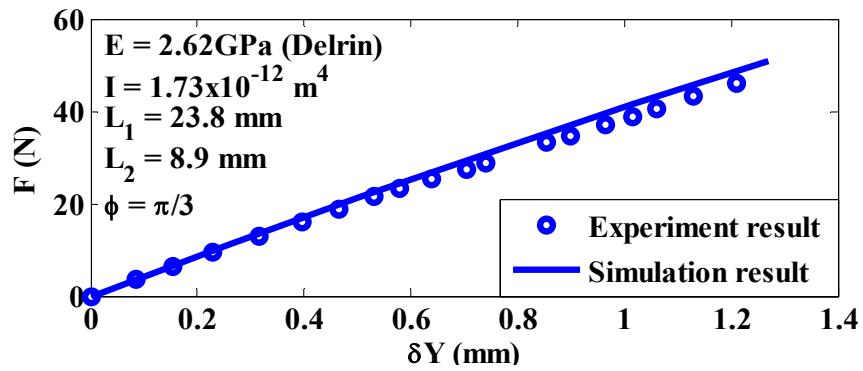


Figure 2.17 F - δY curve

2.6 Conclusions

A general formulation based on Shooting Method has been presented for analyzing compliant mechanisms consisting of initially straight or curved flexible beam members capable of large deflection. As the terminal and physical constraint equations are essential to complete formulation of the problem, a systematic procedure for deriving these equations at the (pinned or clamped) joint connections is given along with two numerical solvers (Gauss-Newton and bounded Gauss-Newton methods) that solve for the deflected shape of the flexible members. Five numerical examples were given to

illustrate the formulation of Generalized Shooting Method and its applications to analyze general planar compliant mechanisms.

This chapter numerically compared the analysis of a flexible beam against predictions with four other methods; exact solution [Frisch-Fay, 1962], linear small-deflection theory, FD and FE methods. Except the linear small-deflection theory that fails at large deflection applications, the numerical solutions closely agree with each other. The advantages of GSM (which treats the BVP as an IVP) over the FD and FE methods include the following: (1) both initially straight and initially curve links share the same simple formulation. (2) It is relatively easy to achieve higher-order accuracy. (3) It can deal with unusual boundary conditions and nonlinear material properties without approximation. This simplicity in formulating GSM, which bases on distributed-parameter with variational principles, makes GSM an ideal candidate for topology synthesis of compliant mechanisms for two reasons: (1) The geometry of a compliant link can be easily varied by changing η and L . (2) The links can be deleted from or added to a compliant mechanism by merely reformulating unknown initial values/parameters and constraint sets.

Finally, we validated experimentally the analysis of a flexible beam and a practical rotational indexer made up of curved members. The excellent agreement shows that the formulation and analysis offered by Generalized SM can effectively facilitate the process of design and optimization of compliant mechanisms that have a broad spectrum of applications ranging from MEMS device fabrication [Quevy et al., 2002] to automated handling of live objects in food processing industry [Lee, 2001].

CHAPTER 3

GLOBAL COORDINATE MODEL

3.1 Introduction

We present here a dynamic link model based on the generalization of classical beam theory to capture the response of large-deflected compliant mechanisms. The classical beam theory (originated by Daniel Bernoulli) assumes that a straight line transverse to the axis of the beam before deformation remains *straight, inextensible, and normal to the mid-plane* after deformation. Another important but implicit assumption for classical beam theory is that *the deflection must be small*. Rayleigh [1945] latter included the rotatory inertia in the equation of motion. Timoshenko [1922] further revealed that the effect of rotatory inertia is small for low frequency vibration but at high frequency the shear stress deformation is comparable to rotatory inertia. However, in order to derive a solvable linear differential equation, the above classical theory and its subsequent modifications approximate the curvature of the link:

$$\frac{d\psi}{ds} \approx \frac{d^2y}{dx^2} \quad (3.1)$$

where ψ is the angle of rotation of the link; and s is the arc length from origin to point (x,y) of the link. The approximation in Equation (3.1) is only valid for $dy/dx \ll 1$ and hence, the classical beam theory is limited to small link deflections.

The difficulty to describe the motion of links undergoing large deflection lies on proper relations between the angle of rotation ψ and the coordinate variables (x, y) . This is because the curvature $d\psi/ds$ is needed to describe the strain energy in addition to the coordinate variables needed to express the kinetic energy. In order to characterize the dynamics of a compliant mechanism, a geometrically exact curvature formula is necessary. The exact curvature equation that can describe dynamics of a large-deflected link can be found in most calculus textbooks:

$$\frac{d\psi}{ds} = \frac{d^2 y / dx^2}{[1 + (dy / dx)^2]^{3/2}} \quad (3.2)$$

When the deflection is small, i.e., $dy/dx \ll 1$, Equation (3.2) reduces to Equation (3.1). Equation (3.2) has been used in several papers to formulate the dynamic equations of a link, such as Reddy *et al.* [1981] and Monasa *et al.* [1983]. However, as pointed out by Hodges [1984], Equation (3.2) defines the curvature along the coordinate x , which is on the undeflected position of the neutral axis. It does not take into account the well-known shortening effect due to transverse deflections. This resulting error is often unacceptable in many applications where large deflection is of particular concern. In order to overcome this problem, we can parameterize x and y by the arc length s . This leads to another curvature equation;

$$\frac{d\psi}{ds} = (x'y'' - x''y') \quad (3.3)$$

where $x=x(s)$, $y=y(s)$, and the prime denotes derivative with respect to s . Equation (3.3) has been used by Wagner [1965] to derive the dynamic equations of a large-deflected beam, where the square of Equation (3.3) is substituted into the strain energy function of the beam in deriving the governing equations based on Hamilton's principle. However,

the resulting equations are highly coupled and cannot account for shear and axial deformation of the link.

Based on the observations of previous curvature expressions, we develop a geometrically accurate relation between the angle of rotation and coordinate variables that can be easily incorporated in the dynamic model of large-deflected links. While the previous angle of rotation cannot fully solve the problem of large deflection with shear deformation (see Equations (3.1)~(3.3)), this chapter provides two constraint equations in the derivation of dynamical equations so that angle of rotation induced by bending and shear can both be accommodated.

The model introduced here accounts for the effects of link compliance on the dynamic response. Specifically, this chapter offers the following:

1. *A distributed-parameter dynamic model to predict the motion of a large-deflected link.* The model accounts for bending, shear, and axial deformation by incorporating geometric constraint equations to characterize the nonlinear kinematics of deformed links.
2. *A method that numerically solves the governing equations of a compliant link.* The method consists of two parts; time domain and spatial domain. In the time domain we use Newmark algorithm and in spatial domain we use generalized multiple shooting method (GMSM).
3. *A systematic procedure for modeling compliant serial mechanisms.* This procedure can deal with both closed and open chain, clamped and revolute joints.

3.2 Global Coordinate Model for Compliant Mechanisms

The dynamic model of a compliant mechanism is formulated in two steps. First, we propose the global coordinate model for analyzing a compliant link. Second, we extend the formulation for general compliant mechanisms by introducing constraint equations at the joints that connect two links together.

3.2.1 Global coordinate model (GCM) for a compliant link

As mentioned above, key to the formulation are two geometric constraint functions that relate the deformation and coordinate variables. In addition, we incorporate the constraint equations in the variational form and apply Hamilton's principle to derive the governing equations of the link. While some popular methods for analyzing compliant mechanisms are based on a floating frame attached to each link, the model introduced here requires only the inertia frame so that it is called the global coordinate model.

Geometric constraints

Figure 3.1 shows a (initially straight) deflected link of length L in the reference frame x - y . In order to fully describe the deflected shape, we define ψ as the initial rotation of the link plus deflection angle induced by bending, and γ as the shear angle. Hence the total angle of rotation is $\psi + \gamma$. Figure 3.2(a) shows an infinitesimal segment ds of the link, the coordinate of which can therefore be described by its geometric center (x, y) and the orientation $\psi + \gamma$. We also introduce the axial deformation variable e so that the distance between two adjacent infinitesimal segments is $ds + de$. The variables x , y , γ , ψ , and e are functions of arc length s and time t . They can be expressed explicitly as $x(s, t)$ and $y(s, t)$, etc.

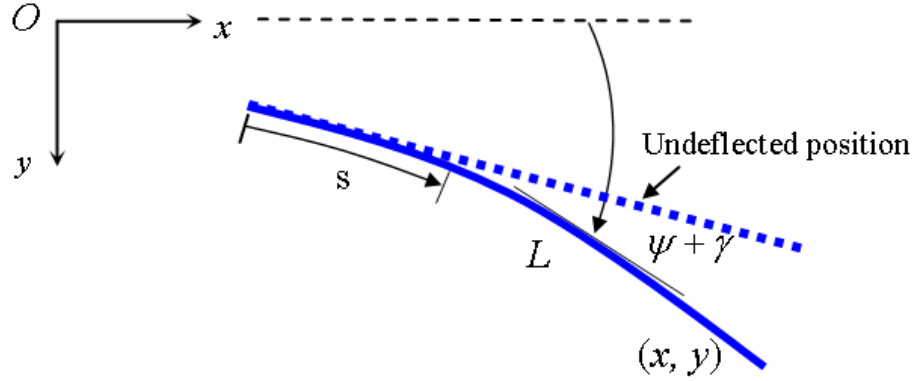


Figure 3.1 Schematic of a compliant link

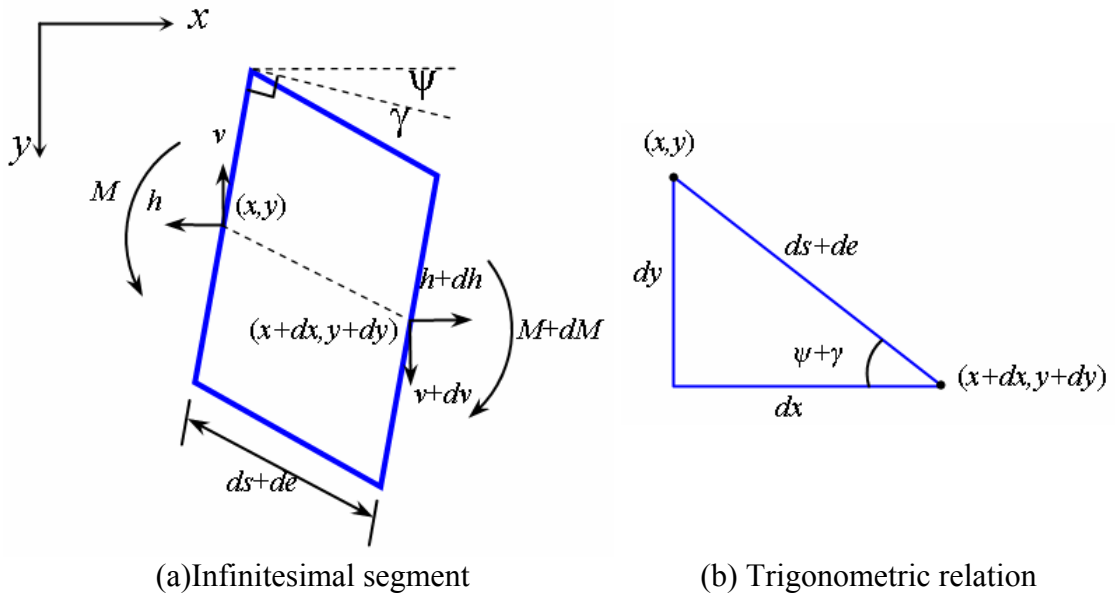


Figure 3.2 Schematic of an infinitesimal segment

Since the plane motion has only three degree-of-freedom, three of the five variables (x, y, ψ, γ, e) are independent. The trigonometry relating the coordinates (x, y) to deformation variables (ψ, γ, e) in the x - y frame can be derived with the aid of Figure 3.2(a) and are stated as two geometric constraints:

$$g_1 = x' - (e' + 1) \cos(\psi + \gamma) = 0 \quad (3.4a)$$

$$g_2 = y' - (e' + 1) \sin(\psi + \gamma) = 0 \quad (3.4b)$$

where prime denotes derivative with respect to arc length s . Compared with Equations (3.2) and (3.3), the shear angle γ and axial deformation e can be embedded in the two geometric constraints in Equation (3.4) easily. Note that Rao *et al.* [1989] have similar constraint equations but again their model cannot capture shear deformation.

At this point, rather than deriving the explicit expressions for ψ and γ from Equation (3.4), we show in the following paragraph that these two equations can be appended in the variational form by multiplying two Lagrange multipliers (h and v), which result from using more variables (five) than necessary (three).

Formulation using Hamilton's principle

With Equation (3.4), the equation of motion of the link can be systematically derived using Hamilton's principle, where the following variational form holds:

$$\int_{t_1}^{t_2} (\delta K - \delta V + \delta W^{nc} - h\delta g_1 - v\delta g_2) dt = 0 \quad (3.5)$$

where K and V are the kinetic and potential energy of the link respectively; δW^{nc} is the virtual work done by non-conservative forces; and t_1 and t_2 are two arbitrary instants of time. Note that we can append $h\delta g_1$ and $v\delta g_2$ in Equation (3.5) since g_1 and g_2 are identically zero. With h and v , we have enough independent variables (five) for the variational procedure.

Following the standard procedure of Hamilton's principle, we first form the total kinetic energy of the link as

$$K = \frac{1}{2} \int_0^L [I_\rho \dot{\psi}^2 + A_\rho (\dot{x}^2 + \dot{y}^2)] ds \quad (3.6)$$

where I_ρ is moment of inertia of the link; ψ is the angle of rotation induced by bending moment; A_ρ is mass per unit length; and the dot over the variable denotes the time derivative of the variable.

Similarly, the potential (strain) energy of the beam can also be expressed as

$$V = \frac{1}{2} \int_0^L \left[EI(\psi')^2 + \kappa GA\gamma^2 + EA(e')^2 \right] ds \quad (3.7)$$

where A is the cross-section area and I is the moment of area; E and G are the moduli of elasticity and shear respectively; κ is the shear correction factor; γ is the shear angle; and e is the axial elongation. The 1st, 2nd, and 3rd terms of Equation (3.7) represent the strain energy due to bending, shear, and axial deformations respectively.

Equations (3.6) and (3.7) express the kinetic and potential energy functions in standard quadratic forms. The nonconservative forces applied at the link may include dissipative forces proportional to the angular and linear velocities. As an illustration, we use mass proportional damping model to formulate the nonconservative forces as follows:

$$\delta W^{nc} = - \int_0^L \sigma (I_\rho \dot{\psi} \delta \psi + A_\rho \dot{x} \delta x + A_\rho \dot{y} \delta y) ds \quad (3.8)$$

where σ is the damping coefficient.

The resulting system of partial differential equations that governs the dynamics of the large-deflected link can be obtained using standard manipulations of variational calculus [Weinstock, 1974]. Detailed derivations are presented in Appendix B. After obtaining the governing equations, we further introduce non-dimensional independent variable $u = s / L \in [0,1]$ to replace s so that $x(s,t) = x(u,t)$ and $x' = dx/du$, etc. The equations can be written as follows after normalization.

$$\frac{EI}{L^2}\psi'' - I_\rho(\ddot{\psi} + \sigma\dot{\psi}) + v\left(\frac{e'}{L} + 1\right)\cos(\psi + \gamma) - h\left(\frac{e'}{L} + 1\right)\sin(\psi + \gamma) = 0 \quad (3.9a)$$

$$LA_\rho(\ddot{x} + \sigma\dot{x}) - h' = 0; LA_\rho(\ddot{y} + \sigma\dot{y}) - v' = 0 \quad (3.9b,c)$$

$$x' - (L + e')\cos(\psi + \gamma) = 0; y' - (L + e')\sin(\psi + \gamma) = 0 \quad (3.9d,e)$$

$$EAe'' - L[h\cos(\psi + \gamma) + v\sin(\psi + \gamma)]' = 0 \quad (3.9f)$$

$$[v(e' + L)\cos(\psi + \gamma) - h(e' + L)\sin(\psi + \gamma)] - L\kappa GA\gamma = 0 \quad (3.9g)$$

From the observation of Equation (3.9b,c), the Lagrange multipliers h and v turn out to be the internal forces acting on an infinitesimal segment in the positive x and y directions as shown in Figure 3.2(a). The physical interpretations of Equation (3.9) are stated as follows:

1. Equation (3.9a) is the moment balance equation. The rotational inertia in the term is often small, and can be neglected in structural applications. Without deformation, this equation can be reduced to the one that governs rigid-body rotation.
2. Equations (3.9b,c) are the results of applying Newton's 2nd law to each infinitesimal segment directly.
3. Equations (3.9d,e) are the normalization of Equation (3.4). They must be solved simultaneously with the rest of Equation (3.9).
4. Equation (3.9f) is the force balance equation in the deformed axial direction. Without the angle of rotation, it reduces to the familiar 2nd order differential equation that governs the axial deformation of a link.
5. Equation (3.9g) states the shear stress-strain relation where the shear stress comes from the internal forces h and v .

Note that Equation (3.9) is already in the global frame. Hence no intermediate or local frames are needed. This is in contrast to those methods that based on floating frames (such as the corotational method or the floating frame method).

3.2.2 Global coordinate model for serial compliant mechanisms

The dynamical model for a compliant link presented in Subsection 3.2.1 can be further extended to analyze mechanisms with compliant members. Since the dynamic model of a compliant link has already based on the inertia frame, we can derive the governing equations of links and their associated constraints without introducing intermediate or local frames since all of them share the same (inertia) frame x - y .

Consider a generic compliant mechanism shown in Figure 3.3. The ℓ links are connected in series by $\ell + 1$ joints where the 0^{th} and $(\ell + 1)^{th}$ joint are ground joints (rigid structure). Each link is governed by one set of Equation (3.9) rewritten as follows:

$$\frac{E_i I_i}{L_i^2} \psi_i'' - I_{\rho_i} \ddot{\psi}_i + v_i \left(\frac{e'_i}{L_i} + 1 \right) \cos(\psi_i + \gamma_i) - h_i \left(\frac{e'_i}{L_i} + 1 \right) \sin(\psi_i + \gamma_i) = 0 \quad (3.10a)$$

$$L_i A_{\rho_i} \ddot{x}_i - h'_i = 0 ; L_i A_{\rho_i} \ddot{y}_i - v'_i = 0 \quad (3.10b,c)$$

$$x'_i - (L_i + e'_i) \cos(\psi_i + \gamma_i) = 0 ; y'_i - (L_i + e'_i) \sin(\psi_i + \gamma_i) = 0 \quad (3.10d,e)$$

$$E_i A_i e''_i - L_i [h_i \cos(\psi_i + \gamma_i) + v_i \sin(\psi_i + \gamma_i)]' = 0 \quad (3.10f)$$

$$[v_i (e'_i + L_i) \cos(\psi_i + \gamma_i) - h_i (e'_i + L_i) \sin(\psi_i + \gamma_i)] - L_i \kappa_i G_i A_i \gamma_i = 0 \quad (3.10g)$$

where the subscript i is with respect to the i^{th} link. Equation (3.10) includes seven variables for one link. For a mechanism with ℓ links we have 7ℓ variables. These variables are constrained by the $\ell + 1$ joints connecting the links. Those constraints at the joints can be expressed as algebraic equations that must be valid for all time. For clarity

we list the constraint equations in the Tables 3.1~3.3. Table 3.1 lists the constraint equations for a typical joint which connects two links together. Both revolute and clamped joints are considered. For a revolute joint both links cannot resist moment and for a clamped joint their moments must balance along with angles of rotation. We list in Tables 3.2 and 3.3 constraint equations for joints that connect end links to ground, referred here as ground joints. Three different types of ground joints are considered, namely fixed, free, and prismatic joints.

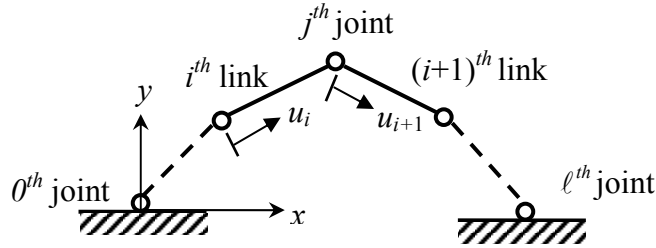


Figure 3.3 A generic serial compliant mechanism

Table 3.1 Constraint equations at a typical joint (1 to $\ell - 1$)

$\begin{cases} \psi'_i(1) = 0 & \psi'_{i+1}(0) = 0 \\ \psi_i(1) - \psi_{i+1}(0) = \text{constant} & \frac{E_i I_i}{L_i} \psi'_i(1) - \frac{E_{i+1} I_{i+1}}{L_{i+1}} \psi'_{i+1}(0) = 0 \end{cases}$		Revolute
		Clamped
$h_i(1) - h_{i+1}(0) = 0; v_i(1) - v_{i+1}(0) = 0$		
$x_i(1) - x_{i+1}(0) = 0; y_i(1) - y_{i+1}(0) = 0$		
$E_i A_i e'_i(1) - [h_i \cos(\psi_i + \gamma_i) + v_i \sin(\psi_i + \gamma_i)]_{u_i=1} = 0$		
$e_{i+1}(0) = 0$		

Table 3.2 Constraint equations at the 0^{th} joint

Fixed	Free	Prismatic
$\begin{cases} \psi'_1(0) = M & \text{moment input} \\ \psi_1(0) = \phi & \text{angle input} \\ \psi_1(0) = \text{constant} & \text{clamped} \end{cases}$	$\begin{cases} \psi'_1(0) = 0 \\ h_1(0) = 0 \\ v_1(0) = 0 \\ e_1(0) = 0 \end{cases}$	$\begin{cases} \psi'_1(0) = 0 & \text{revolute} \\ \psi_1(0) = \text{constant} & \text{clamped} \end{cases}$
$x_1(0) = 0$	$h_1(0) = 0$	$h_1(0) = 0$ or $v_1(0) = 0$
$y_1(0) = 0$	$v_1(0) = 0$	$x_1(0) = 0$ or $y_1(0) = 0$
$e_1(0) = 0$	$e_1(0) = 0$	$e_1(0) = 0$

Table 3.3 Constraint equations at the ℓ^{th} joint

Fixed	Free	Prismatic
$\begin{cases} \psi'_\ell(1) = M & \text{moment input} \\ \psi_\ell(1) = \phi & \text{angle input} \\ \psi_\ell(1) = \text{constant} & \text{clamped} \end{cases}$	$\psi'_\ell(1) = 0$	$\begin{cases} \psi'_\ell(1) = 0 & \text{revolute} \\ \psi_\ell(1) = \text{constant} & \text{clamped} \end{cases}$
$x_\ell(1) = 0$	$h_\ell(1) = 0$	$h_\ell(1) = 0 \text{ or } v_\ell(1) = 0$
$y_\ell(1) = 0$	$v_\ell(1) = 0$	$x_\ell(1) = 0 \text{ or } y_\ell(1) = 0$
$E_\ell A_\ell e'_\ell(1) - [h_\ell \cos(\psi_\ell + \gamma_\ell) + v_\ell \sin(\psi_\ell + \gamma_\ell)]_{u=1} = 0$	$e'_\ell(1) = 0$	$E_\ell A_\ell e'_\ell(1) - [v_\ell \sin(\psi_\ell + \gamma_\ell)]_{u=1} = 0$ or $E_\ell A_\ell e'_\ell(1) - [h_\ell \cos(\psi_\ell + \gamma_\ell)]_{u=1} = 0$

Hence at a typical joint (revolute or clamped) there are eight constraint equations and at a ground joint there are four constraint equations.

Equation (3.10) and the constraint equations in Tables 3.1~3.3 form the necessary equations to solve for a compliant mechanism. Note that while developed for serial compliant mechanisms, the dynamic model can be extended for parallel compliant mechanisms as well.

3.3 Numerical Approximation

Equation (3.10) with the constraint equations in Tables 3.1~3.3 is a system of nonlinear hyperbolic equations with differential constraint equations. We present here a semi-discrete method to solve them numerically. Specifically, the spatial domain u_i is solved using the generalized multiple shooting method while the temporal domain t is solved with Newmark family of integration schemes.

3.3.1 Temporal approximation: Newmark integration scheme

Motivated by stability considerations, we use the Newmark family of time integration schemes [Newmark, 1959] for temporal discretization. Let the position Z^k , its

velocity \dot{Z}^k , and acceleration \ddot{Z}^k denote the approximate solution to $z(t^k, u)$, $\dot{z}(t^k, u)$, and $\ddot{z}(t^k, u)$ at time level t^k and $u \in [0,1]$ respectively. Assume the solutions of Z^k , \dot{Z}^k , and \ddot{Z}^k have been obtained, the Newmark method is an implicit scheme that finds the approximate solution at next time level t^{k+1} according to the following formulae:

$$\ddot{Z}^{k+1} = \frac{2}{a_2(\Delta t)^2}(Z^{k+1} - Z^k) - \frac{2}{a_2\Delta t}\dot{Z}^k - \left(\frac{1}{a_2} - 1\right)\ddot{Z}^k \quad (3.11a)$$

$$\dot{Z}^{k+1} = \dot{Z}^k + (1 - a_1)\Delta t\ddot{Z}^k + a_1\Delta t\ddot{Z}^{k+1} \quad (3.11b)$$

where $\Delta t = t^{k+1} - t^k$ denotes the time step size and (a_1, a_2) are Newmark parameters that determine the stability and accuracy of the scheme. By applying Equation (3.11a), the terms involving time derivatives in Equation (3.10) can be discretized in the time domain. Here we use upper cases to represent the approximate solutions of dependent variables (in lower cases) as following:

$$\Psi_i^k \approx \psi_i(t^k, u_i); H_i^k \approx h_i(t^k, u_i); V_i^k \approx v_i(t^k, u_i);$$

$$X_i^k \approx x_i(t^k, u_i); Y_i^k \approx y_i(t^k, u_i); E_i^k \approx e_i(t^k, u_i) \text{ and } \Gamma_i^k \approx \gamma_i(t^k, u_i).$$

Using the approximate solutions, the discretized differential equations at t^{k+1} of Equation (3.10) can be written as follows:

$$\begin{aligned} & \frac{E_i I_i}{L_i^2}(\Psi_i^{k+1} - \Psi_i^k) - I_{\rho_i} \left[\frac{2}{a_2(\Delta t)^2}(\Psi_i^{k+1} - \Psi_i^k) - \frac{2}{a_2\Delta t}\dot{\Psi}_i^k - \left(\frac{1}{a_2} - 1\right)\ddot{\Psi}_i^k \right] \\ & + V_i^{k+1} \left[\frac{(E_i')^{k+1}}{L_i} + 1 \right] \cos(\Psi_i^{k+1} + \Gamma_i^{k+1}) - H_i^{k+1} \left[\frac{(E_i')^{k+1}}{L_i} + 1 \right] \sin(\Psi_i^{k+1} + \Gamma_i^{k+1}) = 0 \end{aligned} \quad (3.12a)$$

$$L_i A_{\rho_i} \left[\frac{2}{a_2(\Delta t)^2}(X_i^{k+1} - X_i^k) - \frac{2}{a_2\Delta t}\dot{X}_i^k - \left(\frac{1}{a_2} - 1\right)\ddot{X}_i^k \right] - (H_i')^{k+1} = 0 \quad (3.12b)$$

$$L_i A_{\rho_i} \left[\frac{2}{a_2 (\Delta t)^2} (Y_i^{k+1} - Y_i^k) - \frac{2}{a_2 \Delta t} \dot{Y}_i^k - \left(\frac{1}{a_2} - 1 \right) \ddot{Y}_i^k \right] - (V_i')^{k+1} = 0 \quad (3.12c)$$

$$(X_i')^{k+1} = [L_i + (E_i')^{k+1}] \cos(\Psi_i^{k+1} + \Gamma_i^{k+1}); \quad (3.12d)$$

$$(Y_i')^{k+1} = [L_i + (E_i')^{k+1}] \sin(\Psi_i^{k+1} + \Gamma_i^{k+1}) \quad (3.12e)$$

$$\begin{aligned} E_i A_i (E_i')^{k+1} - L_i [(H_i')^{k+1} + V_i^{k+1} (\Psi_i')^{k+1} + V_i^{k+1} (\Gamma_i')^{k+1}] \cos(\Psi_i^{k+1} + \Gamma_i^{k+1}) \\ - L_i [(V_i')^{k+1} - H_i^{k+1} (\Psi_i')^{k+1} - H_i^{k+1} (\Gamma_i')^{k+1}] \sin(\Psi_i^{k+1} + \Gamma_i^{k+1}) = 0 \end{aligned} \quad (3.12f)$$

$$\begin{aligned} V_i^{k+1} [(E_i')^{k+1} + L_i] \cos(\Psi_i^{k+1} + \Gamma_i^{k+1}) - H_i^{k+1} [(E_i')^{k+1} + L_i] \sin(\Psi_i^{k+1} + \Gamma_i^{k+1}) \\ - L_i \kappa_i G_i A_i \gamma_i = 0 \end{aligned} \quad (3.12g)$$

Equation (3.12) is a system of time-independent ordinary differential equations (ODE's) involving unknown functions Ψ_i^{k+1} , H_i^{k+1} , V_i^{k+1} , X_i^{k+1} , Y_i^{k+1} , E_i^{k+1} , and Γ_i^{k+1} .

The method to solve Equation (3.12) will be presented in Subsection 3.3.2.

At the end of time step $k+1$, the approximate functions $(\dot{\Psi}_i^{k+1}, \ddot{\Psi}_i^{k+1})$, $(\dot{X}_i^{k+1}, \ddot{X}_i^{k+1})$, and $(\dot{Y}_i^{k+1}, \ddot{Y}_i^{k+1})$ will be computed by using Equation (3.11). Note that the calculation of Equation (3.12) requires knowledge of the initial conditions $(\Psi_i^0, \dot{\Psi}_i^0, \ddot{\Psi}_i^0)$, $(X_i^0, \dot{X}_i^0, \ddot{X}_i^0)$ and $(Y_i^0, \dot{Y}_i^0, \ddot{Y}_i^0)$. The initial positions and velocities will be given and the initial accelerations can be obtained by assuming zero applied force at $t=0$.

$$\ddot{\Psi}_i^0 = \frac{EI_i}{L_i^2 I_{\rho_i}} (\Psi_i'')^0, \quad \ddot{X}_i^0 = 0, \quad \ddot{Y}_i^0 = 0 \quad (3.13)$$

3.3.2 Spatial approximation: generalized multiple shooting method

After temporal discretization, the governing equation reduces to the nonlinear boundary value problem represented by Equation (3.12). We propose in this section an

improved numerical formulation called generalized multiple shooting method (GMSM) to solve for the spatial domain.

The generalized shooting method introduced in Chapter 2 offers simple formulation with higher order accuracy, but it has the following two major problems in implementation.

(a) When solving Equation (2.1) with wrong initial guesses μ_u and ξ , the solution may not exist for all $0 \leq u_i \leq 1$, i.e., it becomes unbounded before u reaches 1. In such case, there is no way to correct μ_u and ξ because the iteration fails.

(b) The solution accuracy relies on the order of the space marching scheme used.

However, all such schemes suffer the same problem of round-off error accumulation. In Chapter 2, we presented the Bounded Gauss-Newton method to overcome the problem of wrong initial guesses provided the ranges of initial guesses are known in advance. In addition, the problem of round-off errors can be alleviated by using higher order schemes (such as ode45 in MATLAB) without sacrificing computation time (as shown in Figure 2.13). However, we will introduce in the following subsection a unified approach that solves the above two problems at the same time.

Generalized multiple shooting method (GMSM)

The above two problems of GSM both result from relatively lengthy integration interval. This leads to the idea of shortening the interval for shooting. Consider the following system of ℓ coupled, normalized sets of 1st order ODE's:

$$\begin{bmatrix} \mathbf{M}_1 \mathbf{q}'_1 \\ \vdots \\ \mathbf{M}_\ell \mathbf{q}'_\ell \end{bmatrix} = \begin{bmatrix} \mathbf{f}_1(u_1, \mathbf{q}_1, \xi_1) \\ \vdots \\ \mathbf{f}_\ell(u_\ell, \mathbf{q}_\ell, \xi_\ell) \end{bmatrix} \quad (3.14)$$

where $\mathbf{M}_i(u_i, \mathbf{q}_i)$ is the coefficient (mass) matrix of the i^{th} set of ODE. Equation (2.1) can be regarded as a special case of Equation (3.14) where $\mathbf{M}_i = \mathbf{I}_i$. We divide the interval of integration $[0 \ 1]$ of Equation (2.1) into N subintervals with $N+1$ nodes.

$$0 = u_{i1} < u_{i2} < \cdots < u_{ij} < \cdots < u_{iN} < u_{i,N+1} = 1; \ i = 1 \sim \ell \text{ and } j = 1 \sim N+1$$

The symbol u_{ij} denotes the normalized arc length of the j^{th} node in the i^{th} link. A single shooting method is performed in each subinterval of each link so that the resulting solution segments are connected to form a continuous solution over $[0 \ 1]$. Figure 3.4 shows the idea of multiple shooting.

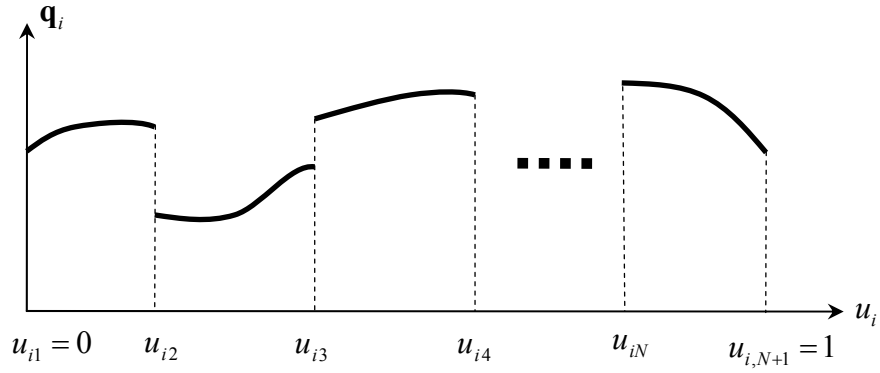


Figure 3.4 Multiple shooting method

Since shooting is performed more than once in the overall interval, the method is called multiple shooting. It is also called parallel shooting because shooting method is performed independently on each subinterval.

Similar to single shooting, each subinterval of the multiple shooting requires an initial value in order to integrate the ODE's. We denote the initial values of each subinterval as

$$\mathbf{q}(\mathbf{u}_j) = [\mathbf{q}_1^T(u_{1j}) \quad \dots \quad \mathbf{q}_i^T(u_{ij}) \quad \dots \quad \mathbf{q}_\ell^T(u_{\ell j})]^T = [\boldsymbol{\mu}_{1j}^T \quad \dots \quad \boldsymbol{\mu}_{ij}^T \quad \dots \quad \boldsymbol{\mu}_{\ell j}^T]^T = \boldsymbol{\mu}_j ;$$

$$1 \leq j \leq N$$

where $\boldsymbol{\mu}_j$ now is an $\ell n \times 1$ vector. Since these initial values are not known in advanced, we treat them as unknowns. For N subintervals we have $\ell n \times N$ unknown initial values

$$\boldsymbol{\mu} = [\boldsymbol{\mu}_1^T \quad \dots \quad \boldsymbol{\mu}_j^T \quad \dots \quad \boldsymbol{\mu}_N^T]^T$$

with r unknown parameters $\boldsymbol{\xi} = [\boldsymbol{\xi}_1^T, \boldsymbol{\xi}_2^T, \dots, \boldsymbol{\xi}_\ell^T]^T$. Hence there are totally $\ell n N + r$ unknowns. The equations corresponding to these unknowns are listed as follows:

(i) $\ell \times n$ boundary constraint equations

$$\mathbf{g}(\mathbf{q}(0), \mathbf{q}(1)) = 0 \quad (3.15a)$$

(ii) $(N-1)n\ell$ continuity equations that connect the solution segments together

$$\boldsymbol{\mu}_{j+1} = \mathbf{q}(\mathbf{u}_{j+1}; \boldsymbol{\mu}_j) \quad (3.15b)$$

We put $\boldsymbol{\mu}_j$ after the semicolon to express that in the j^{th} interval the function \mathbf{q} is a function of the initial value $\boldsymbol{\mu}_j$ of that interval.

(iii) r geometric constraint equations for r unknown parameters

$$\mathbf{g}(\boldsymbol{\mu}, \boldsymbol{\xi}) = 0 \quad (3.15c)$$

We are left to solve a set of $\ell n N + r$ nonlinear algebraic equations

$$\mathbf{F}(\boldsymbol{\mu}, \boldsymbol{\xi}) = \begin{bmatrix} \boldsymbol{\mu}_2 - \mathbf{q}(\mathbf{u}_2; \boldsymbol{\mu}_1) \\ \boldsymbol{\mu}_3 - \mathbf{q}(\mathbf{u}_3; \boldsymbol{\mu}_2) \\ \vdots \\ \boldsymbol{\mu}_N - \mathbf{q}(\mathbf{u}_N; \boldsymbol{\mu}_{N-1}) \\ \mathbf{g}(\boldsymbol{\mu}_1, \mathbf{q}(\mathbf{u}_{N+1}; \boldsymbol{\mu}_N)) \\ \mathbf{g}(\boldsymbol{\mu}, \boldsymbol{\xi}) \end{bmatrix} = 0 \quad (3.16)$$

In summary, the GSM includes four steps:

- (i) Recast the BVP in a state-space form as Equation (3.14).
- (ii) Identify unknown initial values and parameters.
- (iii) Formulate constraint and continuity equations from Equation (3.15).
- (iv) Integrate Equation (3.14) and solve for unknowns in Equation (3.16).

The GSM can be solved iteratively by methods such as Newton's or Quasi-Newton, where Equation (3.14) is integrated in each iteration.

3.3.3 Application to the global coordinate model

By defining $\mathbf{q}_i = [\Psi_{i1}^{k+1} \quad \Psi_{i2}^{k+1} \quad H_i^{k+1} \quad V_i^{k+1} \quad X_i^{k+1} \quad Y_i^{k+1} \quad E_{i1}^{k+1} \quad E_{i2}^{k+1} \quad \Gamma_i^{k+1}]^T$,

we can recast Equation (3.12) in the form of Equation (3.14) as

$$\mathbf{M}_i \mathbf{q}'_i = \begin{bmatrix} \frac{L_i^2}{E_i I_i} \left\{ I_{\rho_i} \left[\frac{2}{a_2 (\Delta t)^2} (\Psi_{i1}^{k+1} - \Psi_{i1}^k) - \frac{2}{a_2 \Delta t} \dot{\Psi}_{i1}^k - \left(\frac{1}{a_2} - 1 \right) \ddot{\Psi}_{i1}^k \right] - \left(\frac{E_{i2}^{k+1}}{L_i} + 1 \right) [V_i^{k+1} \cos(\Psi_{i1}^{k+1} + \Gamma_i^{k+1}) - H_i^{k+1} \sin(\Psi_{i1}^{k+1} + \Gamma_i^{k+1})] \right\} \\ L_i A_{\rho_i} \left[\frac{2}{a_2 (\Delta t)^2} (X_i^{k+1} - X_i^k) - \frac{2}{a_2 \Delta t} \dot{X}_i^k - \left(\frac{1}{a_2} - 1 \right) \ddot{X}_i^k \right] \\ L_i A_{\rho_i} \left[\frac{2}{a_2 (\Delta t)^2} (Y_i^{k+1} - Y_i^k) - \frac{2}{a_2 \Delta t} \dot{Y}_i^k - \left(\frac{1}{a_2} - 1 \right) \ddot{Y}_i^k \right] \\ (L_i + E_{i2}^{k+1}) \cos(\Psi_{i1}^{k+1} + \Gamma_i^{k+1}) \\ (L_i + E_{i2}^{k+1}) \sin(\Psi_{i1}^{k+1} + \Gamma_i^{k+1}) \\ E_{i2}^{k+1} \\ \frac{L_i}{E_i A_i} \left[-H_i^{k+1} \Psi_{i2}^{k+1} \sin(\Psi_{i1}^{k+1} + \Gamma_i^{k+1}) + V_i^{k+1} \Psi_{i2}^{k+1} \cos(\Psi_{i1}^{k+1} + \Gamma_i^{k+1}) \right] \\ V_i^{k+1} (E_{i2}^{k+1} + L_i) \cos(\Psi_{i1}^{k+1} + \Gamma_i^{k+1}) - H_i^{k+1} (E_{i2}^{k+1} + L_i) \sin(\Psi_{i1}^{k+1} + \Gamma_i^{k+1}) - L_i \kappa_i G_i A_i \gamma_i \end{bmatrix} \quad (3.17)$$

where the nonzero entries of \mathbf{M}_i are

$$M_i(k, k) = 1, k = 1 \sim 8;$$

$$M_i(8, 3) = -L_i \cos(\Psi_i^{k+1} + \Gamma_i^{k+1}); \quad M_i(8, 4) = -L_i \cos(\Psi_i^{k+1} + \Gamma_i^{k+1}); \quad \text{and}$$

$$M_i(8, 9) = -L_i [V_i^{k+1} \cos(\Psi_i^{k+1} + \Gamma_i^{k+1}) - H_i^{k+1} \sin(\Psi_i^{k+1} + \Gamma_i^{k+1})].$$

Note that \mathbf{M}_i now is a singular matrix because the last row of Equation (3.17) is an algebraic equation with $M_i(9,9)=0$. A set of ODE's with a singular \mathbf{M} is also known as the differential-algebraic equations (DAE's). Equation (3.17) is defined as a system of DAE's of index 1. For definitions of DAE indexes, please refer to [Ascher, 1988]. Although numerical techniques for solving ODE's and DAE's are different, MATLAB provides ODE solvers (ode15s, ode23t) that can solve a DAE with index 1 [Shampine, 1997].

There are $n=8$ first order differential equations in Equation (3.17) that governs the deformation of the link. We then divide the link into N subintervals. Each link (say, the i^{th} link) then has $8N$ unknown initial values at time step k as follows:

$$\mathbf{\mu}_{ij}^k = [\Psi_{i1}^{k+1}(u_{ij}) \quad \Psi_{i2}^{k+1}(u_{ij}) \quad H_i^{k+1}(u_{ij}) \quad V_i^{k+1}(u_{ij}) \quad X_i^{k+1}(u_{ij}) \quad Y_i^{k+1}(u_{ij}) \quad E_{i1}^{k+1}(u_{ij}) \quad E_{i2}^{k+1}(u_{ij})]^T;$$

$$1 \leq j \leq N$$

For a compliant mechanism with ℓ links there are $8N\ell$ unknown initial values. Note that the unknowns ξ are not involved since the integration of Equation (3.17) does not rely on unknown parameters as compared with Equation (2.1).

For a serial compliant mechanism, the boundary constraint equations corresponding to (i) in Subsection 3.3.2 are listed in Table 3.1, 3.2, and 3.3. Since a serial mechanism includes $\ell - 1$ typical joints with two ground joints (a typical joint provides eight equations and a ground joint provides four equations), the number of boundary constraint equations satisfies that required by the Generalized Multiple Shooting Method.

$$8(\ell - 1) + 2 * 4 = 8\ell$$

In addition, geometric constraint equations corresponding to (iii) are not required since there are no unknown parameters ξ in the dynamic global coordinate model expressed in

Equation (3.9). However, we will see in Chapter 5 that the internal forces h and v appear as unknown parameters in the static global coordinate model.

Once the above unknown initial values and constraint/continuity equations are established, Equation (3.17) can be integrated by Euler's method or higher order schemes such as family of Runge-Kutta methods. After integrating Equation (3.17), the function $\mathbf{F}(\boldsymbol{\mu})$ can be solved by an iterative method. Since explicit formulae for $\mathbf{F}(\boldsymbol{\mu})$ cannot be obtained, the Jacobian matrix has to be approximated numerically. Also, the Jacobian matrix requires the most expensive computation for the generalized multiple shooting method, the popular Newton method is not efficient. Instead we use Quasi-Newton method that requires only one evaluation of the Jacobian matrix in each time step. In summary, the steps for solving the dynamic response of compliant mechanism problem using generalized multiple shooting method are outlined as follows:

Computational Steps:

1. Given (a_1, a_2) with initial conditions $(\Psi_i^0, \dot{\Psi}_i^0, \ddot{\Psi}_i^0)$, $(X_i^0, \dot{X}_i^0, \ddot{X}_i^0)$ and $(Y_i^0, \dot{Y}_i^0, \ddot{Y}_i^0)$,
 $1 \leq i \leq \ell$
 2. For $k = 0 \sim \text{number of time steps}$
 - (I) Given initial guesses $\boldsymbol{\mu}^k$, obtain the Jacobian matrix of Equation (3.16) and residual $\mathbf{F}(\boldsymbol{\mu}^k)$, solve for $\boldsymbol{\mu}^k$ by Quasi-Newton method.
 - (II) After obtaining $\boldsymbol{\mu}^k$, integrate Equation (3.17) to get \mathbf{q} and calculate $(\dot{\Psi}^k, \ddot{\Psi}^k)$, (\dot{X}^k, \ddot{X}^k) , and (\dot{Y}^k, \ddot{Y}^k) from Equation (3.11). These values are required for the next time step.
- End

Note that although initial guesses are required for each time step, we can use the initial guesses for the previous time step to replace the initial guesses for the current step. Thus we only need to make initial guesses for the first time step.

3.4 Conclusions

A complete dynamic model has been presented for analyzing compliant links capable of large deflection. Specifically, we incorporate two geometric constraint equations in the derivation using Hamilton's principle so that bending, shear and axial deformations can be incorporated simultaneously. The resulting governing equations are based on the inertia frame so that it can be easily extended to multi-link analysis. Systematic procedures are presented to analyze compliant serial mechanisms whose joints can be either revolute or clamped. In addition, we developed a numerical method that combines a Newmark scheme with generalized shooting method to solve the equations.

CHAPTER 4

ILLUSTRATIVE EXAMPLES AND VALIDATIONS

4.1 Introduction

By using the numerical schemes described in Chapter 3, we illustrate the application of the global coordinate model by using five test examples. We validate the model of one compliant link using three examples. In the last two examples, we then demonstrate the capability of GCM in analyzing multi-link compliant mechanisms. Specifically, these examples are organized as follows:

I. A compliant link

- I.1 Free vibration of a compliant link
- I.2 Experiment validation of a compliant link with tip load
- I.3 A spinning rod

II Two compliant mechanisms

- II.1 Compliant slider-crank mechanism
- II.2 Compliant four-bar mechanism

Throughout these examples we use the constant average acceleration method where the Newmark parameters (a_1 , a_2) in Equation (3.15) are set to (0.5, 0.5). This method can be proved to be unconditionally stable for linear systems. However, as mentioned by Zienkiewicz [1977], if no other sources of damping are present in the problem, the lack of numerical damping can be cause unacceptable numerical noise in the

higher frequencies of the structure. He introduced a certain level of numerical damping by setting damping amplitude decay factor $\sigma > 0$ in the following equation.

$$a_1 = \frac{1}{2} + \sigma; a_2 = \frac{1}{2}(1 + \sigma)^2.$$

We set $\sigma = 0.005$ for all the following examples. Hence the Newmark parameters become $(a_1, a_2) = (0.5050, 0.5050)$.

4.2 Illustrative Examples

Example 1.1 Free vibration of a compliant link

We simulate the free vibration of a flexible steel rod in this example. The parameters for the rod are listed in Table 4.1. The rod is given an initial applied load at the tip and then released. We can readily apply the formulae in Subsection 3.3.2 and 3.3.3 to solve this problem. Figure 4.1 shows the tip displacement and Figure 4.2 shows the snapshots of the vibrating rod, which has a period approximately equal to 0.49 seconds.

Table 4.1 Simulation parameters and values for a steel rod

Simulation Parameters	Values
Density ρ	7850 kg/m ³
Dimension (LxWxT)	1.11x0.0127x0.0032 m
Young's Modulus E	200GPa
Shear Modulus G	80GPa
Time step size Δt	0.01 sec
Initial tip location	$[x(1), y(1)] = (1.0177\text{m}, 0.4061\text{m})$
Initial velocity $(\dot{\Psi}_0, \dot{X}_0, \dot{Y}_0)$	(0,0,0)

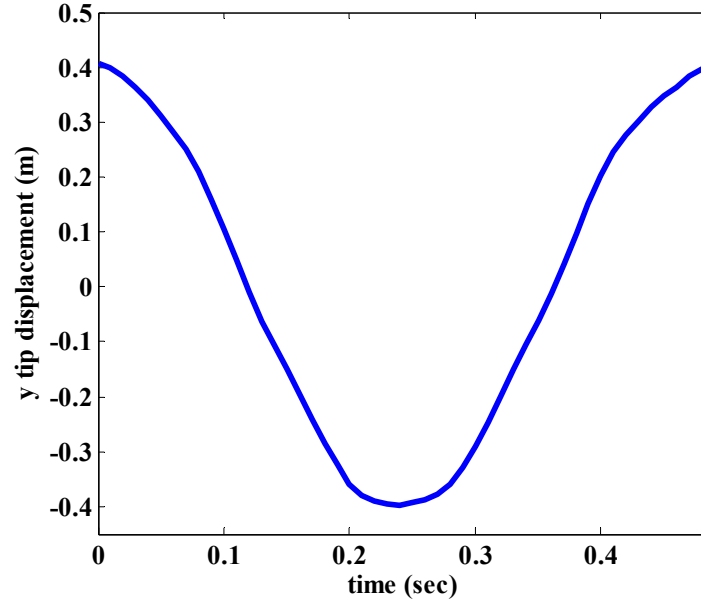


Figure 4.1 Beam tip displacement in one cycle

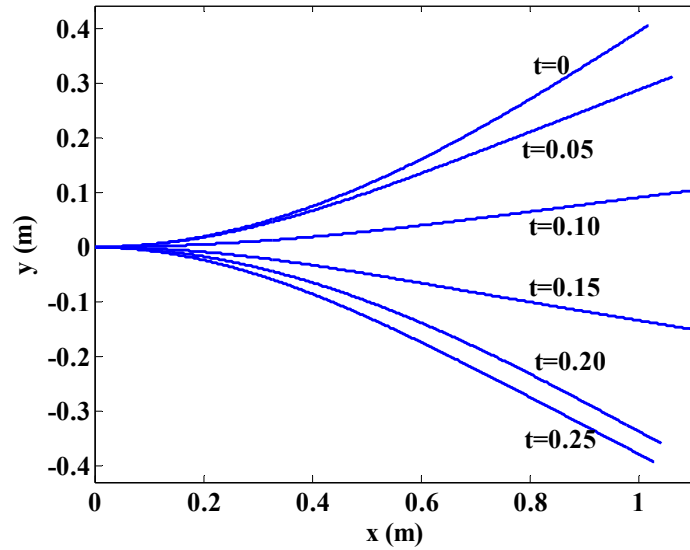


Figure 4.2 Snapshot of a free-vibrating beam

Figure 4.3 shows the kinetic energy distribution in one cycle. Clearly, the kinetic energy is dominated by the translational energy in the y direction, which is much larger than the rotational energy. For this reason the effect of rotational inertia has always been neglected in structural mechanic problems. Figure 4.4 shows the energy distribution

between kinetic and potential. It is worth noting that there is no energy loss during the temporal integration.

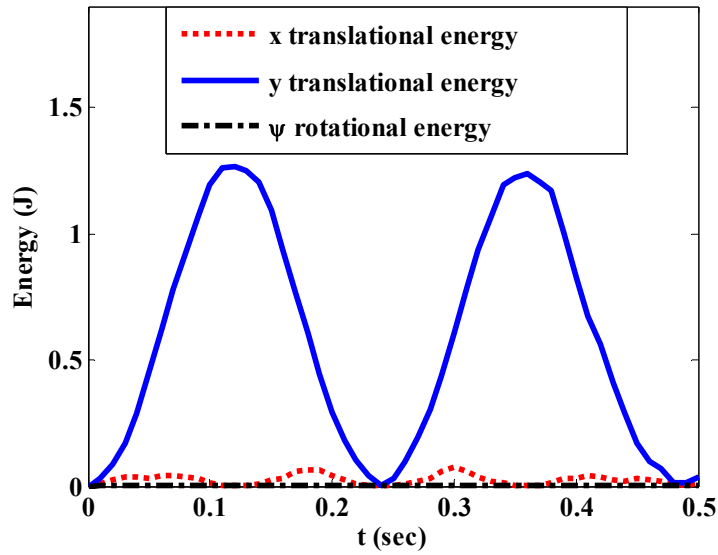


Figure 4.3 Kinetic energy of the vibrating beam

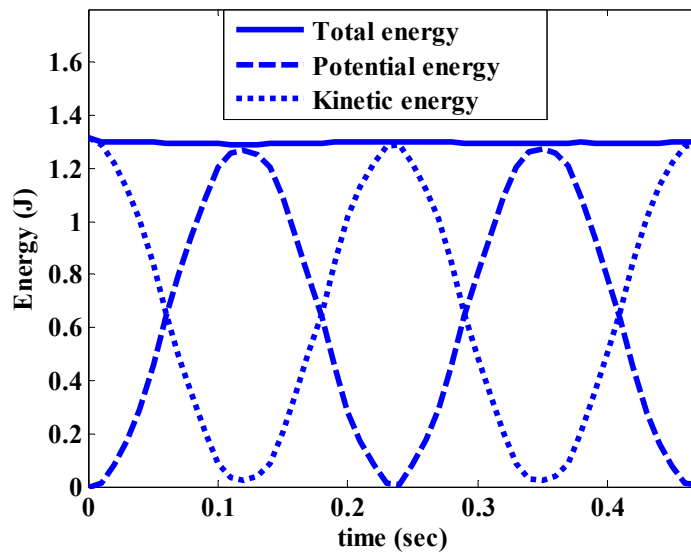


Figure 4.4 Energy balance of the beam

An experiment has also been conducted to measure the natural frequency of the steel rod whose parameters are listed in Table 4.1. As shown in Figure 4.5, the x direction of the rod is parallel to the direction of gravity so that the effect of weight is minimized.

A proximity sensor (Keyence EZ18T) is placed at the undeflected tip position such that it is ON if the tip of the rod approaches and OFF if not. The period of vibration can be recorded by adding two adjacent OFF time intervals. The period shown in Figure 4.6 is approximated 0.485 second which is very close to that predicted by the previous simulation result (0.49 second).

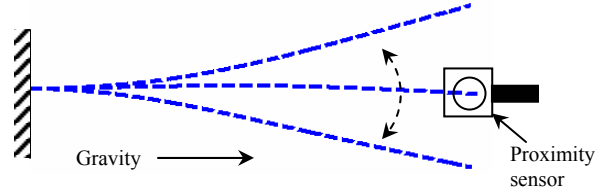


Figure 4.5 Experiment setup

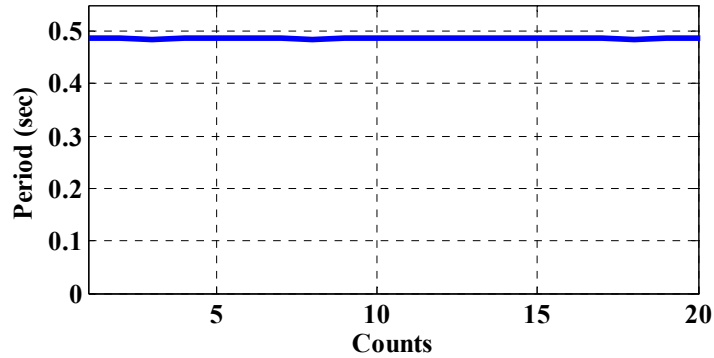


Figure 4.6 Period of a free vibrating steel rod

Example 1.2 Experiment validation of a compliant link with tip load

In order to validate the transient deflection of a compliant link, we compare the simulation result with the experiment obtained by Yoo *et. al.* [2003]. In their experiment shown in Figure 4.7, a spring steel rod is clamped at the base with an applied load m_0 at the tip. The beam with its tip load is released from the undeflected position. A high speed camera (REDLAKE, 125fps) is used to measure the deflection of the tip point.

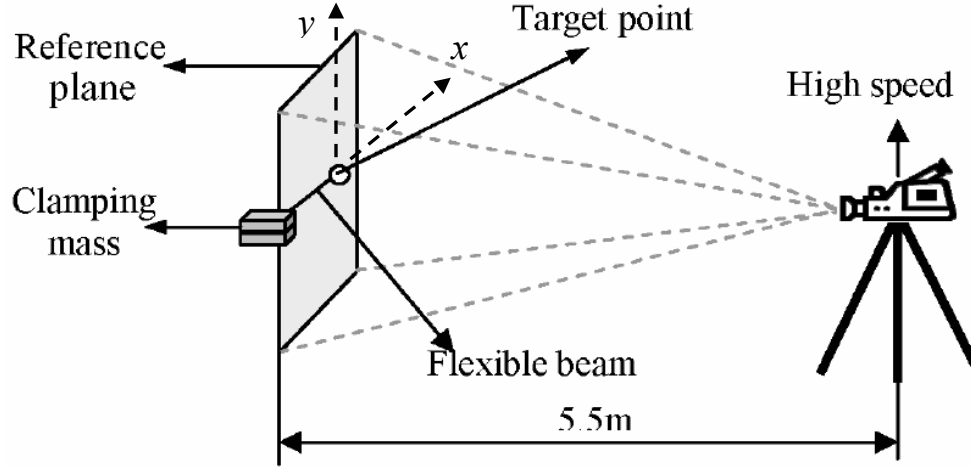


Figure 4.7 Experiment setup in Yoo *et. al.* [2003]

The parameters of the link are listed in Table 4.2. Two experiments are conducted; one with $m_0 = 20g$ and the other with $m_0 = 10g$. The equations of motion of the tip load are

$$-h(L) = m_0 \ddot{x}(L); -v(L) - m_0 g = m_0 \ddot{y}(L)$$

In the original experiment done by Yoo *et. al.* [2003], they use very small damping coefficients to account for aerodynamic and structural damping effects. However, as these effects are not obvious in the first few vibrations, we neglect the damping effect and compute using the global coordinate model. The results (solid) are compared with the experiment data (dotted) shown in Figures 4.8 and 4.9. Obviously the global coordinate model agrees well with the experiment.

Table 4.2 Simulation parameters and values for a spring steel rod

Simulation Parameters	Values
Density ρ	7919 kg/m ³
Length L	0.4 m
Cross-section area A	7.854x10 ⁻⁷ m ²
Moment of inertia I	4.909x10 ⁻¹⁴ m ⁴
Young's Modulus E	200GPa
Time step size Δt	0.005 sec
Initial tip location	(x, y) = (0.4m, 0m)
Initial velocity ($\dot{\Psi}_0, \dot{X}_0, \dot{Y}_0$)	(0,0,0)

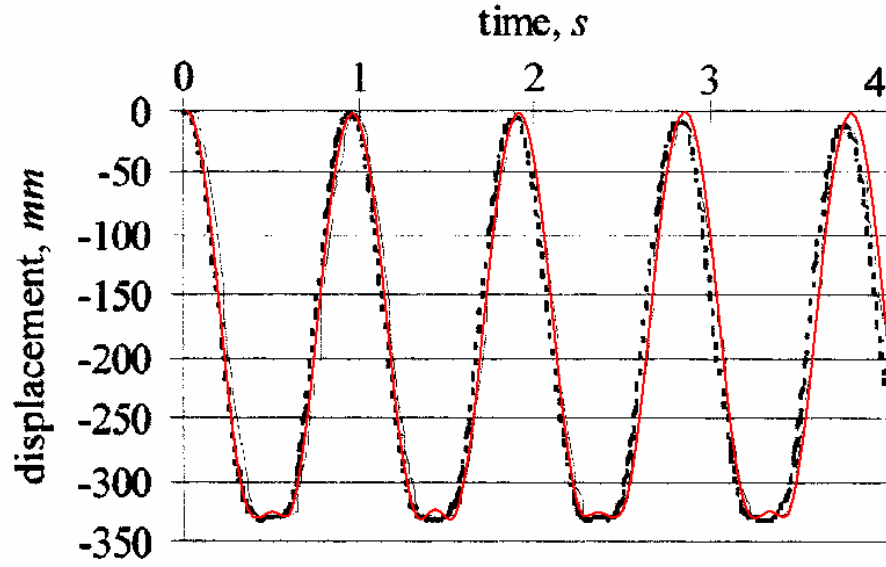


Figure 4.8 Comparison of simulation and experiment data with $m_0 = 20g$

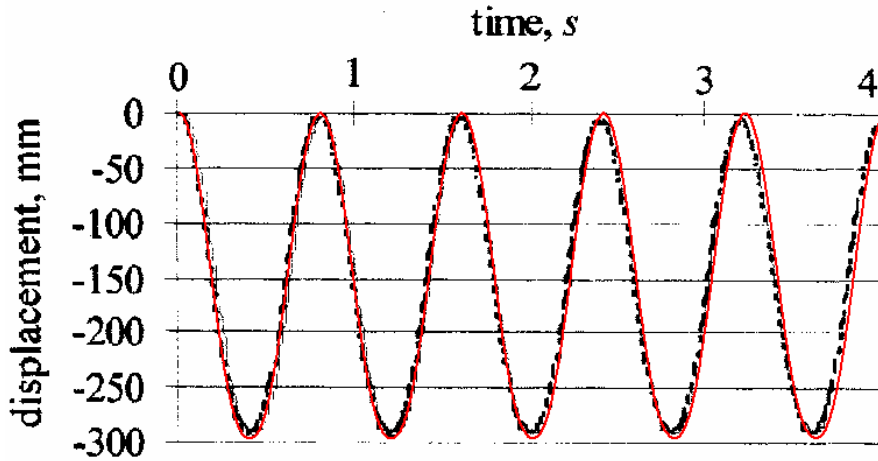


Figure 4.9 Comparison of simulation and experiment data with $m_0 = 10g$

Example I.3 A spinning rod

A high-speed rotating link has many applications such as helicopter blades, flexible robotic manipulators, and turbine blades. However, approaches that based on linear strain-deflection relationship (such as floating frame formulation) have been proved to cause instability when simulating a flexible rotating link [Kane, 1987]. As pointed out by Kane [1987], the instability of linear model is due to the neglect of the

coupling between longitudinal and transverse deformation (centrifugal stiffening effect). While many research work has been done to solve this problem (see [Berzeri and Shabana, 2002] for review), we demonstrate using this example that the global coordinate model can automatically account for centrifugal stiffening effect without further modifications.

Consider an originally straight rod attached to a hub as shown in Figure 4.10. The rod is given a prescribed angle input $\psi(0, t)$ at the base shown in Equation (4.1).

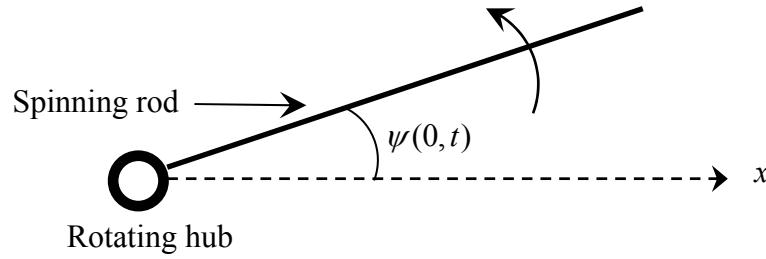


Figure 4.10 A spinning rod

$$\psi(0, t) = \begin{cases} \frac{\omega_s}{T_s} \left[\frac{1}{2} t^2 + \left(\frac{T_s}{2\pi} \right)^2 \left(\cos \left(\frac{2\pi t}{T_s} \right) - 1 \right) \right] & t < T_s \\ \omega_s \left(t - \frac{T_s}{2} \right) & t \geq T_s \end{cases} \quad (4.1)$$

The exact solution for the steady state extension of a spinning rod with angular velocity ω_s can be easily shown to be

$$x(1, t) \cos \psi + y(1, t) \sin \psi = L \left[\frac{\tan aL}{aL} - 1 \right]; \text{ where } a = \sqrt{\frac{\rho A}{EA}} \omega_s \quad (4.2)$$

In the past, two test cases have been performed to show the effect of centrifugal stiffening. We list the parameters for each case in Table 4.3. Case 1 was studied by [Wu and Haug, 1988] and [Dufva *et al.*, 2005]. Case 2 was studied by [Wallrapp and Schwertassek, 1991] and [Simo and Vu-Quoc, 1986]. Both cases are computed using the global coordinate model. The results obtained are compared with those published results as shown in Table 4.4. The comparisons show excellent agreement.

Table 4.3 Simulation parameters and values for the spinning rod

Simulation Parameters	Case 1	Case 2
Length of link L	8 m	10m
Density ρ	2767.77 kg/m ³	3000 kg/m ³
Moment of inertia I	8.214x10 ⁻⁹ m ⁴	1.997x10 ⁻⁷ m ⁴
Cross-sectional area A	7.299x10 ⁻⁵ m ²	4x10 ⁻⁴ m ²
Young's Modulus E	6.895x10 ¹⁰ Pa	7x10 ¹⁰ Pa
(T_s, ω_s)	(15 sec, 2 rad/sec)	(15 sec, 6 rad/sec)
Time step size Δt	0.005 sec	0.005 sec
Initial tip location $[x_1(1), y_1(1)]$	[8, 0] m	[10, 0] m

Table 4.4 Comparisons of global coordinate model and other models

Steady-state extension of rod	Case 1	Case 2
Published results	2.7386x10 ⁻⁵ m	5.14x10 ⁻⁴ m
Results by global coordinate model	2.7385x10 ⁻⁵ m	5.144x10 ⁻⁴ m

Figure 4.11 and 4.12 also shows the tip displacements in the local x and y direction using the following formulae.

$$\begin{bmatrix} x_{tip} \\ y_{tip} \end{bmatrix} = \begin{bmatrix} \cos[\psi(0, t)] & \sin[\psi(0, t)] \\ -\sin[\psi(0, t)] & \cos[\psi(0, t)] \end{bmatrix} \begin{bmatrix} x(1, t) \\ y(1, t) \end{bmatrix} - \begin{bmatrix} L \\ 0 \end{bmatrix} \quad (4.3)$$

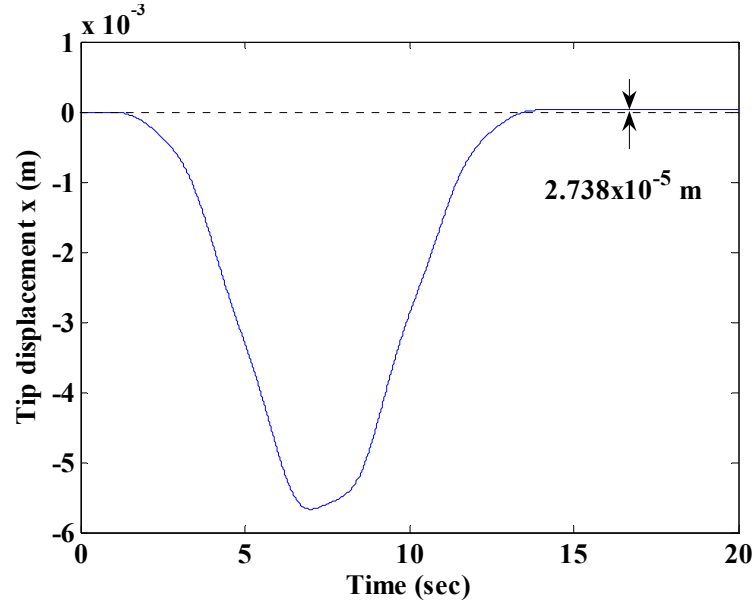


Figure 4.11 The steady-state extension of the rod, 2.738x10⁻⁵ m

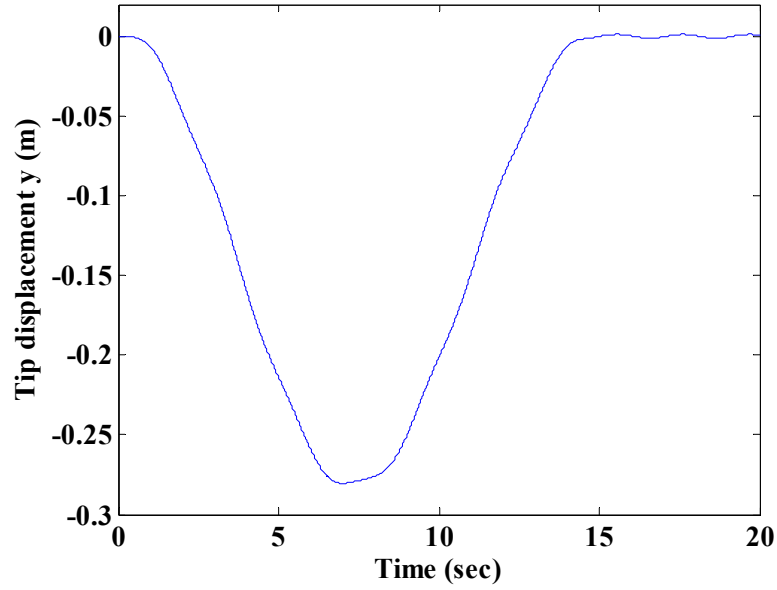


Figure 4.12 The displacement of the tip in the y direction

Example II.1 Slider-crank mechanism

We consider here a slider crank mechanism as shown in Fig. 4.13. An input torque M drives the mechanism at the base of link 1 (crankshaft) that connects link 2 (connecting rod) by joint C. Link 2 is tied to another massless slider block through a revolute joint. The slider block can only move in the x direction (prismatic joint) and it is assumed the surface is frictionless.

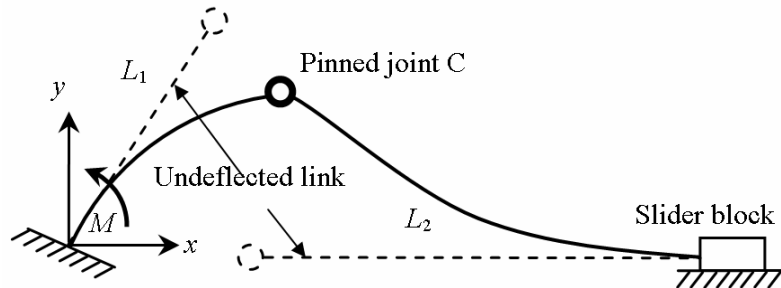


Figure 4.13 Compliant slider crank mechanism

The input torque at link 1 for different time is given as follows and simulation parameters given in Table 4.5.

$$M(t) = \begin{cases} 0.02t & 0 \leq t < 0.5 \\ 0.01 & 0.5 \leq t < 0.7 \\ 0.01 - 0.02(t - 0.7) & 0.7 \leq t < 1.2 \\ 0 & 1.2 \leq t \end{cases} \quad (4.4)$$

Table 4.5 Simulation parameters and values for the compliant slider crank

Simulation Parameters	Values
Length of link (L_1, L_2)	(0.152, 0.304) m
Density (ρ_1, ρ_2)	(2770, 2770) kg/m ³
Moment of inertia (I_1, I_2)	(4.909x10 ⁻¹⁰ , 4.909x10 ⁻¹⁰) m ⁴
Cross-sectional area (A_1, A_2)	(7.854x10 ⁻⁵ , 7.854x10 ⁻⁵) m ²
Young's Modulus (E_1, E_2)	(1x10 ⁹ , 5x10 ⁷) Pa
Time step size Δt	0.005 sec
Initial tip location	$[x_1(1), y_1(1)] = [0.152, 0]$ m $[x_2(1), y_2(1)] = [0.456, 0]$ m

The displacement of the slider block is shown in Figure 4.14 and the midpoint deformation of connecting rod is shown in Figure 4.15. We also compare the presented dynamic model with the floating frame formulation and absolute nodal coordinate formulation in these figures. These results show very good agreement.

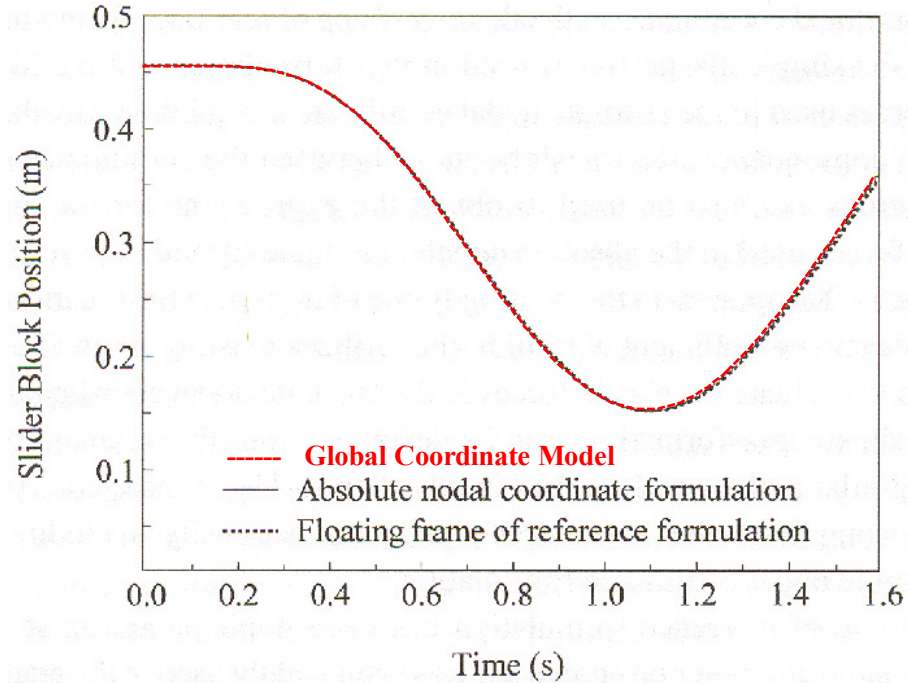


Figure 4.14 Horizontal position of the slider block

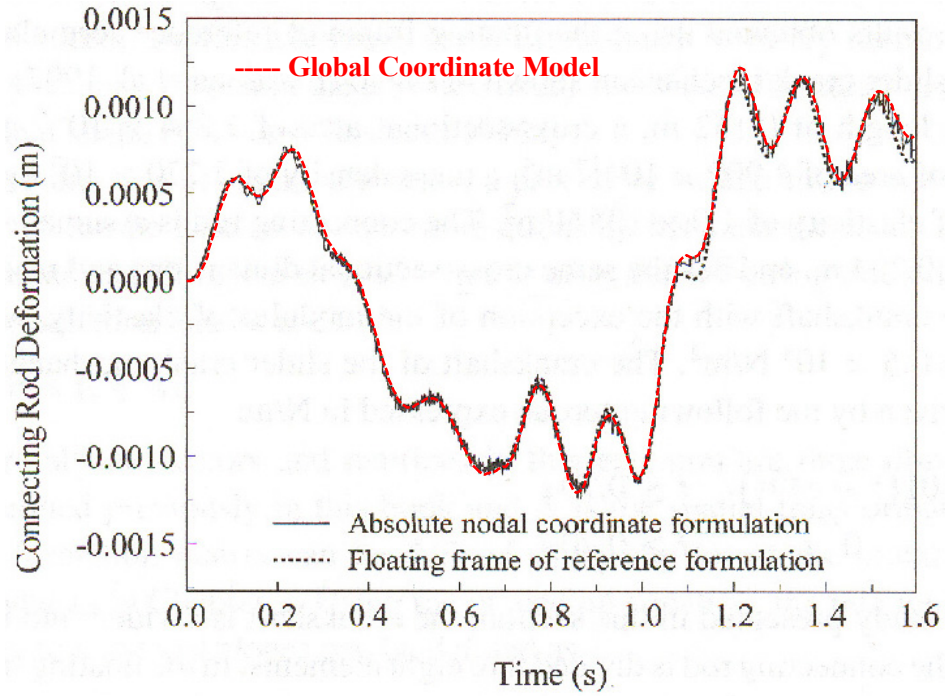


Figure 4.15 Deformation of link 2

Example II.2 Four bar mechanism

In order to explore the ability of global coordinate model for a closed chain mechanism, we study here the dynamics of a compliant four-bar mechanism whose initial configuration is shown in Figure 4.16. The coupler (link 2) is made more compliant than the other two links in order to examine the capability of large deformation. Detailed parameters of the mechanism are listed in Table 4.6.

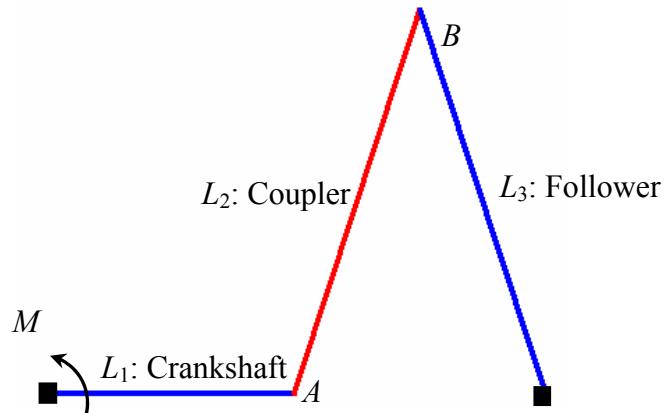


Figure 4.16 Initial four-bar mechanism configuration

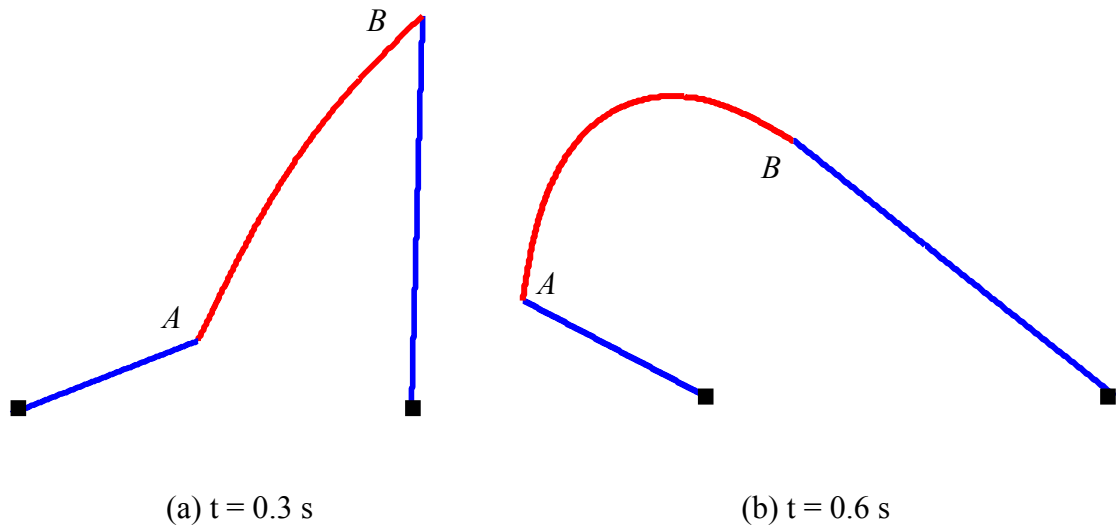
Table 4.6 Parameters of the four-bar mechanism

Parameters	Values
Length of link (L_1, L_2, L_3)	(0.5, 1, 1) m
Density (ρ_1, ρ_2, ρ_3)	(7847, 7847, 7847) kg/m ³
Moment of inertia (I_1, I_2, I_3)	(1.257×10^{-7} , 1.257×10^{-7} , 1.257×10^{-7}) m ⁴
Cross-sectional area (A_1, A_2, A_3)	(1.257×10^{-3} , 1.257×10^{-3} , 1.257×10^{-3}) m ²
Young's Modulus (E_1, E_2, E_3)	(2.1×10^{11} , 2.1×10^8 , 2.1×10^{11}) Pa
Initial tip location	$[x_1(0), y_1(0)] = [0, 0]$ m $[x_3(1), y_3(1)] = [1, 0]$ m

The mechanism is initially at rest and the crankshaft is given a moment input from $0 \leq t \leq 0.6$ as shown in Equation (4.5).

$$M(t) = \begin{cases} 500t & 0 \leq t < 0.2 \\ 100 & 0.2 \leq t < 0.4 \\ 100 - 500(t - 0.4) & 0.4 \leq t < 0.6 \\ 0 & 0.6 \leq t \end{cases} \quad (4.5)$$

Figure 4.17 shows the deformation of the mechanism at four specific time spots. Obviously the coupler undergoes more deformation than the crankshaft and follower. Note that from Figure 4.17(a) to 4.17(c) the crankshaft rotates counter clockwise while from Figure 4.17(c) to 4.17(d) it rotates clockwise.



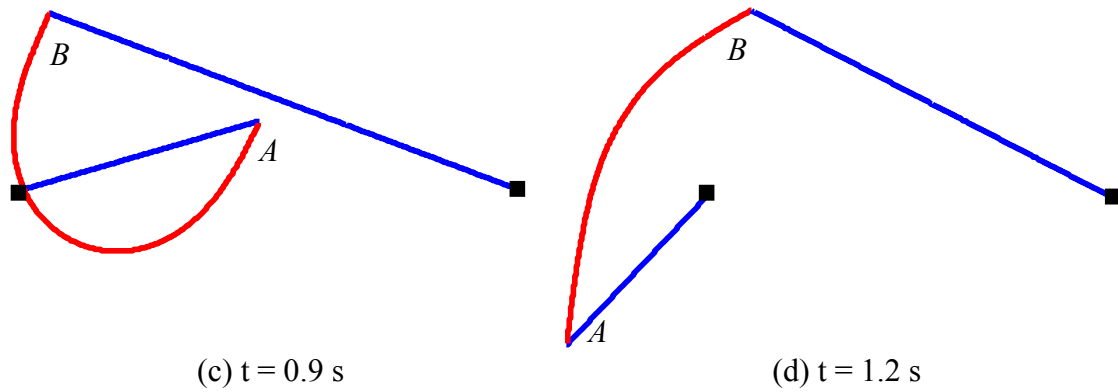


Figure 4.17 Large deformations of the four-bar mechanism

The advantage of the global coordinate model is that it is derived from Hamilton's principle. Hence it allows us to easily verify the results by energy balance check. Figure 4.18 shows the calculated energy which must equal to the applied work apparently. It is obvious that the total kinetic energy is converted to potential energy at $t=0.95\text{s}$. After the potential energy reaches its maximum (and the kinetic energy reaches its minimum), the energy transfers back again to the kinetic component.

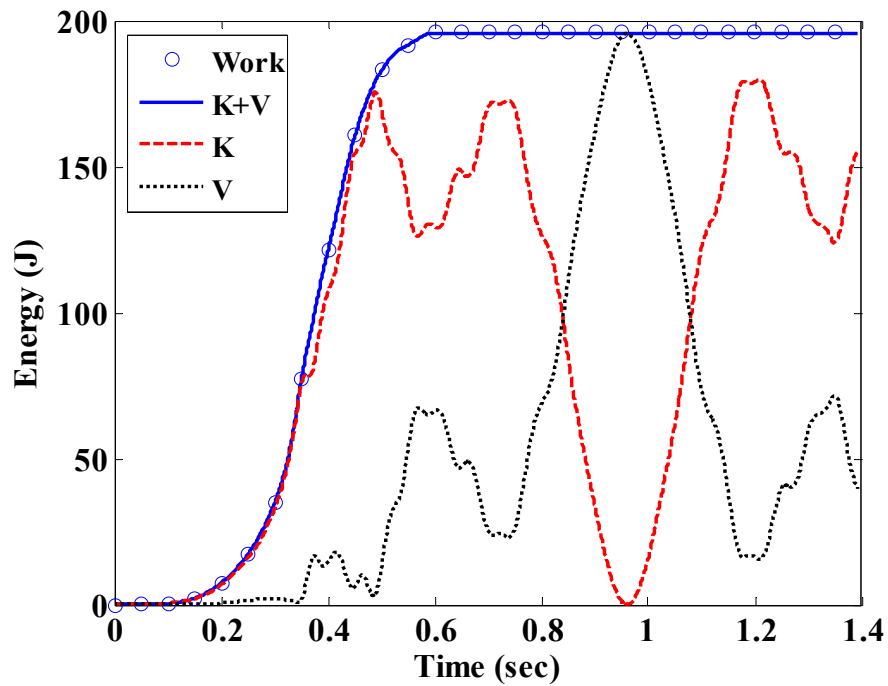


Figure 4.18 Energy balance of the four-bar mechanism (GCM with $\Delta t = 0.001$)

Figure 4.19 also shows the internal forces at the two joints that can be automatically obtained by the global coordinate model. Both four internal forces (h_1, v_1, h_2, v_2) have peak values around $t=0.35$ seconds.

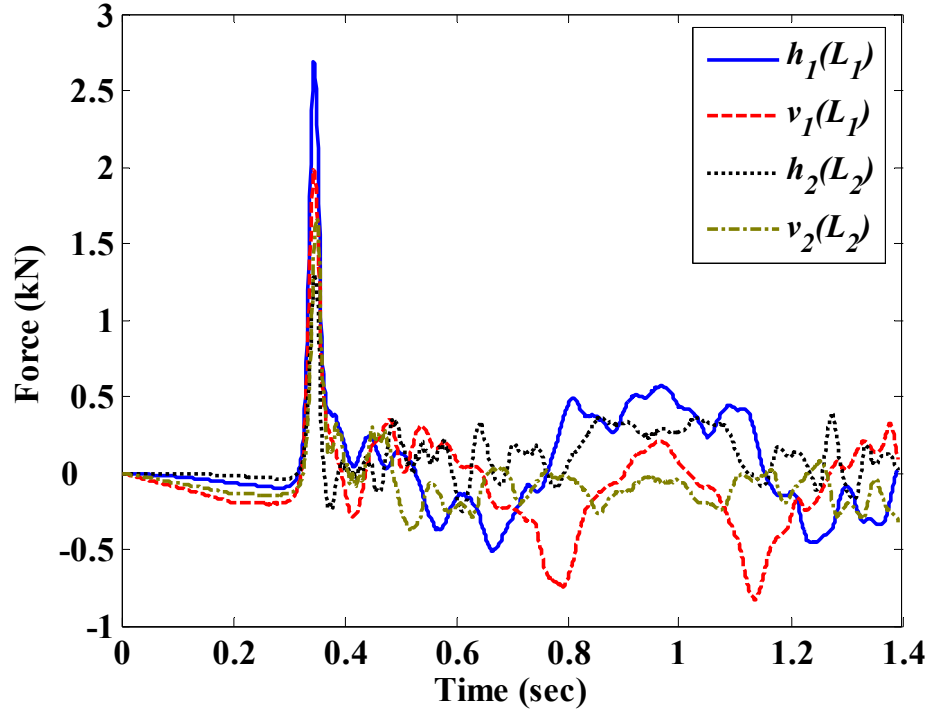


Figure 4.19 Internal forces at the joints

Based on the examples given above, the following observations can be made by comparing the global coordinate model with other existing method for analyzing flexible multibody systems.

1. Compared with the floating frame formulation, the links in the global coordinate model are all referenced in the global coordinate. The GCM has no geometric assumption, and thus, can be applied for links with large deflection.
2. As mentioned in Chapter 1, the corotational procedure relies on small deflection (less than 30°) between successive time steps. It requires reducing step size in order to get

more accurate results. However, the error will still accumulate even for small deflections.

3. Compared with other displacement-based models, the internal forces at the joints can be automatically obtained by using the global coordinate model.

4.3 Conclusions

Five examples are discussed in this chapter to verify the global coordinate model. An illustrative example of a free-vibrating steel rod has been given to show the application of the model. The simulation result of the vibrating rod has matched well with the experiment data. Finally we extend the dynamic model for predicting the motion of one compliant link to analyze compliant mechanisms. An illustration example has been given to show the accuracy of the proposed model over general finite element software (ANSYS).

CHAPTER 5

DESIGN AND ANALYSIS USING GLOBAL COORDINATE MODEL

5.1 Introduction

We presented the global coordinate model with systematic formulation in Chapter 3 to predict the dynamic response of serial compliant mechanisms. In this chapter, we explore its static forward and inverse model for analyzing compliant mechanisms (both serial and parallel). The forward model seeks for the deformed configuration given its initial configuration and applied forces. It is useful for analyzing mechanisms whose initial shape is known. The inverse model, on the other hand, seeks for the initial configuration given its deformed configuration and internal forces. It is useful for analyzing mechanisms whose desired shapes are known. Of particular interest here is to develop a computer program to facilitate design analysis of compliant mechanisms. As will be shown through an illustrative application, the forward/inverse models can also serve as a basis for optimizing compliant links with initial curvatures.

Specifically, this chapter provides the following:

1. *A static forward and inverse model.* The model will be obtained by neglecting time dependent terms in Equation (3.10). Unlike traditional models that attach a frame to

each link, this model is derived using the global coordinate which requires no transformation matrices between links.

2. *A systematic formulation.* This formulation provides a means to analyze both serial and parallel compliant mechanisms. A computer program with GUI will be developed to facilitate design of compliant mechanisms.
3. *Illustrative examples.* Examples will be given to characterize the effect of shear deformation and illustrate the global coordinate model for forward/inverse analyses.
4. *A case study.* This case study has been motivated by the need to accommodate a limited range of sizes in live object handling.

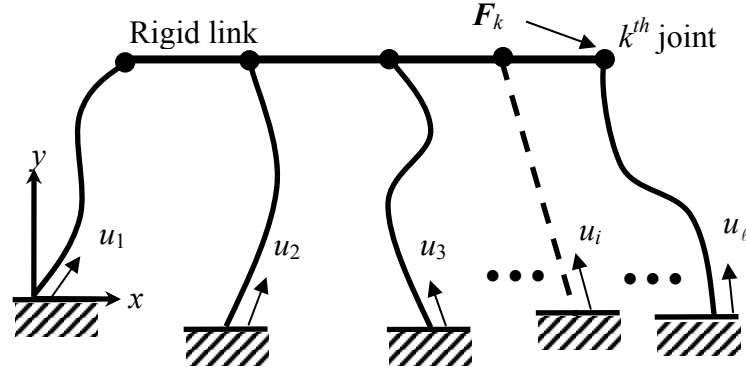
Note that same as Chapter 3, we use generalized multiple shooting method through out this chapter to solve for the global coordinate model.

5.2 Global Coordinate Model for Static Analysis

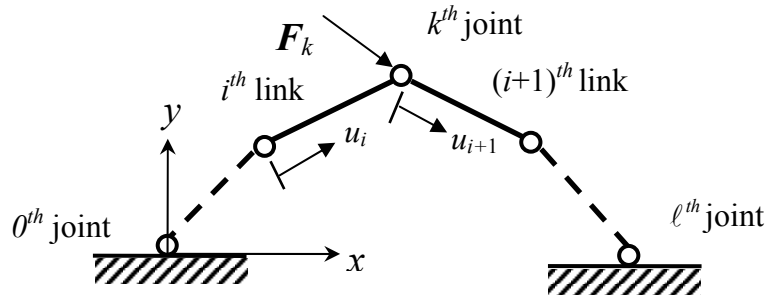
We first derive the static governing equations for a compliant link. Deflections due to flexural and shear deformation are both considered. The constraint formulations for generic compliant mechanisms are then developed. Finally the relations between a forward and inverse problem are addressed.

5.2.1 Governing equations for a link

Consider a typical mechanism consisting of ℓ compliant links shown in Figure 5.1, where $\mathbf{F}_k = (F_{xk}, F_{yk})$ is an external concentrated force acting at the k^{th} joint. Each link is described by a non-dimensional arc length u_i with the arrow indicating the positive direction.



(a) A compliant parallel mechanism



(b) A compliant serial mechanism

Figure 5.1 Generic compliant mechanisms

Without loss of generality, we consider here two joint configurations, which can be either clamped or revolute.

- (i) A floating joint connects w links as shown in Figure 5.2(a). Index j is used to number the links. An external concentrated force (F_{xk}, F_{yk}) may apply at the joint.
- (ii) A fixed joint connects a link to ground (rigid structure) as shown in Figure 5.2(b). If more than one link are connected, they are treated as individual fixed joints.

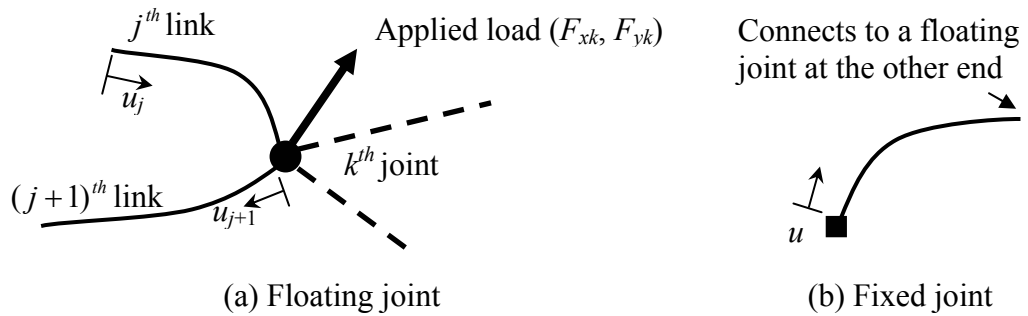


Figure 5.2 A joint that connects multiple links

The equations that govern the static deformation of the link can be reduced from Equation (3.10) as follows:

$$\frac{E_i I_i}{L_i^2} (\psi_i'' - \eta_i'') + v_i \cos(\psi_i + \gamma_i) - h_i \sin(\psi_i + \gamma_i) = 0 \quad (5.1a)$$

$$h_i' = 0; \quad v_i' = 0 \quad (5.1b,c)$$

$$[v_i \cos(\psi_i + \gamma_i) - h_i \sin(\psi_i + \gamma_i)] - \kappa_i G_i A_i \gamma_i = 0 \quad (5.1d)$$

Compared with many other displacement-based models that often need a post computation in order to obtain internal forces (h_i, v_i) , Equation (5.1) can directly solve for those forces. They also serve as an essential basis for the forward/inverse models that will be introduced later.

Depending on the type of problems, Equations (5.1a~d) must be solved simultaneously with

$$\text{Forward:} \quad x_i' - L_i \cos(\psi_i + \gamma_i) = 0; \quad y_i' - L_i \sin(\psi_i + \gamma_i) = 0 \quad (5.1e,f)$$

$$\text{Inverse:} \quad x_i' - L_i \cos \eta_i = 0; \quad y_i' - L_i \sin \eta_i = 0 \quad (5.1g,h)$$

The coordinate variables (x_i, y_i) indicate the deformed and initial shapes for the forward and inverse problems respectively. Besides its static feature, we list the major differences of Equation (5.1) from Equation (3.10) as follows:

- (1) We add the shape function $\eta_i(u_i)$ in Equation (5.1a) to represent the initial configuration of the i^{th} link. This is similar to Frisch-Fay's [1962] beam model presented in Subsection 2.3.2. However, in Frisch-Fay's model, the external force F and its direction α are measured in the local frame attached to each link. The global coordinate model, on the other hand, requires no local frame since the external force is decomposed into the global x and y direction (h and v respectively). Hence, only a

single coordinate, which is the inertia frame, is necessary to model all the links; thus, the GCM simplifies the formulation, and eliminates computation of coordinate transformation.

- (2) Note that the mass of the links does not affect the deformation hence the internal forces h and v become constant values within each link.
- (3) We had the axial elongation variable e in Equation (3.10) in order to capture the centrifugal stiffening effect (see Example I.3 in Section 4.2). However, for static analysis this is not a problem and hence we ignore the axial deformation.

5.2.2 Constraint (boundary) equations

Equation (5.1) that governs each link is subjected to constraint equations at both ends ($u=0$ or 1), which may be a floating and/or fixed joints shown in Figure 5.2. For convenience, we introduce \bar{u} and δ to denote the value of u at the joints so that

$$\delta = \begin{cases} -1 & \text{if } \bar{u} = 0 \\ +1 & \text{if } \bar{u} = 1 \end{cases}$$

For clarity, the constraint equations are divided into two classes, force/displacement and angle/moment, as follows:

1 Force/displacement constraint equations

Force/displacement constraints depend on the mobility of joints (floating or fixed). For a floating joint, the forces must balance regardless of its type (clamped or revolute). With external forces F_{xk} and F_{yk} , the following equations must be satisfied:

$$\sum_{j=1}^w \delta h_j - F_{xk} = 0; \quad \sum_{j=1}^w \delta v_j - F_{yk} = 0. \quad (5.2a,b)$$

The links are also connected rigidly at the floating joint and must satisfy the following $w - 1$ constraint equations to prevent separation.

$$\begin{aligned} x_j(\bar{u}_j) - x_{j+1}(\bar{u}_{j+1}) &= 0 \text{ for } j = 1 \sim w - 1 \\ y_j(\bar{u}_j) - y_{j+1}(\bar{u}_{j+1}) &= 0 \text{ for } j = 1 \sim w - 1 \end{aligned} \quad (5.2c,d)$$

In addition, a floating joint may have absolute displacement load (D_{xk}, D_{yk}) as follows:

$$x_1(\bar{u}_1) = D_{xk}; \quad y_1(\bar{u}_1) = D_{yk} \quad (5.2e,f)$$

When an arbitrary D_{xk} or D_{yk} is applied to a joint, the corresponding forces (F_{xk} and F_{yk}) are unknown since force and displacement cannot be applied simultaneously at a joint.

For a fixed joint, the two constraint equations are

$$x(\bar{u}) = \text{constant} \text{ and } y(\bar{u}) = \text{constant} \quad (5.2g,h)$$

where the constants are determined by mechanism configurations. The internal forces for the link connecting to a fixed joint must be determined from the other end, which connects to a floating joint.

2 Moment/angle constraint equations

Moment/angle constraints given below depend on joints types (clamped or revolute as well as floating or fixed joints):

Floating joint - w constraint equations

At a *clamped joint*, the clamped angle between every two links must remain unchanged after they are deflected and the moment summation of every link must balance at the joint:

$$\eta_j(\bar{u}_j) - \eta_{j+1}(\bar{u}_{j+1}) = \psi_j(\bar{u}_j) - \psi_{j+1}(\bar{u}_{j+1}) \text{ for } j = 1 \sim w - 1 \quad (5.3a)$$

$$\sum_{j=1}^w \delta \frac{E_j I_j}{L_j} [\psi'_j(\bar{u}_j) - \eta'_j(\bar{u}_j)] = 0 \quad (5.3b)$$

A *revolute joint* cannot resist moment hence the change of slope must be zero for all the w links.

$$[\psi'_j(\bar{u}_j) - \eta'_j(\bar{u}_j)] = 0 \text{ for } j = 1 \sim w \quad (5.3c)$$

Fixed joint - one constraint equation

Equation (5.3d) is the angle constraint for a clamped joint and Equation (5.3e) is the moment equation for a revolute joint.

$$\eta(\bar{u}) = \psi(\bar{u}) ; [\psi'(\bar{u}) - \eta'(\bar{u})] = 0 \quad (5.3d,e)$$

5.2.3 Forward and inverse as a dual problem

The system (Figures 5.1 and 5.2) represented by Equations (5.1a~5.1h) and constraints (5.2) and (5.3) can be formulated as a forward or an inverse problem, which are a complementary pair as illustrated in Figure 5.3.

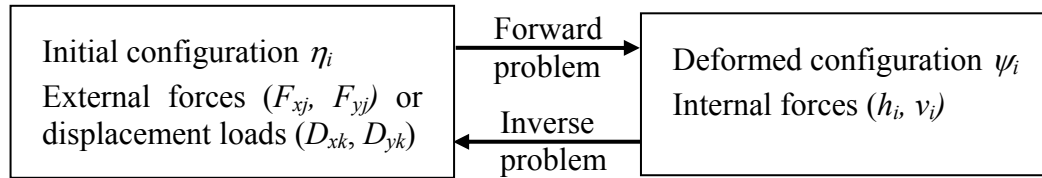


Figure 5.3 The forward and inverse problems

The forward analysis solves for the deformed shape characterized by the link curvature $\psi_i + \eta_i$ and the corresponding internal forces (h_i, v_i) given the initial shape η_i and external forces. On the other hand, the inverse analysis solves for the initial shape η_i and external forces given the deformed shape and internal forces. Unlike the forward model that focuses on analysis, the inverse model is for synthesis (or design). It is not always

known how much an external force a mechanism can resist before it yields. However, the yield strength of common material is generally available. By specifying internal forces that are below the material's limit, the inverse analysis will give us the appropriate external forces.

5.3 Forward and Inverse Analyses

Following the procedures of GSM, we solve for the forward and inverse problems posted in Section 5.2. We consider the forward and inverse problems separately since they have different state-space forms.

5.3.1 Forward and inverse models in state-space forms

The forward problem is defined as follows: *Given initial mechanism configuration and external loads, solve for the deformed configuration and internal forces of all links.* For this, Equations (5.1a)~(5.1f) are recast in a state-space form:

$$\mathbf{M}_i \mathbf{q}'_i = \begin{bmatrix} \psi' \\ \frac{L_i^2}{E_i I_i} [h_i \sin(\psi_i + \gamma_i) - v_i \cos(\psi_i + \gamma_i)] + \eta'' \\ L_i \cos(\psi_i + \gamma_i) \\ L_i \sin(\psi_i + \gamma_i) \\ [v_i \cos(\psi_i + \gamma_i) - h_i \sin(\psi_i + \gamma_i)] - \kappa_i G_i A_i \gamma_i \end{bmatrix} \quad (5.4a)$$

where $\mathbf{q}_i = [\psi \ \psi' \ x \ y \ \gamma]$ are the state variables. Since the last component in Equation (5.4a) is an algebraic equation that does not include γ' , the matrix \mathbf{M}_i is singular. Equation (5.4a) becomes a set of DAE. The MATLAB programs ode15s and ode23t [Shampine, 1997] can be used to integrate DAE as an ODE.

We define the inverse problem as follows: *Given a deformed configuration and some of its internal forces, solve for the initial configuration and external forces.* The

internal forces are the design parameters to be specified (with selection of materials). As in the forward analysis, Equations (5.1a)~(5.1d) and (5.1g,h) are recast for the inverse problem as follows:

$$\mathbf{M}_i \mathbf{q}'_i = \begin{bmatrix} \eta' \\ L_i^2/E_i I_i [v_i \cos(\psi_i + \gamma_i) - h_i \sin(\psi_i + \gamma_i)] + \psi'' \\ L_i \cos \eta_i \\ L_i \sin \eta_i \\ [v_i \cos(\psi_i + \gamma_i) - h_i \sin(\psi_i + \gamma_i)] - \kappa_i G_i A_i \gamma_i \end{bmatrix} \quad (5.4b)$$

where $\mathbf{q}_i = [\eta \quad \eta' \quad x \quad y \quad \gamma]$ are the state variables. Opposite of Equation (5.4a), the unknown and known shape functions of the inverse problem are η and ψ respectively.

5.3.2 Number of unknowns and constraint equations

The unknowns generally include initial values of Equation (5.4) with force loads (F_{xk}, F_{yk}) and/or displacement loads (D_{xk}, D_{yk}). As an example, we consider force loads for the mechanism shown in Figure 5.1. The number of constraint equations and unknowns are given in Tables 5.1 and 5.2.

Table 5.1 Number of constraint equations for a joint

Type of constraints	Floating joint	Fixed joint
Force/displacement	$2w$	2
Moment/angle	w	1
Total	$3w$	3

Table 5.2 Unknowns for the forward and inverse problems

Type of unknowns	Forward problem	Inverse problem
Initial values (μ_i)	$\psi_i(0), \psi'_i(0), x_i(0), y_i(0)$	$\eta_i(0), \eta'_i(0), x_i(0), y_i(0)$
Parameters (ξ_i)	h_i, v_i	h_i, v_i, F_{xi}, F_{yi}
Number of unknowns	6ℓ	6ℓ

The number of constraint equations is independent of problem types, i.e., a floating joint connecting w links will have $3w$ constraint equations while a fixed joint will have three. For a forward problem where external forces are given, there are six unknown for every link and hence a mechanism with ℓ links will have 6ℓ unknowns. In order to apply GMSM, we provide the proof that the number of unknowns is always equal to that of the constraint equations for a forward problem.

Proof:

Consider a mechanism consisting of ℓ links. The total number of connections is equal to 2ℓ as a link has two connections. For n_i floating joints connecting i links and m fixed joints, the sum of these joints must equal to the number of connections, or

$$2\ell = \sum_{i=2}^{\ell} in_i + m \quad (5.5)$$

Multiplying the above equation by three on both sides we have

$$6\ell = \sum_{i=2}^{\ell} 3in_i + 3m \quad (5.6)$$

where the 1st and 2nd terms on the right hand side represent the number of constraint equations from floating joints and fixed joints respectively. The sum of them equals to 6ℓ (number of unknowns) on left hand side. We then finish the proof. The forward problem is always solvable.

For the inverse problem where some of the internal forces are given, the number of unknowns must also equal to 6ℓ . In order to be solvable, the number of given internal forces must be equal to the number of unknown external forces. For the case of one external force, we specify the internal force of the link that undergoes most critical loads. Note that the internal force and the applied force don't have to act on the same joint. For

cases of multiple external forces, care must be taken so that the specified internal forces are not over-constrained.

5.4 Illustrative Examples and Applications

We demonstrate GCM and its forward/inverse models with three examples. The 1st example illustrates the effect of shear deformation on the link deflection. The 2nd and 3rd examples illustrate the forward and inverse analyses respectively.

Example 1: Effect of shear deformation on link deflection

As shown in Equations (5.1d~f), the link deflection is caused by both bending and shear. Although shear angles are small within each infinitesimal element, they accumulate along the axial direction of the link. The effect of shear deformation at the tip can be observed by comparing the computation with/without shear deformation, which cannot be ignored especially for highly compliant members or precision flexure mechanisms.

We investigate the effect of shear deformation by applying a vertical (+y) force on a compliant link originally pointing to +x. We denote $\delta + \delta_s$ and δ as the tip deflections in the +y with and without considering shear deformations. We use $\kappa=5/6$ as the shear correction factor for rectangular cross-sections. Other shear correction factors can be found in [Kaneko, 1975].

It can be shown from Equation (5.1d) that the shear angle is inverse proportional to shear modulus G , and from Equations (5.1a) and (5.1d) that the shear angle is proportional to the square of the link height h . We define the following two ratios so that the effect of these two factors on the shear deformation can be studied on a non-dimensional basis:

(a) Material property ratio (E/G): This ratio is related to Poisson's ratio as $E/G=2(1+\nu)$.

Typical materials have an E/G between two to three, such as steel ($E/G=2.54$), Delrin ($E/G=2.7$), and rubber ($E/G=3$).

(b) Geometric aspect ratio (h/L): This is the ratio of the height h to the length L of the link.

Figure 5.4 shows the effects of these two ratios on the tip deflection for $\delta=0.2$. Figure 5.5 shows the effect of increasing tip deflection δ to the deflection δ_s caused by shear.

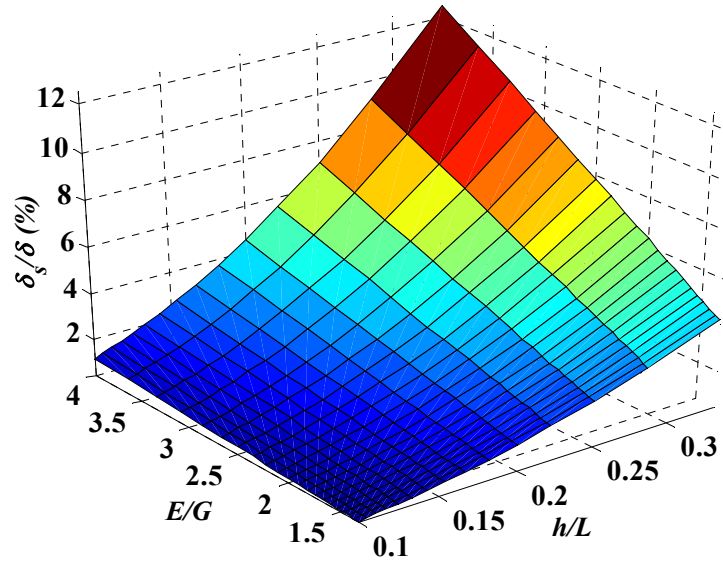


Figure 5.4 Effect of shear on tip deflection with $\delta=0.2$

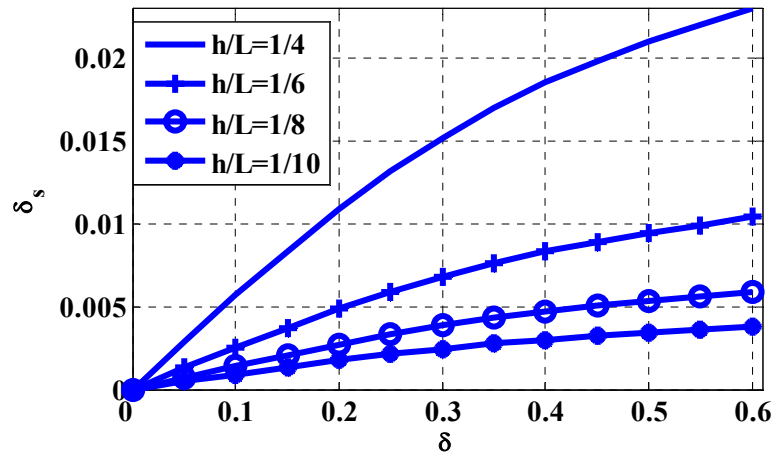


Figure 5.5 Effect of shear for link with large deflection ($E/G = 3$)

Clearly, the deflection δ_s becomes more significant as the two ratios increase; it is especially dominated by the geometric ratio. As expected, δ_s increases as δ increases. Hence the tip deflection due to shear deformation becomes significant for links undergoing large deflections.

Example 2: Forward analysis of a six-bar mechanism

The mechanism shown in Figure 5.6 was originated from Kim and Kota [2002] as a compliant transmission for the secondary micro actuators in disk drives. The 6-bar mechanism is actually a 4-bar mechanism with its mirror image over the vertical link L_3 . Translation of J_4 can be obtained by an input force at J_2 . We solve for the displacement δy for a given force F_{y2} at J_2 . The parameters of the mechanism are that $L_1=L_5=0.5\text{m}$, $L_2=L_4=0.68\text{m}$, and $L_3=0.4\text{m}$. All the links are initially straight ($\eta'_i = 0$) and have the same flexural rigidity $EI=0.3\text{Nm}^2$. The angles between the links are $\beta_1 = \beta_2 = \pi/6$. The arrows in the middle of each link indicate the direction of the arc length u .

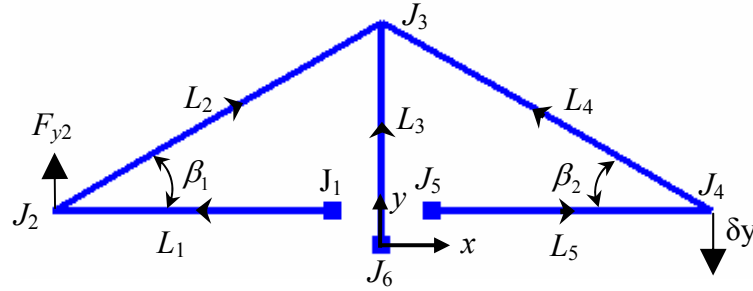


Figure 5.6 A compliant double four-bar mechanism

Since the mechanism consists of $\ell = 5$ links, there are $6 \times 5 = 30$ constraint equations, which are given in Table 5.3. The simulated geometry after deformation and computed F - δy curve are shown in Figs. 5.7 and 5.8 respectively. The results match well with those obtained by ANSYS (commercially available FE software).

Table 5.3 Constraint equations for the double four-bar mechanism

Force constraints	
J ₂ :	$h_1 - h_2 = 0 ; v_1 - v_2 - F_{2y} = 0$
J ₃ :	$h_2 + h_3 + h_4 = 0 ; v_2 + v_3 + v_4 = 0$
J ₄ :	$h_5 - h_4 = 0 ; v_5 - v_4 = 0$
Compatibility constraints	
J ₁ :	$x_1(0) + 0.088 = 0 ; y_1(0) - 0.06 = 0$
J ₂ :	$x_1(1) - x_2(0) = 0 ; y_1(1) - y_2(0) = 0$
J ₃ :	$x_2(1) - x_3(1) = 0 ; y_2(1) - y_3(1) = 0 ; x_3(1) - x_4(1) = 0 ; y_3(1) - y_4(1) = 0$
J ₄ :	$x_5(1) - x_4(0) = 0 ; y_5(1) - y_4(0) = 0$
J ₅ :	$x_3(0) = 0 ; y_3(0) = 0$
J ₆ :	$x_5(0) - 0.088 = 0 ; y_5(0) - 0.06 = 0$
Angle/moment constraints	
J ₁ :	$\psi_1(0) = \pi$
J ₂ :	$\psi_1(1) - \psi_2(0) = \pi - \beta_1 ; \frac{EI_1}{L_1^2} \psi_1'(1) - \frac{EI_2}{L_2^2} \psi_2'(0) = 0$
J ₃ :	$\psi_2(1) - \psi_3(1) = \beta_1 - \pi/2 ; \psi_3(1) - \psi_4(1) = \pi/2 - (\pi - \beta_2) ; \frac{EI_2}{L_2^2} \psi_2'(1) + \frac{EI_3}{L_3^2} \psi_3'(1) + \frac{EI_4}{L_4^2} \psi_4'(1) = 0$
J ₄ :	$\psi_5(1) - \psi_4(0) = -(\pi - \beta_2) ; \frac{EI_5}{L_5^2} \psi_5'(1) - \frac{EI_4}{L_4^2} \psi_4'(0) = 0$
J ₅ :	$\psi_5(0) = 0$
J ₆ :	$\psi_3(0) = \pi/2$

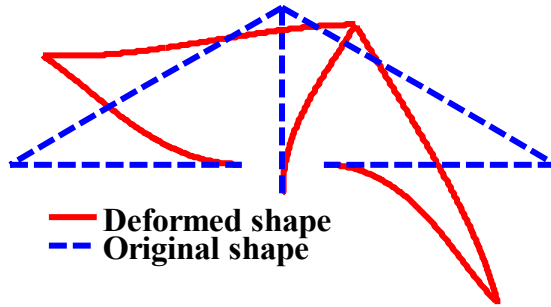


Figure 5.7 Deformed shape

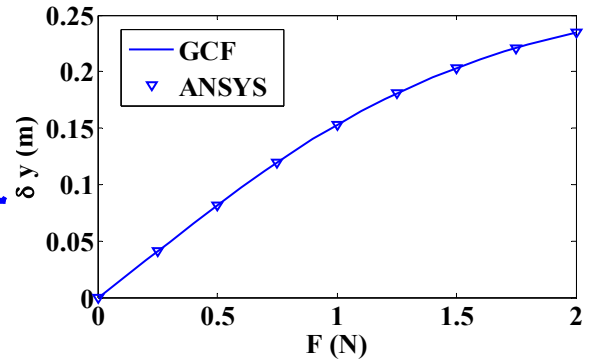


Figure 5.8 Forward $F - \delta y$ curve

Example 3: Inverse analysis of a four-bar mechanism

Consider a compliant 4-bar mechanism. The interest is to find a configuration that, after deflected, has the shape shown in Figure 5.9. It is required that L_2 remains straight under an external force F_{x2} . We also know the critical internal (shear) force h_3 that L_3 can

resist. We now seek for the original shape and F_{x2} . The parameters of the four-bar mechanism are $EI_1 = EI_2 = EI_3 = 0.08\text{Nm}^2$, $L_1 = L_3 = 0.2\text{m}$, and $L_2 = 0.1932\text{m}$.

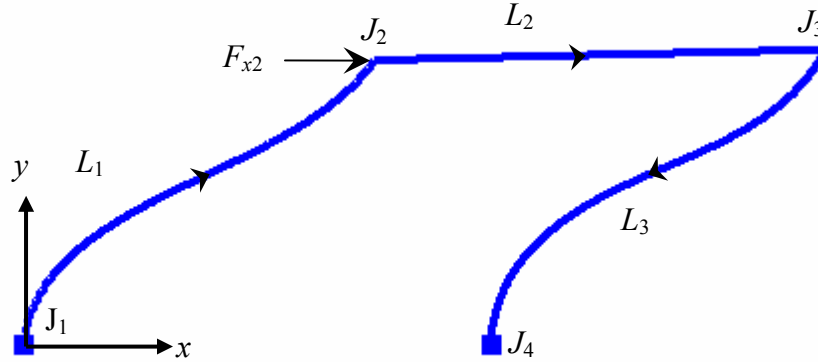


Figure 5.9 Deformed shape of a compliant mechanism

Since the deformed shape is known, the angle function of each link can be approximated as a 4th order polynomial shown in Table 5.4.

Table 5.4 Polynomials that approximate the angle functions

Link 1	$\psi_1(u_1) \approx 4.8763u_1^4 - 11.0858u_1^3 + 11.3610u_1^2 - 5.7463u_1 + 1.5673$
Link 2	$\psi_2(u_2) = 0.0233$
Link 3	$\psi_3(u_3) \approx -0.4298u_3^4 + 0.7269u_3^3 + 3.2937u_3^2 - 3.0966u_3 - 2.0609$

By using the approach stated in Subsection 5.2.2, we formulate the 3x6=18 constraint equations in Table 5.5. The external force F_{x2} is now an unknown and we specify the value of h_3 . The total number of unknowns is 18, which matches the number of constraint equations. Two original shapes are obtained in Figure 5.10 for $h_3=5\text{N}$ and $h_3=-5\text{N}$. Their required forces are 32.48N and -32.33N respectively.

Table 5.5 Constraint equations for the single four-bar mechanism

Force constraints	
J2:	$h_1 - h_2 - F_{x2} = 0; v_1 - v_2 = 0$
J3:	$h_2 - h_3 = 0; v_2 - v_3 = 0$
Compatibility constraints	
J1:	$x_1(0) = 0; y_1(0) = 0$

$$J_2: x_1(1) - x_2(0) = 0; y_1(1) - y_2(0) = 0$$

$$J_3: x_2(1) - x_3(0) = 0; y_2(1) - y_3(0) = 0$$

$$J_4: x_3(1) = 0.2; y_3(1) = 0$$

Angle constraint equations

$$J_1: \eta_1(0) = \psi_1(0)$$

$$J_2: \eta_1(1) - \eta_2(0) = \psi_1(1) - \psi_2(0); \frac{EI_1}{L_1^2} [\psi'_1(1) - \eta'_1(1)] - \frac{EI_2}{L_2^2} [\psi'_2(0) - \eta'_2(0)] = 0$$

$$J_3: \eta_2(1) - \eta_3(0) = \psi_2(1) - \psi_3(0); \frac{EI_2}{L_2^2} [\psi'_2(1) - \eta'_2(1)] - \frac{EI_3}{L_3^2} [\psi'_3(0) - \eta'_3(0)] = 0$$

$$J_4: \eta_3(1) = \psi_3(1)$$

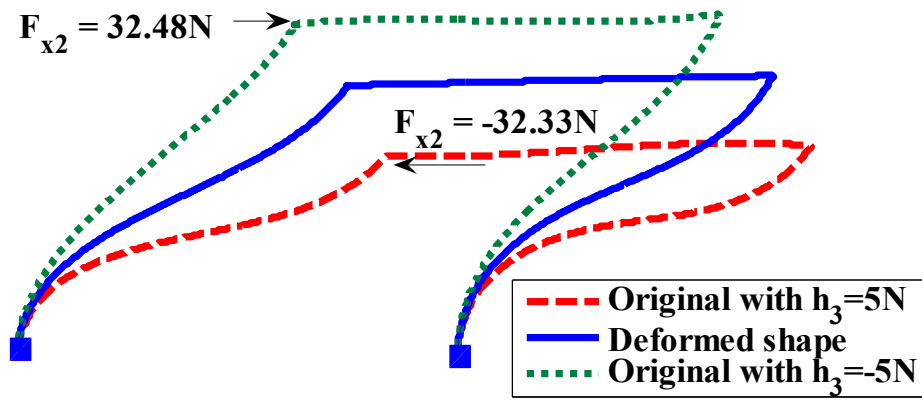


Figure 5.10 Original and deformed shape of the four-bar mechanism

5.5 Software Development

With the systematic procedures stated above, the global coordinate formulation can be written as a graphical user interface (GUI) program to analyze general compliant mechanisms. We develop a program using the forward model with layout shown in Figure 5.11.

The steps of using this program are outlined as follows:

Step 1: **Create joints:** Graphical user input and manual input are both available. Joints will be labeled in order.

Step 2: **Create links:** Create links starting from source joint ($u=0$) to sink joint ($u=1$).

Input flexural rigidity EI for each link. For compliant mechanisms that include

rigid link, increase the flexural rigidity of the rigid link so that it is large enough compared with compliant links. Links will be labeled in order.

Step 3: **Choose fixed joints:** Choose fixed joints from the joints created in Step 1. The fixed joint is limited to one link connection.

Step 4: **Define loads:** Define applied load or displacement at the joint. This is limited to one joint.

Step 5: **Execute:** After setting up the constraint equations, the generalized shooting method will be used to solve this model. Deflected shape will be plotted in red. Internal forces in each link will also be shown.

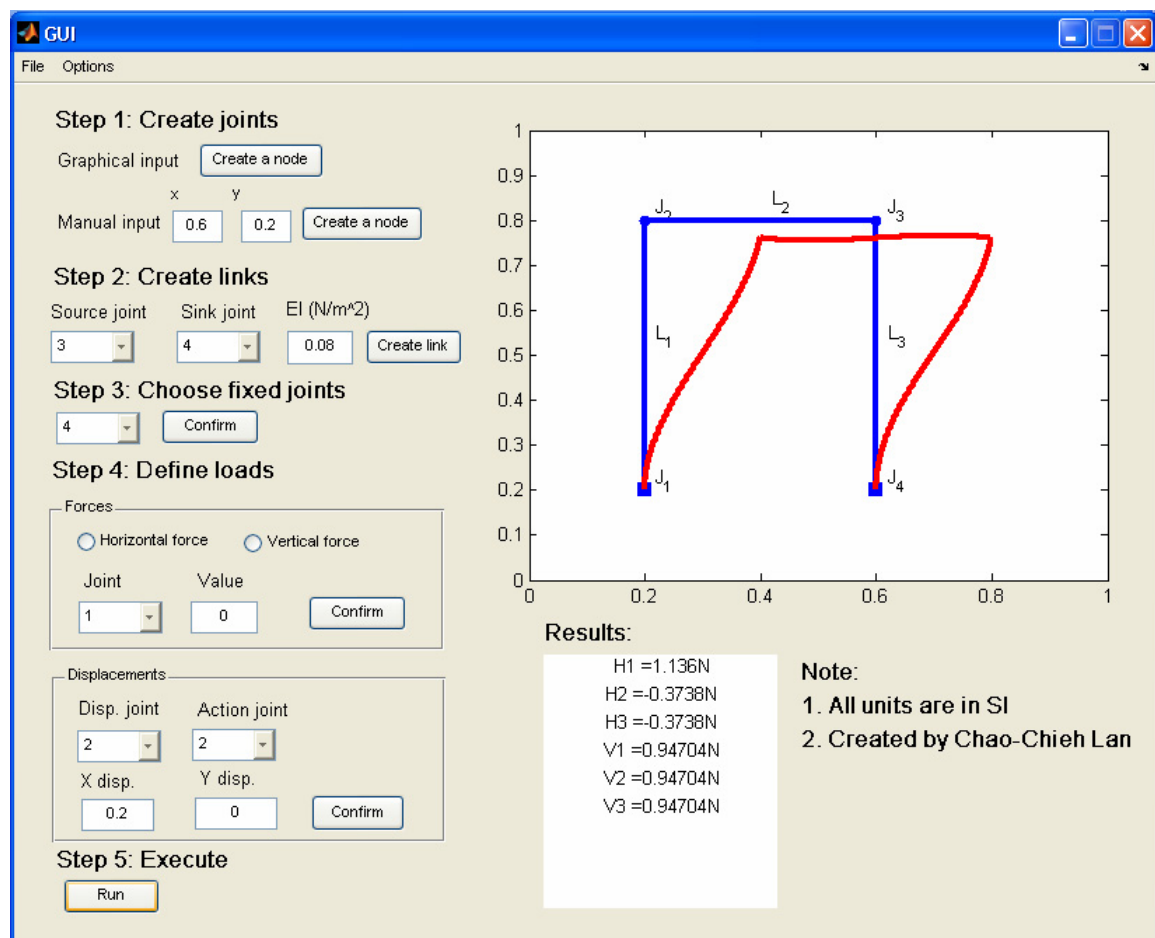


Figure 5.11 Layout of the program

By showing some complicated examples, we demonstrate that the global coordinated model is generic for any number of links with any type of joints. Figure 5.12 shows a compliant gripper mechanism that has often been implemented in micro systems, such as Figure 1.3(b) in [Lee *et al.*, 2003]. Figure 5.13 shows a compliant crimper designed by Saxena and Ananthasuresh [2001].

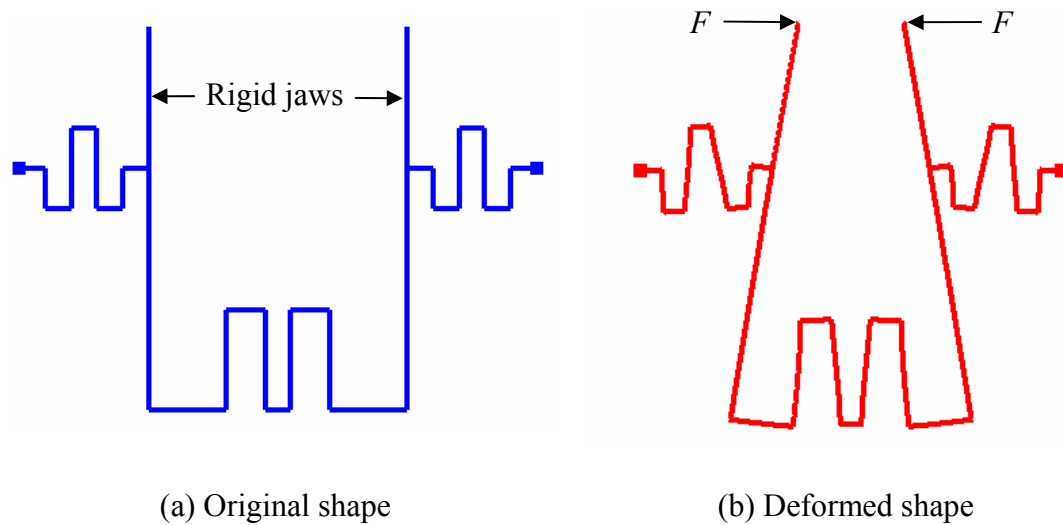


Figure 5.12 Compliant gripper

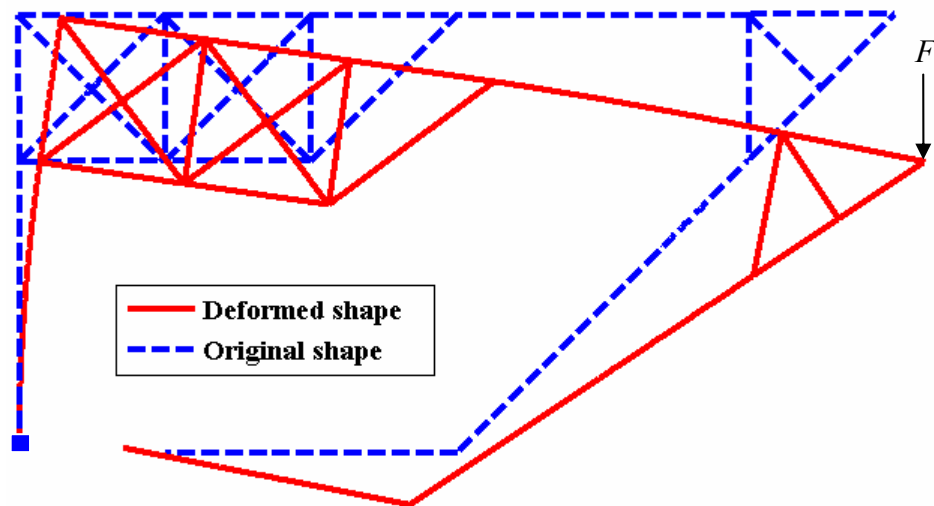


Figure 5.13 Compliant crimper [Saxena and Ananthasuresh, 2001]

5.6 A Case Study: Design and Optimization of a Compliant Grasper

We have shown in the previous sections that the global coordinate model is capable of both forward and inverse analysis. The objective here is to demonstrate that the model is efficient for design and optimization of compliant mechanisms.

The optimization problem of a compliant mechanism can be defined into three hierarchical levels [Howell, 2001]. *Topology optimization* is the highest level that determines the form of the mechanism. It is equivalent to type and number synthesis in rigid-link mechanisms [Uicker *et al.*, 2003]. At the second level, *shape optimization* determines the curvature of each link. It has no rigid-link mechanism counterpart since links must be rigid. At the lowest level, the *size optimization* is considered. It is equivalent to dimensional synthesis in rigid-link mechanisms. Table 5.6 lists the design variables for each level using the nomenclature of the global coordinate model.

Table 5.6 Optimization problems and its corresponding variables

Optimization level	Design variables	Rigid-link mechanism equivalence
Topology	Number of links ℓ and position of joints (x_i, y_i)	Type synthesis and number synthesis
Shape	$\eta(u), \psi(u)$	N/A
Size	I, A, L	Dimensional synthesis

Many research works have been performed to optimize the topology of compliant mechanisms (see [Kirsch, 1989] for review). Most of them assume the shape of link to be initially straight and then perform optimization technique to determine the number of links with their locations. However, the function of the link's initial shape has not been fully explored. The determination of initial shape (or shape optimization) is in general more difficult than size optimization because we need appropriate variables to define the

shape of a compliant mechanism. While this may be a problem for models (such as Euler-Bernoulli's beam model) that based on coordinate variables (x, y) to describe the shape, the global coordinate model can easily express an arbitrary by using initial angle of rotation $\eta(u)$. We illustrate in the following two subsections with an example to show how to optimize the shape of a compliant mechanism using the global coordinate model.

5.6.1 Shape optimization of a compliant link

The well known shortening effect of a large deflected link is shown in Figure 5.14(a). When an initially straight link undergoes a vertical force F , its tip will not only displace in the y direction but also retreat in the x direction. This effect is undesired in applications that require linear displacement of the tip in the y direction while keeping δx unchanged. However, for an initially curved link as shown in Figure 5.14(b), it is possible that δx remains unchanged under a specified force F .

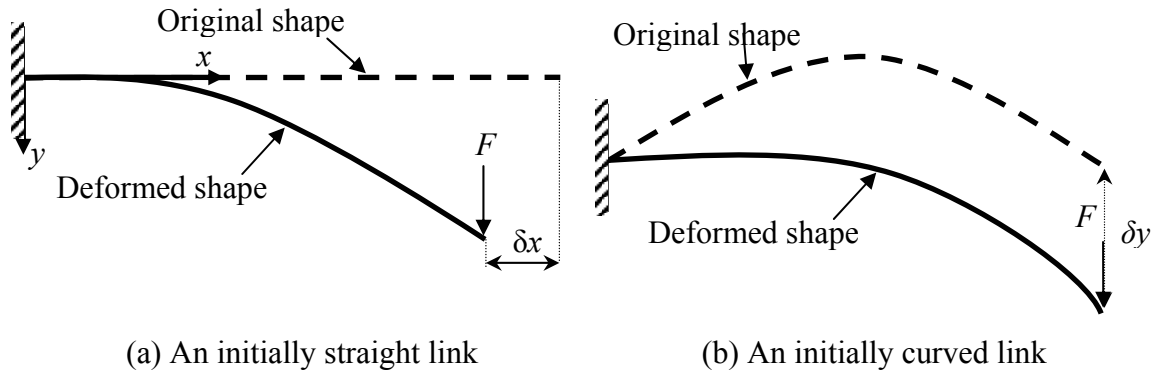


Figure 5.14 Shortening effect of a link

Obviously there are many solutions to the initial shape and specified force in Figure 5.14(b). We post the optimization problems as: *To find the optimal initial shape that requires least force to deflect δy while keeps δx unchanged.* In order to find the optimal shape, we first express the initial curvature of the link in a Fourier sine series as follows:

$$\eta(u) = \sum_{i=1}^{\infty} c_i \sin(2i\pi u) \quad (5.7)$$

where c_i 's are Fourier coefficients. Other series can also be used to express $\eta(u)$. The reasons that we use Fourier sine series are that the slope at $u = 0$ and $u = 1$ are required to be zero for ease of fabrication and Equation (5.7) can express an arbitrary function with zero initial and end slopes. Figure 5.15 shows three different initial shapes using two term (c_1 and c_2) Fourier series that have total link length $L=3.34$ inches. The original base and tip locations are at (0, 0)inch and (2, 0)inch respectively. The forces shown in Figure 5.15 are those required to have $\delta y=0.5$ inch while δx remains unchanged. Obviously the number of inflection points increases as c_2 increases.

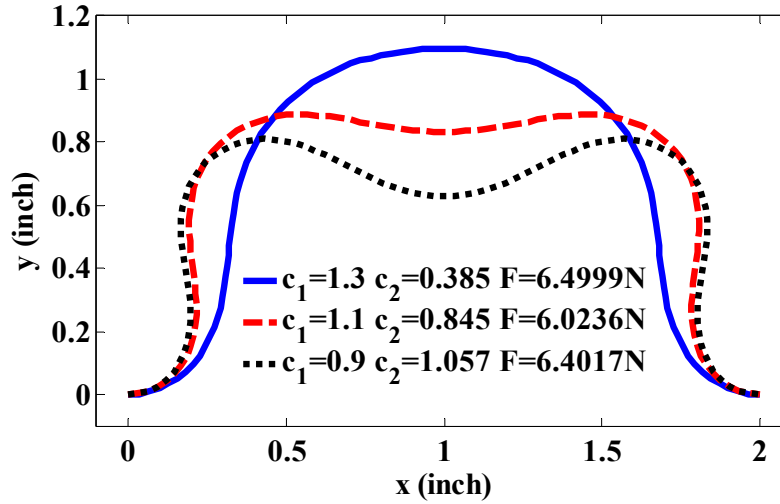


Figure 5.15 Different initial shapes

Since the shape is determined by Fourier coefficients, the vertical force F can be represented as a function of those coefficients. In order to find the minimum F , we express the optimization problem as follows:

$$\min F = f(c_1, c_2, c_3, \dots) \text{ subject to } L < \bar{L} \quad (5.8)$$

where f is the object function that we are trying to minimize and \bar{L} is the given length that the link can not exceed due to design constraints. In this problem we set the object

function as $F = v$ so that the required vertical force is minimized. Other design variables are listed in Table 5.7 with dimensions set according to the fabrication complexity.

Table 5.7 Design variables for compliant grasper

Variable	Value
E	2.62GPa
W x H	0.04572m x 0.001016m
\bar{L}	0.085m (3.34 inches)
$x(1)$	0.0508m (2 inches)
δy	0.0127m (0.5inches)

In order to find the coefficients that would give the optimal solution, we implement the optimization algorithm using MATLAB function *fmincon()*. In each optimization iteration, we use the GSM to obtain the F - δy relations. The optimal shape with respect to one, two, and three terms Fourier series are shown in Figure 5.16. Table 5.8 also shows the optimal coefficients and their corresponding required forces. Smaller F can be obtained by increasing the number of terms. Due to fabrication complexity (machine tool geometry and assembly difficulties, etc), the one term approximation is chosen.

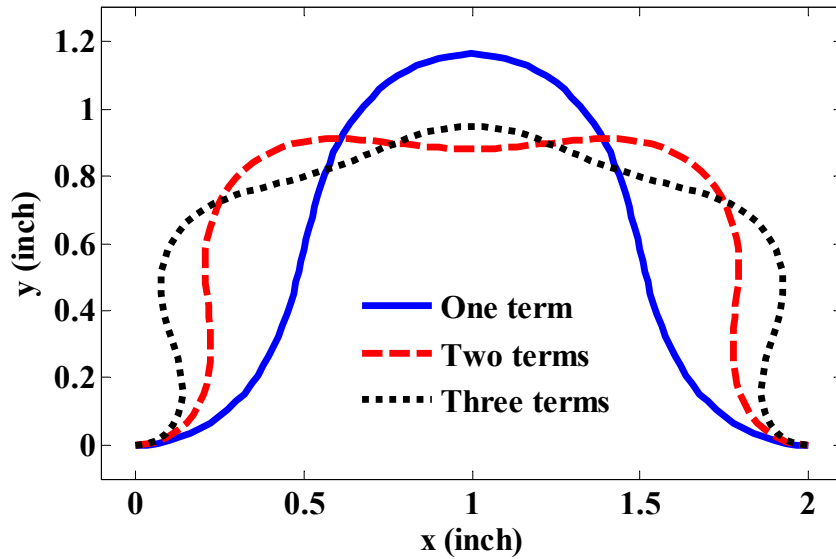


Figure 5.16 Optimal grasper shapes

Table 5.8 Optimal coefficients and required forces

Number of Terms	Function	F (N)
1	$\eta(u) \approx 1.3426 \sin(2\pi u)$	7.6227
2	$\eta(u) \approx 1.1412 \sin(2\pi u) + 0.7817 \sin(4\pi u)$	6.0119
3	$\eta(u) \approx 1.0628 \sin(2\pi u) + 0.7668 \sin(4\pi u) + 0.5197 \sin(6\pi u)$	5.4298

5.6.2 Compliant grasper and experiment validations

An immediate application of the optimized compliant link presented in Subsection 5.5.1 is the compliant grasper shown in Figure 1.2. The compliant grasper consists of a rigid frame with a pair of compliant links inside shown in Figure 5.17. It is used to support the compliant fingers (for grasping objects) and accommodate objects with a limited variation in sizes in the y direction. The force to deflect the compliant links comes from the contact forces between compliant fingers and objects.

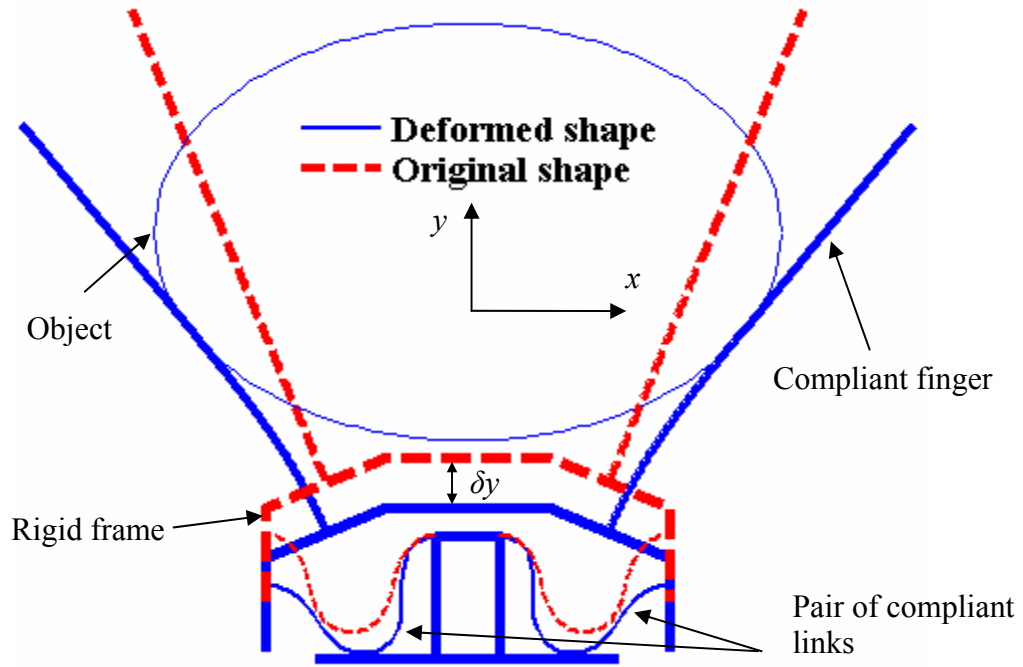


Figure 5.17 Grasping with compliant grasper

We performed an experiment to measure the force-displacement relations of the compliant grasper. As shown in Figure 5.18(a), we use a force tester from

TESTRESOURCES (Model 650M) to record the forces by giving displacement inputs. We also show the deformed shape in Figure 5.18(b) and a close view in Figure 5.18(c). Deformed shapes under 0, 5 and 10 lb are shown in Figure 5.19. As compared in Figure 5.20, the experiment results of both tension and compression tests are performed and agree well with those obtained by the global coordinate model.

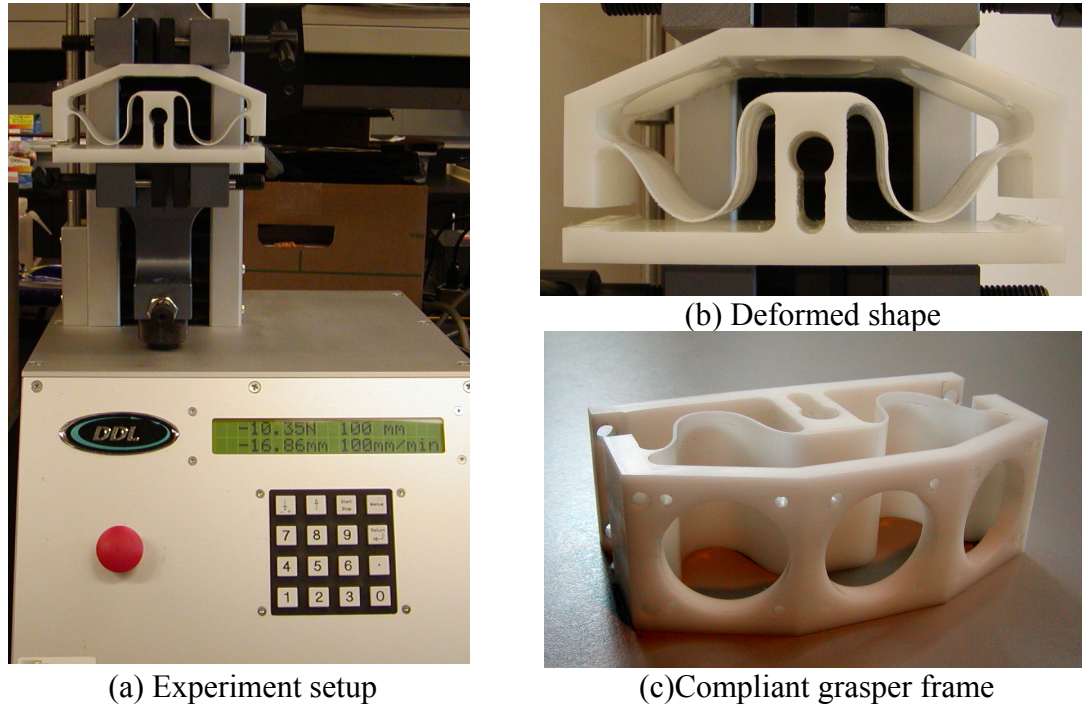


Figure 5.18 Experiment setup

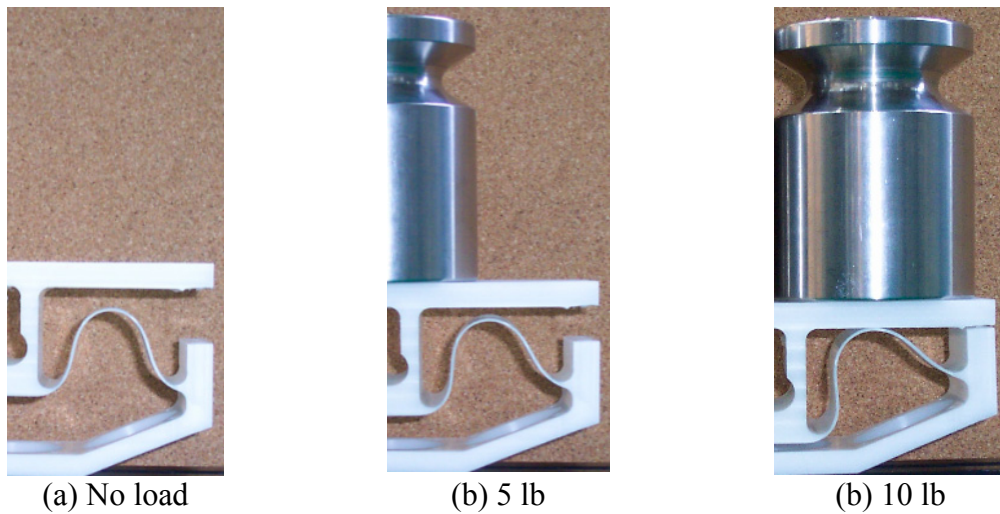


Figure 5.19 Deformation of the grasper frame under different loads

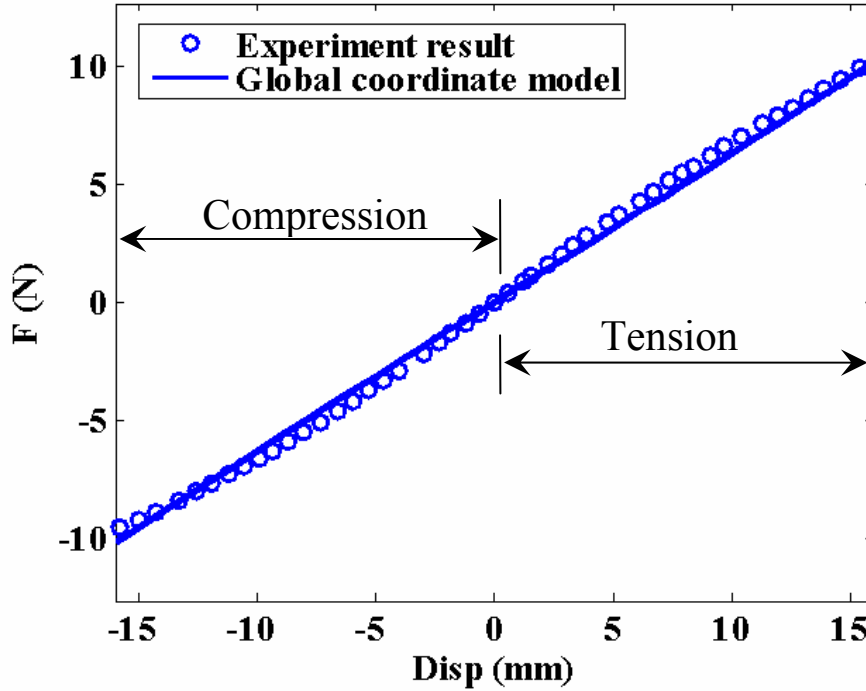


Figure 5.20 Force-displacement relations

5.7 Conclusions

This chapter presents the global coordinate model for analytical design of compliant mechanisms. This model is general in such that it automatically accounts for initially curved beams and beams with nonuniform shape. The deflection is governed by a set of differential equations with two types of constraint equations. The differential equations can be readily solved by the generalized multiple shooting method developed in Chapter 2 and 3. The global coordinate model is systematic that it can be generalized to analyzing multi-link compliant mechanisms.

Forward and inverse models are both illustrated with examples. Unlike displacement-based models, the global coordinate model can directly solve the inverse problems and thus, is suitable for initial design of compliant mechanisms. The effect of shear deformation on the deflection of a compliant link has also been characterized.

Along with the GCM, a GUI program has been developed to facilitate topology design of compliant mechanisms. Finally, we use the compliant grasper as an example to demonstrate the capability of global coordinate model in both analysis and optimization. An experiment is conducted to validate the global coordinate model for analyzing initially curved compliant links. The comparison result has shown good agreement.

CHAPTER 6

GRIPPING CONTACT MODEL

6.1 Introduction

In the previous three chapters (Chapter 3, 4, and 5), compliant mechanisms with equality (bilateral) constraints have been investigated using generalized shooting method with global coordinate model. For certain applications such as compliant grippers, some of their constraints (contact constraint) cannot be expressed as equations and hence require a different analytical tool that can deal with inequality constraints.

This chapter presents an efficient computational technique using nonlinear constrained optimization to facilitate design and analysis of compliant grippers. This technique is rather general and can be used to analyze contact between an arbitrarily shaped 2-D object and a compliant gripper with arbitrary geometry in its lateral direction. Key to this model is the expression of strain energy and formulation of geometric constraints. This remaining chapter offers the following:

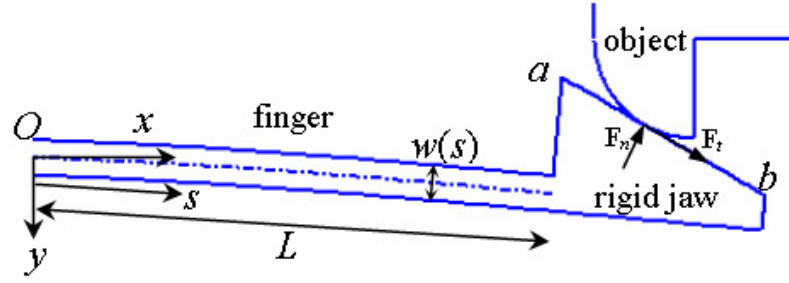
1. *A formulation based on the Nonlinear Constrained Optimization (NCO) technique.*

It offers a means to predict the deflected shape of the compliant gripper and its contact forces (both normal and tangential) with an object where the geometric shapes of the gripper cannot be ignored.

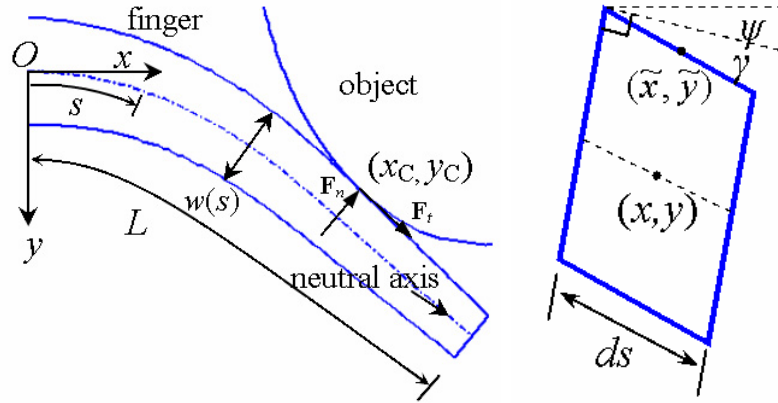
2. *Two classes of design configurations are considered. Namely, gripping with and*

without a rigid jaw as shown in Figures. 6.1(a) and 6.1(b) respectively. The former relies on indirect contact with the object through a jaw while in the latter the compliant gripper directly contacts the object.

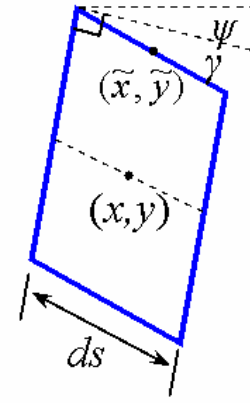
3. *A numerical solver based on Sequential Quadratic Programming method.* This method solves the nonlinear constraint optimization problems.
4. *Verification with FEM.* We simulate two examples using the proposed method and compare the computed results against those obtained using FEM; the results are in excellent agreement with simpler formulation and much less computation effort.



(a) Grip with a rigid jaw



(b) Continuous grip without a rigid jaw



(c) Differential segment

Figure 6.1 Compliant gripping contacts

While this chapter focuses on 2-D gripping contact model, the formulation of 3-D model can be found in Appendix C.

6.2 General Formulation of the Contact Problem

We formulate the compliant gripper contact problem as a nonlinear constrained optimization (NCO) problem. This begins with the strain energy expression of a compliant gripper capable of large deflection with shear deformation; followed by the formulation of geometric constraints that prevent the gripper from penetrating the object. The minimization of strain energy with geometric constraints together forms a nonlinear constrained optimization problem after discretization. Normal and tangential contact forces can be obtained by using Newton's 3rd law.

6.2.1 Formulation of strain energy

Consider the two classes of compliant grippers as shown in Figure 6.1(a) and Figure 6.1(b). The manipulation of grippers depends on the contact forces from the rigid object to make the fingers deflect in such a way that can accommodate the geometry of the object. The gripper shown in Figure 6.1(a) has a triangular jaw attached at the end while the surface of the gripper in Figure 6.1(b) is in direct contact with an elliptical object. Note that the shapes of the gripper and object are not restricted to the schematics shown in Figure 6.1.

In order to characterize the gripper deflection, we generalize Timoshenko's beam theory [1922] so that it can account for large flexural deflection with shear deformation. Timoshenko's beam theory is applicable to small deflections with assumptions that (a) the cross-section remains planar after deflection and (b) the gripper is inextensible. The

deflection of a differential segment shown in Figure 6.1(c) is interpreted as a superposition of two effects: (I) a bending moment induces an angle of rotation ψ without changing the shear angle, and (II) the shear force distorts the segment by a shear angle γ without causing it to rotate. The resultant of these effects is that the cross-section rotates by an angle $\psi + \gamma$. *Furthermore, by replacing the differential arc length ds with dx , we generalized Timoshenko's theory so that it is applicable to large deflections.* Since most deformation of the gripper is due to bending and shear, we neglect the local surface deformation (treat as rigid surface) and state the strain energy V stored in the system shown in Figure 6.1(a) and Figure 6.1(b) as

$$V = \frac{1}{2} \int_0^L \left\{ EI(s) \left(\frac{d\psi}{ds} \right)^2 + \kappa GA(s) [\gamma(s)]^2 \right\} ds \quad (6.1)$$

where s is an arc length;

A , L , and I are the cross-section area, length and moment of inertia of the gripper respectively;

E and G are respectively the Young's and shear moduli of the gripper;

ψ is the angle of rotation of the gripper;

γ is the shear angle of the gripper;

κ is the shear coefficient; and

$[x_C, y_C]^T$ is the position vector of the contact point.

The shear coefficient κ is introduced in order to correct the assumption (a) made above. In Equation (6.1), the 1st and 2nd terms in the integral account for the strain energy due to bending and shear respectively. There is no strain energy of the object since we assume it is rigid. Here we perform a quasi-static analysis and assume that the gripper and object

are on the verge to slip. The following conditions can be drawn according to this assumption.

1. The magnitude of normal force $|\mathbf{F}_n|$ and contact force $|\mathbf{F}_t|$ are related to each other by $\mu|\mathbf{F}_n|=|\mathbf{F}_t|$ where μ is kinetic friction coefficient.
2. Continue from 1, the contact point can be viewed as a rigid joint since we neglect local deformation. The work due to normal and friction force is canceled between the gripper and object. Thus the potential energy of the system only includes Equation (6.1).

From hereafter we set the x -axis pointing to the undeflected direction of the gripper and y -axis to the deflected direction. The dash line in the middle of the finger represents the neutral axis and the position of a point (x, y) on it can be obtain as

$$\begin{bmatrix} x \\ y \end{bmatrix} = \int_0^{\hat{s}} \begin{bmatrix} \cos(\psi + \gamma) \\ \sin(\psi + \gamma) \end{bmatrix} ds \quad (6.2)$$

where \hat{s} is the arc length from origin O to point (x, y) .

6.2.2 Formulation of geometric constraints

The geometric constraints are formulated in order to describe the state at contact. Specifically, the points (\tilde{x}, \tilde{y}) on the contact surface of the gripper must satisfy the following inequality in order not to penetrate the rigid object

$$g(\tilde{x}, \tilde{y}) \geq 0 \quad (6.3)$$

where $g(x, y)=0$ is the surface function that describes the contour of the object contacting the gripper. Depending on the location of contact, the points (\tilde{x}, \tilde{y}) on the contact surface for the two classes of grippers can be stated as follows:

Case I: Compliant finger with a rigid jaw (indirect contact)

Since the local deformation near contact area of the jaw is small compared with the deflection of the finger, it can be treated as a rigid body. The position (\tilde{x}, \tilde{y}) of a point on the surface of the jaw, i.e., line segment ab , can be described by the angle of rotation at $s=L$ and the point $[x(L), y(L)]$.

$$\begin{bmatrix} \tilde{x} \\ \tilde{y} \end{bmatrix} = \begin{bmatrix} x_L \\ y_L \end{bmatrix} + \begin{bmatrix} \cos(\psi_L + \gamma_L) & \sin(\psi_L + \gamma_L) \\ -\sin(\psi_L + \gamma_L) & \cos(\psi_L + \gamma_L) \end{bmatrix} \begin{bmatrix} P_x \\ P_y \end{bmatrix} \quad (6.4)$$

where the subscript L denotes the value obtained at $s=L$; and

$[P_x, P_y]^T$ is the position vector from (x_L, y_L) to (\tilde{x}, \tilde{y}) in the jaw frame (with origin at $[x_L, y_L]^T$ and axes parallel to x - y before contact);

Case II: Direct contact between compliant finger and object

When the finger surface is in direct contact with the object, an arbitrary point (\tilde{x}, \tilde{y}) on the contact surface of the finger can be related to its corresponding point on the neutral axis by

$$\begin{bmatrix} \tilde{x} \\ \tilde{y} \end{bmatrix} = \begin{bmatrix} x \\ y \end{bmatrix} + \frac{w(s)}{2} \begin{bmatrix} \sin(\psi + \gamma) \\ -\cos(\psi + \gamma) \end{bmatrix} \quad (6.5)$$

where $w(s)$ is the thickness of the finger.

6.2.3 Determination of normal and tangential contact forces

Of all the points on the contact surface, the one that satisfies the surface function $g=0$ is denoted as $\mathbf{P}_C=[x_C \ y_C]^T$. The contact force can be obtained by applying Newton's 3rd law at the gripper. Specifically, the contact forces $\mathbf{F}=[F_x \ F_y]^T$ from the gripper to the object (or $-\mathbf{F}$ from the object to the gripper) must have a moment on the gripper that equals the reaction moment at O .

$$EI(s) \frac{d\psi}{ds} \Big|_{s=0} = -\mathbf{P}_C \times \mathbf{F} \quad (6.6)$$

The contact force \mathbf{F} includes normal and tangential components that can be written in the following form.

$$\mathbf{F} = [F_x \ F_y]^T = \mathbf{F}_n + \mathbf{F}_t = [F_{nx} \ F_{ny}]^T + [F_{tx} \ F_{ty}]^T \quad (6.7)$$

The direction of normal contact force must be parallel to the gradient of the object surface at $(x_C \ y_C)$.

$$\frac{\partial g / \partial y}{\partial g / \partial x} \Big|_{(x_C, y_C)} = \frac{F_{ny}}{F_{nx}} \quad (6.8)$$

Since normal contact force and tangential (friction) contact force are orthogonal to each other, we have

$$F_{nx} F_{tx} = F_{ny} F_{ty} \quad (6.9)$$

Since the contact surface is on the verge to slip, the magnitude of normal force relates to the magnitude of friction force by

$$\mu \sqrt{F_{nx}^2 + F_{ny}^2} = \sqrt{F_{tx}^2 + F_{ty}^2} \quad (6.10)$$

where μ is the kinetic friction coefficient. The components F_{nx} , F_{ny} , F_{tx} , and F_{ty} can be solved simultaneously from Equations (6.6), (6.8), (6.9), and (6.10). Note that the signs of F_{tx} and F_{ty} have to be determined from the direction of interaction between the gripper and object.

In the case of frictionless contact, only normal contact force $\mathbf{F}_n = [F_{nx} \ F_{ny}]^T$ needs to be considered. The x component F_{nx} and y component F_{ny} can be solve simultaneously from Equations (6.6) and (6.8).

6.2.4 Numerical discretization

In order to obtain the deflected shape of the gripper, we apply the principle of minimum potential energy for Equation (6.1) with geometric constraints Equation (6.3). Specifically, the principle of minimum potential energy states that of all admissible displacements, those that satisfy the equilibrium condition at contact make the total potential energy minimum. Namely, we are trying to find the minimum of V from Equation (6.1) with the admissible displacements imposed by Equation (6.3). Rather than seeking for a closed-form solution, we resort to numerical approximations by discretizing the neutral axis of the finger into N equally spaced intervals and the contact surface into M equally spaced intervals. We use capital letters to denote the approximated values of the variables as follows:

$$\begin{aligned} s_i &= i\Delta s, \Delta s = L/N, i = 0 \sim N \\ \Psi_i &\approx \psi_i = \psi(s_i); \Gamma_i \approx \gamma_i = \gamma(s_i), i = 0 \sim N \\ X_i &\approx x_i = x(s_i); Y_i \approx y_i = y(s_i), i = 0 \sim N \\ \tilde{X}_j &\approx \tilde{x}_j = \tilde{x}(s_j); \tilde{Y}_j \approx \tilde{y}_j = \tilde{y}(s_j), j = 0 \sim M \end{aligned} \tag{6.11}$$

Hence we can approximate Equation (6.1) by, but not restricted to, the trapezoidal rule:

$$V \approx \frac{1}{2} \Delta s \left[\sum_{i=1}^N EI_{i-1/2} \left(\frac{\Psi_i - \Psi_{i-1}}{\Delta s} \right)^2 + \kappa G A_{i-1/2} \left(\frac{\Gamma_i^2 + \Gamma_{i-1}^2}{2} \right) \right] \tag{6.12}$$

The area A and moment of inertia I are approximated as

$$I_{i-1/2} = \frac{I(s_i) + I(s_{i-1})}{2}; \text{ and } A_{i-1/2} = \frac{A(s_i) + A(s_{i-1})}{2} \tag{6.13}$$

Since the gripper is clamped at the base, the initial angle of rotation (ψ_0) and position (x_0, y_0) are equal to zero.

$$\Psi_0 = 0; X_0 = 0; \text{ and } Y_0 = 0 \quad (6.14)$$

Follow from Equation (6.2), any point on the neutral axis of the finger can be approximated as

$$\begin{aligned} X_i &= \frac{1}{2} \sum_{k=0}^{i-1} [\cos(\Psi_k + \Gamma_k) + \cos(\Psi_{k+1} + \Gamma_{k+1})] \Delta s \\ Y_i &= \frac{1}{2} \sum_{k=0}^{i-1} [\sin(\Psi_k + \Gamma_k) + \sin(\Psi_{k+1} + \Gamma_{k+1})] \Delta s \end{aligned} \quad (6.15)$$

where $i=1 \sim N$. The points on the contact surface can be obtained by plugging Equation (6.15) into Equation (6.4) or (6.5). The approximated (\tilde{X}, \tilde{Y}) is then substituted into Equation (6.3)

$$g_j(\tilde{X}_j, \tilde{Y}_j) \geq 0; j = 1 \sim M \quad (6.16)$$

Equation (6.12) is a quadratic object function that has to be minimized subject to the constraint functions from Equation (6.16) with independent variables Ψ_i and Γ_i ($i=1 \sim N$). The numerical solvers for obtaining the optimal solution will be presented in Section 6.3. Note that the number of intervals M for the neutral axis, in general, does not have to be equal to the number of intervals N of the contact surface.

6.3 Sequential (Successive) Quadratic Programming

In this section we introduce a numerical algorithm based on sequential quadratic programming (SQP) to solve the optimization problem governed by Equations (6.12) and (6.16). The general nonlinear minimization problem with inequality constraints can be stated as follows:

$$\min f(\mathbf{x}) \quad (6.17)$$

subject to $g_i(\mathbf{x}) \geq 0, i = 1 \sim M$

where g_i is the i^{th} inequality constraint function.

The idea of SQP is to approximate the current state (say, \mathbf{x}_k) by a quadratic programming (QP) sub-problem as

$$\begin{aligned} \min \quad & \frac{1}{2} \mathbf{p}^T \nabla^2 L(\mathbf{x}_k) \mathbf{p} + \nabla f_k^T \mathbf{p} \\ \text{subject to} \quad & \nabla g_i(\mathbf{x}_k) \mathbf{x}_k + g_i(\mathbf{x}_k) \geq 0, i = 1 \sim M \end{aligned} \quad (6.18)$$

where $\mathbf{p} = \mathbf{x} - \mathbf{x}_k$ and $L = f(\mathbf{x}) + \sum_{i=1}^m \lambda_i g_i(\mathbf{x})$

Equation (6.18) contains a quadratic approximation of $f(\mathbf{x})$ and linear approximations of $g_i(\mathbf{x})$. The minimizer of Equation (6.16) is then used to define a new state by setting $\mathbf{x}_{k+1} = \mathbf{x}_k + \mathbf{p}$. The minimizer of the QP should be the optimal solution of Equation (6.17) when the iterative process converges. The disadvantages of SQP are that the computation of Hessian matrix $\nabla^2 L(\mathbf{x}_k)$ is time-consuming for large problems and that it may not be positive definite. Various quasi-Newton algorithms can be used to approximate Hessian matrix. Here we adopt the popular BFGS algorithm (by Bryoden, Fletcher, Goldfarb, and Shanno). The formulae are stated as follows [Bazaraa *et al.*, 1993]:

$$\tilde{\mathbf{W}}_{k+1} = \tilde{\mathbf{W}}_k + \frac{\mathbf{q}_k \mathbf{q}_k^T}{\mathbf{q}_k^T \mathbf{p}_k} - \frac{\tilde{\mathbf{W}}_k \mathbf{p}_k \mathbf{p}_k^T \tilde{\mathbf{W}}_k}{\mathbf{p}_k^T \tilde{\mathbf{W}}_k \mathbf{p}_k} \quad (6.19)$$

where

$$\mathbf{p}_k = \mathbf{x}_{k+1} - \mathbf{x}_k \quad (6.19a)$$

and

$$\mathbf{q}_k = \nabla f(\mathbf{x}_{k+1}) - \nabla f(\mathbf{x}_k) + \nabla \sum_{i=1}^m \lambda_{k+1,i} [g_i(\mathbf{x}_{k+1}) - g_i(\mathbf{x}_k)] \quad (6.19b)$$

$\tilde{\mathbf{W}}_{k+1}$ is the approximation Hessian for the next step. The steps for the SQP are outlined as below.

Computational Steps

Given initial \mathbf{x}_0 , $\tilde{\mathbf{W}}_0$, $\lambda_{0,i}$ ($i=1 \sim m$), $\beta \in [0,1]$, and tolerance ε :

1. Solve Equation (6.18) for \mathbf{p} and $\lambda_{k+1,i}$ ($i=1 \sim m$)
2. For $k=0,1,2 \dots$

Set $\mathbf{x}_{k+1} = \mathbf{x}_k + \beta \mathbf{p}$

While $f_{k+1} > f_k$

$$\mathbf{x}_{k+1} = \mathbf{x}_k + \beta(\mathbf{x}_{k+1} - \mathbf{x}_k)$$

End

Obtain BFGS update matrix $\tilde{\mathbf{W}}_{k+1}$ from Equation (6.19).

If $|f(\mathbf{x}_{k+1})| < \varepsilon$, exit

End

6.4 Verification of Frictionless and Frictional Contact

In this section we illustrate with two examples to verify the NCO technique introduced in Section 6.2. In Example I, we consider an indirect gripping contact where the object contacts with the gripper through a triangular jaw. In Example II the direct contact of the gripper with an elliptical object is considered. The simulation results are then compared against those obtained by using FEM. Both frictionless and frictional contacts will be considered. Note that in Example I we need not consider shear deformation since finger thickness is relatively small.

Example I: Passive gripper for micro-assembly

The assembly process using a compliant gripper includes insertion, deflection, and assembly. An effective assembly requires designing the geometry of the gripper and its jaw such that it is easy to insert but very difficult to pull out. For clarity, we consider in Figure 6.2 a gripper with a triangular jaw and a circular object surface. Due to symmetry, only half of the gripper needs to be considered.

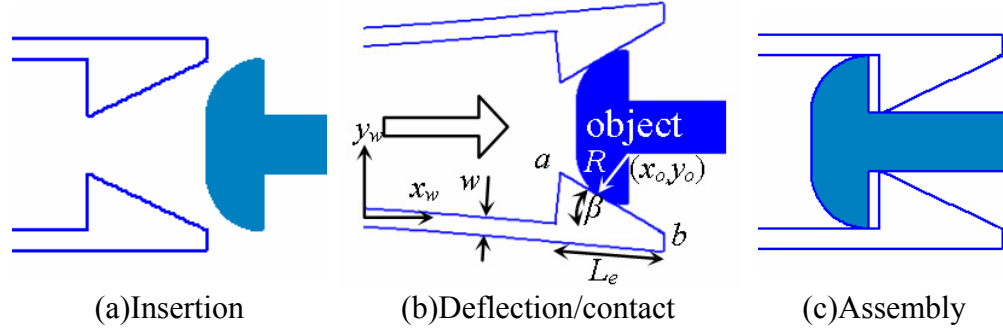


Figure 6.2 Gripper assembly sequence

Since only segment ab on the jaw contacts with the object, we only need to discretize surface ab into M equally spaced intervals. The geometric constraints can be obtained by using the equation of a circle

$$g_j(\tilde{X}_j, \tilde{Y}_j) = (\tilde{X}_j - x_o)^2 + (\tilde{Y}_j - y_o)^2 - R^2 \geq 0 \quad (6.20)$$

where R is the radius of the extrusion part of the object and (x_o, y_o) is the center of the circle as shown in Figure 6.2(b). The simulation parameters for both the NCO technique and FEM are listed in Table 6.1. Figures 6.3 and 6.4 show the forces required as the gripper inserts into the fixture. The NCO technique matches well with FEM with differences less than 3%. Figure 6.5 also shows the deflection shape obtained by ANSYS where $x_o = 0.06781\text{m}$. The comparison of computation time of this particular result in

Table 6.2 shows that the NCO technique is more efficient than FEM without losing accuracy.

Table 6.1 Simulation parameters and values

Parameters	Values	Parameters	Values
Young's modulus(N/m^2)	2.6×10^9	element type for ANSYS	PLANE2 for both gripper and object
Lead angle β	25°	# of elements for ANSYS	1266
Thickness w	0.0032m	N	100
Width b	0.0095m	M	100
Finger length L	0.057m		
Jaw length L_e	0.019m		
Fixture radius R	0.0089m		
Fixture position y_o	0.0105m		

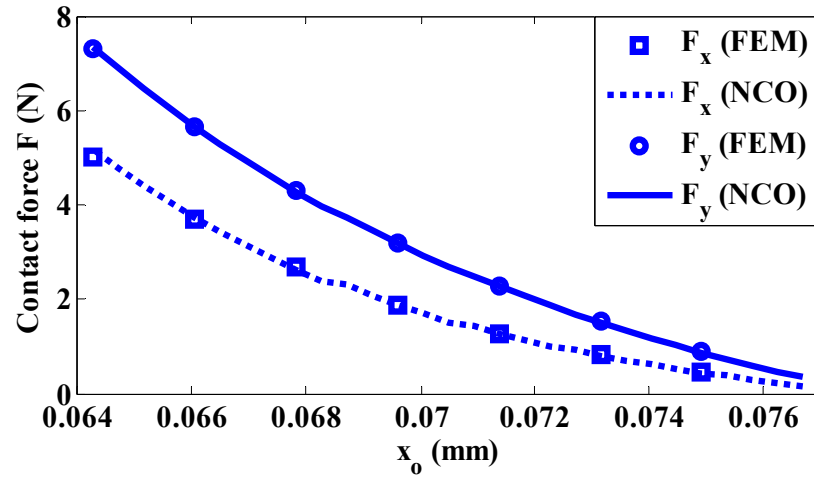


Figure 6.3 Simulation result of a gripper assembly ($\mu=0$)

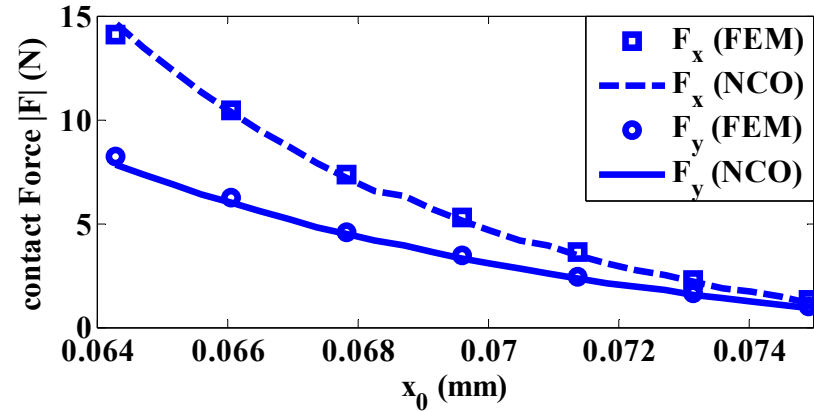


Figure 6.4 Simulation result of a gripper assembly ($\mu=0.5$)

1
DISPLACEMENT
STEP=1
SUB =175
TIME=100
DMX =.005715

ANSYS
FEB 12 2005
23:25:24

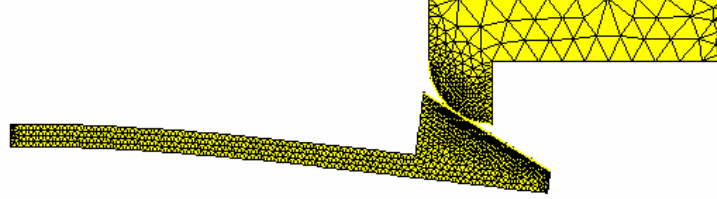


Figure 6.5 Simulation results from FEM

Table 6.2 Comparison of computation time

Method	Time(sec)
NCO(without shear deformation)	20.95
FEM(ANSYS)	516.463

Example II: Gripper for object handling

In this example we illustrate an application where the gripper manipulates an object by direct contact through the finger. The finger needs to make contact with the object. For ease of illustration, we consider a case where a nonuniform gripper manipulates an elliptical object as shown in Figure 6.6. We perform a quasi-static analysis where the relationship between the moving object and rotating finger can be described by

$$\phi = -236.22x_e + 102^\circ \quad (6.21)$$

where x_e is in meters and ϕ is the rotation between gripper frame xy and world frame x_wy_w . The contact surface includes one side of the finger that approaches the object. Since the contact location is unknown, the whole finger surface needs to be discretized and the geometric constraints can be obtained by using the equation of an ellipse.

$$g_j = b_1 \tilde{X}_j^2 + b_2 \tilde{Y}_j^2 + b_3 \tilde{X}_j \tilde{Y}_j + b_4 \tilde{X}_j + b_5 \tilde{Y}_j + b_6 \geq 0 \quad (6.22)$$

where b_i 's are the coefficients of the elliptical object.

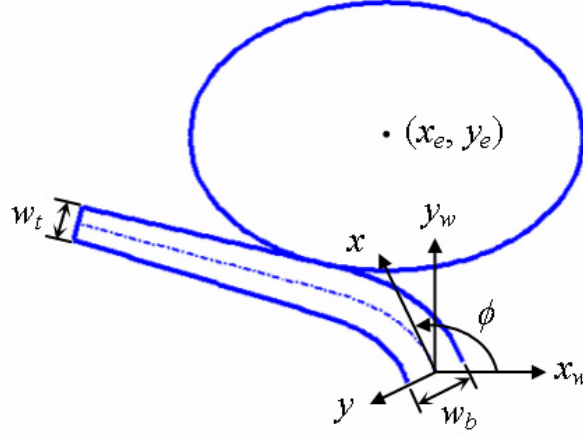


Figure 6.6 Schematics of a rotating gripper contacting an object

As mentioned in Section 6.2, Timoshenko's beam theory includes a shear coefficient κ . Various shear coefficient formulae have been proposed. As shown in Equation (6.23), we adopt the shear coefficient formula suggested by Kaneko [1975] to correct the shear angles of grippers with rectangular cross-section.

$$\kappa = (5 + 5\nu)/(6 + 5\nu) \quad (6.23)$$

where ν is Poisson's ratio. We again compare the results of the NCO technique with FEM. Simulation parameters are listed in Table 6.3. Figure 6.7 shows the continuous snapshots where the object moves from left to right while the gripper rotating clockwise. The computation time of $x_e=0.0508\text{m}$ is compared in Table 6.4. In Figure 6.8 we compare the results of frictionless contact by using the NCO technique (with and without shear effect), FEM and a one-dimensional model (treat finger as a line segment without considering lateral thickness, say, Frisch-Fay's model). In Figure 6.9, the results of frictional contact are also compared with direction of friction force pointing to the positive x axis. We also show in Figure 6.10 the angle of rotation ψ and shear angle γ at $x_e = -0.0254\text{m}$. It is

apparent that the contact point locates around $s = 0.08\text{m}$. There is no deformation after the contact point and hence, ψ remains constant and γ becomes zero.

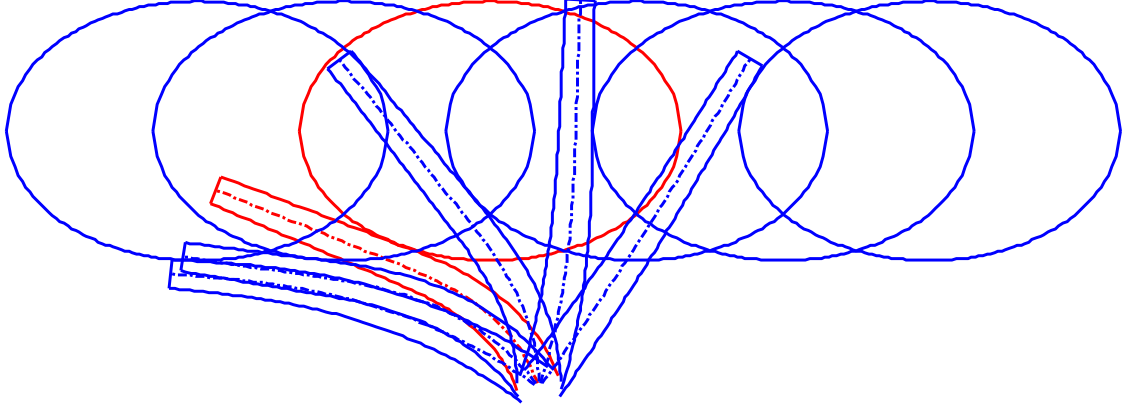


Figure 6.7 Snapshots of gripper-ellipse contact

($\phi=144^\circ, 126^\circ, 108^\circ, 90^\circ, 72^\circ, 54^\circ$ from left to right)

Table 6.3 Simulation parameters and values

Parameters	Values	Parameters	Values
Young's modulus	$4.8 \times 10^6 \text{ N/m}^2$	element type for ANSYS	PLANE2 for ellipse and PLANE42 for gripper
Shear modulus	$1.71 \times 10^6 \text{ N/m}^2$	# of elements for ANSYS	1080
Poisson's ratio	0.4	N	90
Base thickness w_b	0.030m	M	90
Tip thickness w_t	0.017m		
Width b	0.025m		
Ellipse long axis	0.09906m		
Ellipse short axis	0.06731m		
Ellipse position y_e	0.12065m		

Table 6.4 Comparison of computation time

Method	Time(sec)
NCO(without shear deformation)	15.352
NCO(with shear deformation)	33.358
FEM(ANSYS)	222.42

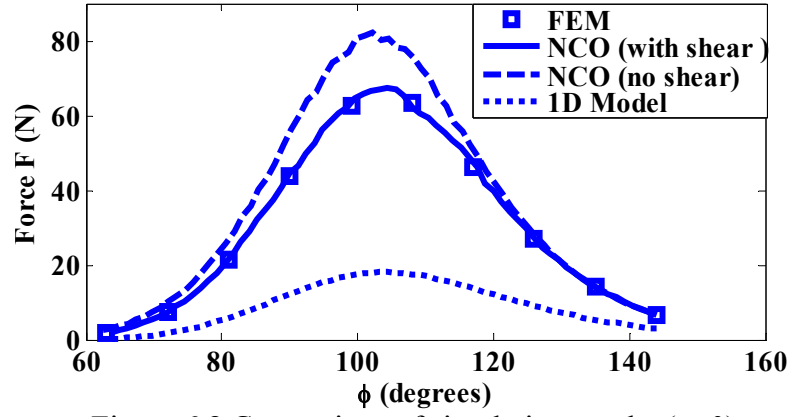


Figure 6.8 Comparison of simulation results ($\mu=0$)

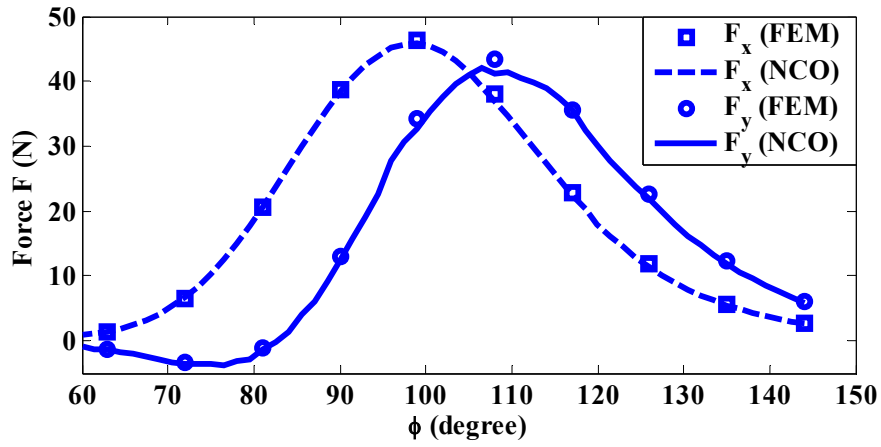


Figure 6.9 Comparison of simulation results ($\mu=0.5$)

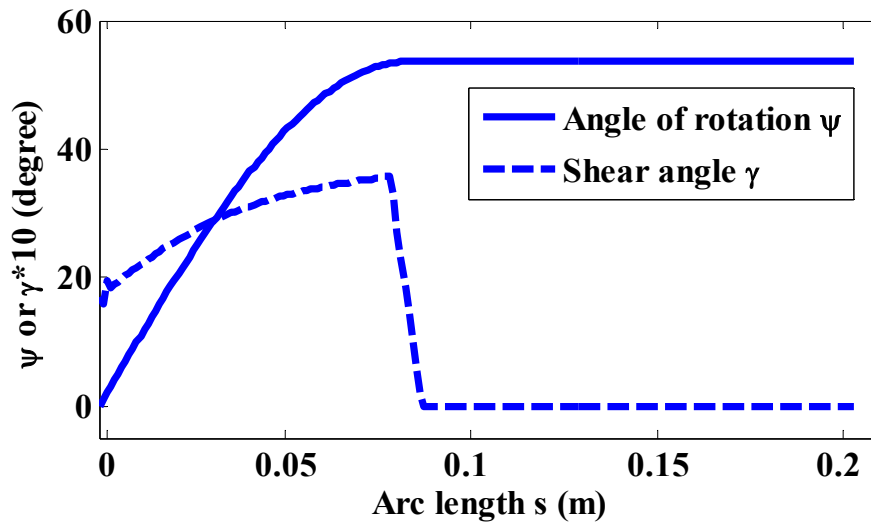


Figure 6.10 Angle of rotation and shear angle at $x_e = -0.0254\text{m}$ and $\phi=108^\circ$

The following observations can be made from the comparison between NCO and other existing methods:

1. The one-dimensional model, which treats the finger as a line segment, ignores the geometry of the finger hence is only applicable for fingers with relatively small thickness. The error of contact forces will increase as the thickness increases.
2. When applying the NCO technique without considering shear deformation of the gripper, the error increases as contact force increases. The overall contact forces also tend to be higher than those with considering shear deformation. When considering shear deformation, the predicted contact forces obtained from the NCO technique matches well with FEM. Typical differences are within 3%. Without losing accuracy, the NCO technique, which discretizes the finger in one dimension (along the neutral axis), is far faster than FEM which discretizes the gripper in two dimensions (along the neutral axis and transverse direction).
3. The excellent agreement of the NCO technique and FEM also verifies that the assumption of small surface deformation is valid for frictionless contact and frictional contact with moderate friction coefficient.
4. In order to satisfy the boundary conditions of gripper/object surface, FEM requires discretization of both gripper and object surface while the NCO technique only needs to discretize the gripper surface. Hence the formulation of NCO can be simpler.

6.5 Conclusions

A computational model based on Nonlinear Constrained Optimization (NCO) techniques has been presented for analyzing compliant grippers whose manipulation relies on direct or indirect contact with the objects. The model takes into account large

flexural deflection and shear deformation whose effect can not be neglected for thick fingers. By formulating geometric constraints this model can be applied to nonuniform fingers and jaws with arbitrary geometry.

Two types of compliant grippers have been presented to illustrate the formulation. Both frictionless and frictional contacts have been considered. The simulation results of NCO technique agree well with those obtained by using FEM with difference typically within 3%. Compared with FEM, the advantages of the NCO technique are the following: (a) The dimension of discretization can be reduced by one, namely, 2-D problem can be reduced to 1-D and 3-D problem can be reduced to 2-D. Hence it is computationally much more efficient than FEM. (b) The object domain need not be discretized. Hence its formulation is simpler than FEM.

The excellent agreement shows that the formulation and analysis offered by the NCO technique can effectively facilitate the process of design and optimization of compliant grippers that have a broad spectrum of applications ranging from MEMS device fabrication [Tsui *et al.*, 2004] to automated handling of live objects in food processing industry [Lee *et al.*, 1996]. The formulation can also be further extended to compliant grippers with external actuators.

CHAPTER 7

CONCLUSIONS AND FUTURE WORKS

7.1 Conclusions

A rather complete set of computational models have been presented in this thesis to analyze and design planar compliant mechanisms. The models are capable of mechanisms with both clamped/revolute joints and gripping contact conditions. In summary, we conclude this thesis research with the following three paragraphs.

(1) The generalized shooting method (GSM):

In Chapter 2, we proposed the generalized shooting method as the computational basis for analyzing compliant mechanisms. As the method is rather generic, it can be applied to any compliant link models that are governed by sets ordinary differential equations. Comparisons of generalized shooting method with other existing methods are made and the advantages of GSM are highlighted.

(2) The global coordinate model (GCM):

We developed the global coordinate model in Chapter 3 and 5 for analyzing compliant mechanisms. This is a distributed-parameter type model that can account for large deflection with nonuniform link geometry as well as nonlinear material properties. Bending, axial and shear deformations are all captured in this model. Both dynamic and static examples are given with verifications. Systematic procedures are formulated to

analyze compliant mechanisms with arbitrary link numbers and connection types. Forward and inverse problems are addressed to show that this model is an excellent candidate for both analysis and design of compliant mechanisms. Finally an illustrative example is given to demonstrate how this model can be applied to real problems.

(3) The gripping contact model and nonlinear constrained optimization technique (NCO):

In Chapter 6 we proposed the gripping contact model for analyzing compliant grippers. We used the global coordinate model to capture the deformation of the gripper with geometric constraints that describe contact boundary conditions. The model was solved using nonlinear optimization technique. It was demonstrated that this technique essentially reduces the order of computation by one with errors less than 3%. The proposed technique is also significantly faster than popular finite element method. Both frictional and frictionless problems were investigated.

As the computational models have immediate applications in designing compliant mechanisms for robotic grasping, it is expected that the models can serve as a basis for design and analysis of a wide spectrum of compliant mechanisms.

7.2 Future Works

Some recommendations for further improving the computational models are summarized as follows:

(1) In this thesis, compliant members are assumed to deflect in one direction only. In other words, we only consider planar compliant mechanisms. Although most compliant mechanisms are designed for planar manipulation, there are certain applications where three dimensional models are necessary. Examples include compliant rubber finger applied for 3-D object handling [Lee, 1999], space robot arm, and electroactive polymers.

To make the global coordinate model complete, we list some of the future works for developing three dimensional link models.

- The generalized shooting method is readily applicable to any models that are governed by ordinary differential equations. Hence we can extend Equation (3.10) to predict three dimensional deformation using GSM.
- The gripping contact model developed in Chapter 6 can also be extended to analyze 3-D compliant grippers. We present the 3-D gripping contact model in Appendix C.

(2) For broader applications such as control and vibration analysis of compliant mechanisms, close form equations are necessary. By using the power series method (Appendix D), the governing equations of the global coordinate model can be approximated by algebraic equations.

(3) In addition, the gripping contact model is a quasi-static model that does not consider the dynamic interaction between grippers and the object. Although dynamic contact models are well developed for rigid bodies, it remains a challenge to develop dynamic compliant contact model for grasping problems.

APPENDIX A

ALTERNATIVE COMPLIANT LINK MODELS

Although we suggest the proposed global coordinate model for analyzing compliant mechanisms, there are other alternatives that can capture the deformation of a compliant link. As long as the link model can be represented by ordinary differential equations, it can be solve by the generalized shooting method proposed in Chapter 2.

Two additional link models are introduced here as alternatives. The first model extends the large deflection capability to predict the axial deformations. The second model uses x as the independent variable and includes Karman strains in the potential energy function to account for moderate deflection (transverse normal around $10^\circ \sim 15^\circ$). These two models can be explored in the same way using generalized shooting method to analyze general compliant mechanisms.

A.1 Link Model With Large Deflection And Axial Deformation

The Frisch-Fay model [1962] in Chapter 2 is limited to compliant mechanisms with negligible effect of axial deformation. In order to account for such effect, we extend the Frisch-Fay model by including axial deformation terms. The governing equations are derived by using the principle of minimum potential energy which can be formulated as follows:

$$V = \frac{1}{2} \int_0^L \left\{ EI \left(\frac{d\psi}{ds} \right)^2 + EA \left(\frac{de}{ds} \right)^2 \right\} ds - F_x x(L) - F_y y(L) \quad (\text{A.1})$$

where e is the axial displacement; and F_x, F_y are applied forces at the tip along positive x and y directions. By means of standard manipulation of variational calculus, we obtain the normalized governing equation of a flexible link as

$$\begin{aligned} F_x \left(\frac{e'}{L} + 1 \right) \sin \psi - F_y \left(\frac{e'}{L} + 1 \right) \cos \psi &= \frac{EI}{L^2} \psi'' \\ -F_x \frac{\psi'}{L} \sin \psi + F_y \frac{\psi'}{L} \cos \psi &= \frac{EA}{L^2} e'' \end{aligned} \quad (\text{A.2})$$

where $()' = d() / du$ and $u=s/L$. By introducing state-space variables

$$[q_1 \quad q_2 \quad q_3 \quad q_4] = [\psi \quad \psi' \quad e \quad e'],$$

we can recast Equation (A.2) as 1st order ODE's with $n=4$.

$$\begin{aligned} q_1' &= q_2 \\ q_2' &= \frac{L^2}{EI} \left[F_x \left(\frac{q_4}{L} + 1 \right) \sin q_1 - F_y \left(\frac{q_4}{L} + 1 \right) \cos q_1 \right] \\ q_3' &= q_4 \\ q_4' &= \frac{L}{EA} \left(-F_x q_4 \sin q_3 + F_y q_4 \cos q_3 \right) \end{aligned} \quad (\text{A.3})$$

The known and unknown initial values for a clamped link are given by

$$\text{Known I.C.: } q_1(0) = 0, q_3(0) = 0$$

$$\text{Unknown I.C.: } q_2, q_4$$

In order to solve Equation (A.3) using generalized shooting method, the following terminal conditions must be satisfied for an applied tip force.

$$q_2(L) = 0$$

$$\left[EA \frac{q_4}{L} - F_x \cos q_1 - F_y \sin q_1 \right]_L = 0$$

After obtaining the solution, the position of the tip C can be obtained from the following integral equation.

$$\begin{bmatrix} x_C \\ y_C \end{bmatrix} = L \int_0^1 \begin{bmatrix} (1+e') \cos \psi \\ (1+e') \sin \psi \end{bmatrix} du \quad (\text{A.4})$$

Note that the positions of the tip have to be obtained from Equation (A.4) after solving Equation (A.3). The global coordinate model, on the other hand, can directly obtain the tip position after solving the ODE's.

A.2 Euler-Bernoulli-Von Karman Equations of Compliant Links

The potential energy function using Karman strains [Reddy, 1999] is formulated as follows:

$$V = \frac{1}{2} \int_0^L \left\{ EA \left[\frac{de}{dx} + \frac{1}{2} \left(\frac{dy}{dx} \right)^2 \right]^2 + EI \left(\frac{d^2 y}{dx^2} \right)^2 \right\} dx - F_y y(L) - F_x e(L) \quad (\text{A.5})$$

where y is the transverse displacement. Similarly, we can obtain the normalized Euler-Bernoulli-von Karman equations of links using variational calculus.

$$\left\{ EA \left[Le' + \frac{1}{2} (y')^2 \right] \right\}' = 0; \quad (EI y'')'' - \left\{ y' EA \left[Le' + \frac{1}{2} (y')^2 \right] \right\}' = 0 \quad (\text{A.6})$$

where $()' = d()/dv$ and $v=x/L$. Compared with Equation. (A.2), (A.6) uses the x coordinate of the undeflected link as the independent variable, which makes it insufficient to predict very large deflection [Hodges, 1984]. Note that by setting $A=0$, Equation (A.6) collapses to the classical Euler-Bernoulli equation. Next we define

$$[q_1 \ q_2 \ \dots \ q_6] = [e \ w \ e' \ w' \ w'' \ w''']$$

so that Equation (A.5) can be recast as 1st-order ODE's with $n=6$.

$$q'_1 = q_3$$

$$q'_2 = q_4$$

$$q'_3 = -\frac{A'}{A} \left(q_3 + \frac{1}{2L} q_4^2 \right) - \frac{1}{L} q_4 q_5$$

(A.7)

$$q'_4 = q_5$$

$$q'_5 = q_6$$

$$q'_6 = -\frac{2I'}{I} q_6 - \frac{I''}{I} q_5 + \frac{A'}{I} \left(Lq_3 q_4 + \frac{1}{2} q_4^3 \right) + \frac{A}{I} \left(Lq_5 q_3 + \frac{3}{2} q_4^2 q_5 + Lq_4^2 \right)$$

For a compliant link clamped at the base, we have the following known and unknown initial values.

Known I.C.: $q_1 = q_2 = q_4 = 0$ at $x=0$; Unknown I.C.: q_3, q_5, q_6 at $x=0$

To solve Equation (A.7) using generalized shooting method, the following terminal conditions must be satisfied for an applied force at the tip.

$$EA \left(Lq_3 + \frac{1}{2} q_4^2 \right) = L^2 F_x$$

$$q_5 = 0$$

$$EAq_4 \left(Lq_3 + \frac{1}{2} q_4^2 \right) - EI'q_5 - EIq_6 = L^3 F_y \text{ at } x=L$$

Note that in order for Equation (A.6) to analyze compliant mechanisms, coordinate transformation matrices are needed among compliant links. The proposed global coordinate model does not suffer from this problem.

APPENDIX B

DERIVATION OF EQUATIONS GOVERNING A COMPLIANT LINK

In this appendix we present the derivation of Equation (3.9) using standard procedures of variational calculus. We first construct one-parameter comparison functions Ψ, X, Y, Γ , and R .

$$\begin{aligned}\Psi(s, t) &= \psi(s, t) + \varepsilon \eta_1(s, t); X(s, t) = x(s, t) + \varepsilon \eta_2(s, t); Y(s, t) = y(s, t) + \varepsilon \eta_3(s, t) \\ \Gamma(s, t) &= \gamma(s, t) + \varepsilon \eta_4(s, t); R(s, t) = e(s, t) + \varepsilon \eta_5(s, t)\end{aligned}\tag{B.1}$$

where η_i 's are arbitrary differentiable functions and $\eta_i(s, t_1) = \eta_i(s, t_2) = 0$ as required by Hamilton's principle; and ε is the parameter of the family. Further we replace (ψ, γ, x, y, e) in Equation (3.5) by (Ψ, Γ, X, Y, R) and obtain

$$J^*(\varepsilon) = \int_{t_1}^{t_2} \left[\int_0^L \frac{1}{2} (I_\rho (\dot{\Psi})^2 + A_\rho \dot{X}^2 + A_\rho \dot{Y}^2 - EI(\Psi')^2 - \kappa GA \Gamma^2 - EA(R')^2) - h g_1 - v g_2 ds \right] dt. \tag{B.2}$$

For simplicity we omit non-conservative forces in Equation (B.2). We then form the derivative $dJ^* / d\varepsilon$ at $\varepsilon = 0$

$$\left. \frac{dJ^*}{d\varepsilon} \right|_{\varepsilon=0} = \int_{t_1}^{t_2} \left\{ \int_0^L \begin{bmatrix} I_\rho \dot{\psi} \dot{\eta}_1 + A_\rho \dot{x} \dot{\eta}_2 + A_\rho \dot{y} \dot{\eta}_3 - EI \psi' \eta_1' - \kappa GA \gamma \eta_4 - EA e' \eta_5' - h \eta_2' - v \eta_3' \\ + (v(e' + 1) \cos(\psi + \gamma) - h(e' + 1) \sin(\psi + \gamma)) \eta_1 \\ + (v(e' + 1) \cos(\psi + \gamma) - h(e' + 1) \sin(\psi + \gamma)) \eta_4 \\ + (h \cos(\psi + \gamma) + v \sin(\psi + \gamma)) \eta_5' \end{bmatrix} ds \right\} dt \tag{B.3}$$

Since $\eta_i(s, t_1) = \eta_i(s, t_2) = 0$, we express the 1st, 2nd, and 3rd terms in the integrand of Equation (B.3) as follows using integration by parts.

$$\begin{aligned} \int_{t_1}^{t_2} \int_0^L I_\rho \dot{\psi} \dot{\eta}_1 ds dt &= - \int_{t_1}^{t_2} \int_0^L I_\rho \ddot{\psi} \eta_1 ds dt, \quad \int_{t_1}^{t_2} \int_0^L A_\rho \dot{x} \dot{\eta}_2 ds dt = - \int_{t_1}^{t_2} \int_0^L A_\rho \ddot{x} \eta_2 ds dt \\ &\text{and} \quad \int_{t_1}^{t_2} \int_0^L A_\rho \dot{y} \dot{\eta}_3 ds dt = - \int_{t_1}^{t_2} \int_0^L A_\rho \ddot{y} \eta_3 ds dt \end{aligned} \quad (\text{B.4})$$

The 4th, 6th, 7th, 8th, and 11th terms in the integrand of Equation (B.3) can be expressed as

$$\begin{aligned} \int_0^L EI \psi' \eta_1' ds &= [EI \psi' \eta_1]_0^L - \int_0^L EI \psi'' \eta_1 ds, \quad \int_0^L EA e' \eta_5' ds = [EA e' \eta_5]_0^L - \int_0^L EA e'' \eta_5 ds \\ \int_0^L h \eta_2' ds &= [h \eta_2]_0^L - \int_0^L h' \eta_2 ds, \quad \int_0^L v \eta_3' ds = [v \eta_3]_0^L - \int_0^L v' \eta_3 ds, \text{ and} \\ \int_0^L (h \cos(\psi + \gamma) + v \sin(\psi + \gamma)) \eta_5' ds &= [(h \cos(\psi + \gamma) + v \sin(\psi + \gamma)) \eta_5]_0^L \\ &- \int_0^L \eta_5 (h \cos(\psi + \gamma) + v \sin(\psi + \gamma))' ds \end{aligned} \quad (\text{B.5})$$

Plug in Equations (B.4) and (B.5) back into Equation (B.3) we get

$$\int_{t_1}^{t_2} \left\{ \begin{aligned} &[-h \eta_2 - v \eta_3 - EI \psi' \eta_1 + (h \cos(\psi + \gamma) + v \sin(\psi + \gamma) - EA e' \eta_5)]_0^L \\ &+ \int_0^L \left[\begin{aligned} &(EI \psi'' - I_\rho \ddot{\psi} - h(e' + 1) \sin(\psi + \gamma) + v(e' + 1) \cos(\psi + \gamma)) \eta_1 \\ &- (A_\rho \ddot{x} - h') \eta_2 - (A_\rho \ddot{y} - v') \eta_3 + (v(e' + 1) \cos(\psi + \gamma) - h(e' + 1) \sin(\psi + \gamma) - \kappa GA \gamma) \eta_4 \\ &+ (EA e'' - (v \sin(\psi + \gamma) + h \cos(\psi + \gamma))') \eta_5 \end{aligned} \right] ds \end{aligned} \right\} dt = 0$$

We temporarily let $\eta_i(0) = \eta_i(L) = 0$, and since $h(s, t)$ and $v(s, t)$ are arbitrary functions, the resulting system of partial differential equations that governs the dynamics of large-deflected link can be written as follows:

$$\begin{aligned} EI \psi'' - I_\rho \ddot{\psi} + v(e' + 1) \cos(\psi + \gamma) - h(e' + 1) \sin(\psi + \gamma) &= 0 \\ A_\rho \ddot{x} - h' &= 0, \quad A_\rho \ddot{y} - v' = 0 \\ x' - (e' + 1) \cos(\psi + \gamma) &= 0, \quad y' - (e' + 1) \sin(\psi + \gamma) = 0 \end{aligned} \quad (\text{B.6})$$

$$EAe'' - (v \sin(\psi + \gamma) + h \cos(\psi + \gamma))' = 0$$

$$v(e' + 1) \cos(\psi + \gamma) - h(e' + 1) \sin(\psi + \gamma) - \kappa GA \gamma = 0$$

When the link is clamped at $s=0$ and free at $s=L$, the geometric boundary conditions are given as follows:

$$\psi(0, t) = 0, x(0, t) = y(0, t) = 0, e(0, t) = 0 \quad (\text{B.7})$$

We immediately know that $\eta_1(0, t) = \eta_2(0, t) = \eta_3(0, t) = \eta_5(0, t) = 0$. Therefore the natural boundary conditions are

$$\begin{aligned} v(L, t) = 0, h(L, t) = 0, \psi'(L, t) = 0, \text{ and} \\ EAe' - [h \cos(\psi + \gamma) + v \sin(\psi + \gamma)] = 0 \text{ at } s=L. \end{aligned} \quad (\text{B.8})$$

APPENDIX C

THREE DIMENSIONAL CONTACT MODEL

The 2-D gripping contact model presented in Chapter 6 will be extended to 3-D here. As shown in Figure C.1, the compliant link has length L with its base located at the origin of the inertia frame XYZ . The undeflected direction of the link is parallel to the X axis. Each cross-section of the link has a local xyz frame attached with origin at the geometric center. The y and z axes are parallel to the principal axes of the cross-section and the x axis is normal to the cross-section. As shown in Figure C.2, we use ψ_1, ψ_2, ψ_3 as the precession, nutation and spin angles that transform inertia frame to local frame. Since each cross-section has its own local frame, these angles are functions of arc length s .

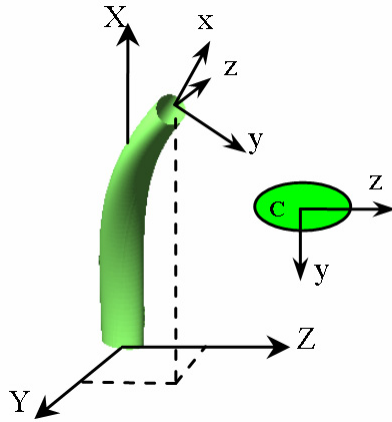


Figure C.1 Three dimensional link model

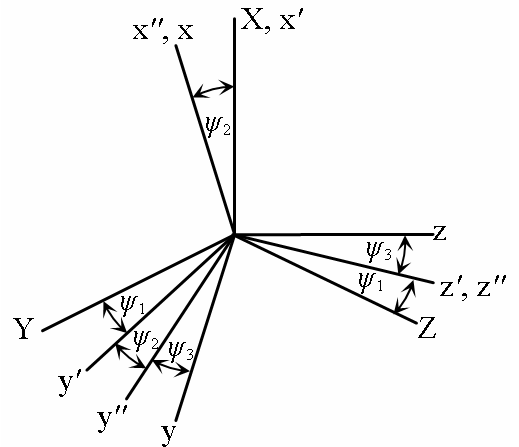


Figure C.2 XZX Eulerian angles

We denote \mathbf{R} the rotation matrix from XYZ frame to xyz frame, \mathbf{P} the position vector of the origin of xyz frame in XYZ frame. The homogenous transformation matrix

from any point in the local frame xyz to inertia frame XYZ can be expressed as

$$\mathbf{B} = \begin{bmatrix} \mathbf{R} & \mathbf{P} \\ \mathbf{0}_{1 \times 3} & 1 \end{bmatrix} = \begin{bmatrix} c_{11} & c_{12} & c_{13} & P_X \\ c_{21} & c_{22} & c_{23} & P_Y \\ c_{31} & c_{32} & c_{33} & P_Z \\ 0 & 0 & 0 & 1 \end{bmatrix}$$

where the direction cosines c_{ij} are

$$c_{11} = \cos \psi_2$$

$$c_{12} = \sin \psi_2 \cos \psi_1$$

$$c_{13} = \sin \psi_2 \sin \psi_1$$

$$c_{21} = -\sin \psi_2 \cos \psi_3$$

$$c_{22} = -\sin \psi_1 \sin \psi_3 + \cos \psi_1 \cos \psi_3 \cos \psi_2$$

$$c_{23} = \cos \psi_1 \sin \psi_3 + \sin \psi_1 \cos \psi_3 \cos \psi_2$$

$$c_{31} = \sin \psi_2 \sin \psi_3$$

$$c_{32} = -\sin \psi_1 \cos \psi_3 - \cos \psi_1 \sin \psi_3 \cos \psi_2$$

$$c_{33} = \cos \psi_1 \cos \psi_3 - \sin \psi_1 \sin \psi_3 \cos \psi_2$$

The coordinate of the point C on the neutral axis of the finger can be obtained from the following integration

$$\mathbf{P} = \begin{bmatrix} \int_0^{\hat{s}} c_{11} ds & \int_0^{\hat{s}} c_{12} ds & \int_0^{\hat{s}} c_{13} ds \end{bmatrix}^T \quad (\text{C.1})$$

where \hat{s} is the arc length from origin of XYZ to point C .

Since a 3-D compliant link can bend in y and z with twist in x direction, we need to formulate the curvature expressions κ_x κ_y κ_z for the three axes in order to formulate the strain energy function. As pointed out by Clebsch [1862], these curvatures are analogous

to the angular velocities of a rigid body with respect to XYZ by replacing time t with arc length s . Hence we can express the curvatures as in Equation (C.2).

$$\begin{aligned}\kappa_X &= \psi'_3 + \psi'_1 \cos \psi_2 \\ \kappa_Y &= \psi'_2 \sin \psi_3 - \psi'_1 \sin \psi_2 \cos \psi_3 \\ \kappa_Z &= \psi'_2 \cos \psi_3 + \psi'_1 \sin \psi_2 \sin \psi_3\end{aligned}\tag{C.2}$$

where prime denotes derivative with respect to s . By assuming superposition of strain energy holds, the total strain energy of a deformed link can be shown as

$$V = \frac{1}{2} \int_0^L \left[GA \kappa_X^2 + EI_y \kappa_Y^2 + EI_z \kappa_Z^2 \right] ds \tag{C.3}$$

where I_x is the principal moment of inertia about x and I_y is the principal moment of inertia about y. When the compliant link makes contact with a 3-D object, we have to formulate the geometric inequalities so that the link does not penetrate the object.

$$g({}_i\mathbf{p}_s) \geq 0 \tag{C.4}$$

where ${}_i\mathbf{p}_s$ is an arbitrary surface point expressed in the inertia frame and g is the 3-D surface function of the object. The vector ${}_i\mathbf{p}_s$ can be obtained from the following coordinate transformation.

$$\begin{bmatrix} {}_i\mathbf{p}_s \\ 1 \end{bmatrix} = \mathbf{B} \begin{bmatrix} {}_f\mathbf{p}_s \\ 1 \end{bmatrix}$$

where ${}_i\mathbf{p}_s$ is the surface point expressed in the local frame. Similar to the procedures in Chapter 6, the link is divided into N equally spaced elements with $\Delta s = L/N$. We use capital letters to represent approximate values of curvatures and Eulerian angles after discretization.

$$K_X^i \approx \kappa_X(s = iL / N); K_Y^i \approx \kappa_Y(s = iL / N); K_Z^i \approx \kappa_Z(s = iL / N)$$

$$\Psi_1^i = \psi_1(s = iL / N); \Psi_2^i = \psi_2(s = iL / N); \Psi_3^i = \psi_3(s = iL / N)$$

Using the above notation, Equation (C.3) can be discretized using trapezoidal rule as follows:

$$\begin{aligned} \min V \approx \frac{1}{2} \Delta s \sum_{i=1}^N & \left[G \frac{A^i (K_X^i)^2 + A^{i+1} (K_X^{i+1})^2}{2} \right. \\ & \left. + E \frac{I_y^i (K_Y^i)^2 + I_y^{i+1} (K_Y^{i+1})^2}{2} + E \frac{I_z^i (K_Z^i)^2 + I_z^{i+1} (K_Z^{i+1})^2}{2} \right] \end{aligned} \quad (C.5)$$

In order to explicitly express Equation (C.5) in terms of Eulerian angles, we also have to discretize the curvatures in Equation (C.2). Take K_X^i and K_X^{i+1} as an example; we obtain the following finite difference equations.

$$\begin{aligned} K_X^i &= \frac{\Psi_2^{i+1} - \Psi_2^i}{\Delta s} \sin \Psi_3^i - \frac{\Psi_1^{i+1} - \Psi_1^i}{\Delta s} \sin \Psi_2^i \cos \Psi_3^i \\ K_X^{i+1} &= \frac{\Psi_2^{i+1} - \Psi_2^i}{\Delta s} \sin \Psi_3^{i+1} - \frac{\Psi_1^{i+1} - \Psi_1^i}{\Delta s} \sin \Psi_2^{i+1} \cos \Psi_3^{i+1} \end{aligned}$$

Similar difference equations can be derived for K_Y^i, K_Y^{i+1}, K_Z^i , and K_Z^{i+1} . In order to obtain the finite difference form of Equation (C.4), we use trapezoidal rule again to calculate the integral of Equation (C.1) that is the position of any point on the neutral axis of the link.

$$\begin{aligned} P_{X_i} &= \sum_{j=1}^{i-1} \frac{1}{2} \left[\sin(\Psi_2^j) \cos(\Psi_1^j) + \sin(\Psi_2^{j+1}) \cos(\Psi_1^{j+1}) \right] \Delta s \\ P_{Y_i} &= \sum_{j=1}^{i-1} \frac{1}{2} \left[\sin(\Psi_2^j) \sin(\Psi_1^j) + \sin(\Psi_2^{j+1}) \sin(\Psi_1^{j+1}) \right] \Delta s \end{aligned}$$

$$P_{Z_i} = \sum_{j=0}^{i-1} \frac{1}{2} [\cos(\Psi_2^j) + \cos(\Psi_2^{j+1})] \Delta s ; \text{ and } i = 1 \sim N$$

After discretization, this turns out to be a constrained optimization problem with object function from Equation (C.5) and constrained function from Equation (C.4). By using sequential quadratic programming techniques, we can obtain the deflected shape of the link when making contact with an external object. Note that the geometric boundary conditions are

$$\Psi_1^0 = \Psi_2^0 = \Psi_3^0 = 0$$

since the link is assumed to be clamped at the base. Figure C.3 shows preliminary results of a rotating grasper (consists of five fingers) making contact with an elliptical object.

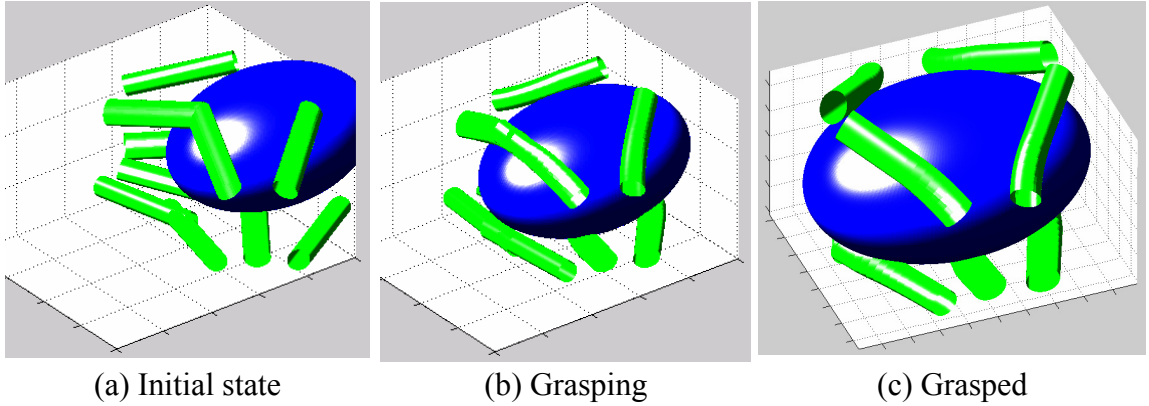


Figure C.3 Quasi-static grasping using compliant fingers

As expected, the proposed constrained optimization technique reduces the 3-D problem into a 2-D problem (we only discretize the surface only and not the entire finger). It is hoped that the proposed technique can facilitate the analysis of compliant finger grasping.

APPENDIX D

POWER SEIRES METHOD

Equation (5.1) that governs the deflected shape of a link is a set of differential equations. We presented the generalized multiple shooting method (GMSM) as the numerical solver for obtaining the deflected shape. However, the relationships between the forces (h, v) and displacements (x, y, ψ) are governed by differential equations and do not render a close form. They are not suitable for control and vibration applications. In order to explore the global coordinate model for broader applications, we propose here a power series method based on [Frisch-Fay, 1962] that turns the differential equations into close-form algebraic equations.

D.1 Formulation of Power Series Method

We consider an initially straight link with negligible shear deformation. Its governing equation is rewritten from Equation (5.1a) as follows:

$$\psi_i'' = \frac{L_i^2}{E_i I_i} (h_i \sin \psi_i - v_i \cos \psi_i) \quad (\text{D.1})$$

First we expand $\psi_i(u_i)$ into an m^{th} order Maclaurin's series as

$$\psi_i \approx \psi_i(0) + u_i \psi_i'(0) + \frac{u_i^2}{2!} \psi_i''(0) + \dots + \frac{u_i^m}{m!} \psi_i^{(m)}(0). \quad (\text{D.2})$$

Same as the GMSM, we treat the initial values $\psi_i(0)$ and $\psi_i'(0)$ as unknowns. The value $\psi_i''(0)$ can be obtained from Equation (D.1) as

$$\psi_i''(0) = \frac{L_i^2}{E_i I_i} [h_i \sin(\psi_i(0)) - v_i \cos(\psi_i(0))]$$

The initial value $\psi_i'''(0)$ is obtained by differentiating Equation (D.1) with respect to u_i .

$$\psi_i'''(0) = \frac{L_i^2}{E_i I_i} [h_i \psi_i'(0) \cos(\psi_i(0)) + v_i \psi_i'(0) \sin(\psi_i(0))]$$

Similarly, higher order initial values can be obtained as

$$\begin{aligned} \psi_i^{(4)}(0) = & \frac{L_i^2}{E_i I_i} \{h_i [\psi_i'''(0) \cos(\psi_i(0)) - 3\psi_i'(0) \psi_i''(0) \sin(\psi_i(0)) - (\psi_i'(0))^3 \cos(\psi_i(0))] \\ & + v_i [\psi_i'''(0) \sin(\psi_i(0)) + 3\psi_i'(0) \psi_i''(0) \cos(\psi_i(0)) - (\psi_i'(0))^3 \sin(\psi_i(0))]\} \end{aligned}$$

and $\psi_i^{(5)}(0) = \dots$, etc. Hence we can express ψ_i as an algebraic function of unknowns $\psi_i(0)$, $\psi_i'(0)$, h_i , and v_i . The tip location $x_i(1)$ and $y_i(1)$ are obtained using Gauss quadrature formulae:

$$\begin{aligned} x_i(1) &= x_i(0) + L_i \int_0^1 \cos \psi_i du_i = x_i(0) + L_i \int_{-1}^1 \frac{1}{2} \cos \psi_i dw \\ &\approx x_i(0) + \frac{L_i}{2} [a_1 \cos(\psi(w_1)) + a_2 \cos \psi(w_2) + \dots + a_n \cos \psi(w_n)] \\ y_i(1) &= y_i(0) + L_i \int_0^1 \sin \psi_i du_i = y_i(0) + L_i \int_{-1}^1 \frac{1}{2} \sin \psi_i dw \\ &\approx y_i(0) + \frac{L_i}{2} [a_1 \sin(\psi(w_1)) + a_2 \sin \psi(w_2) + \dots + a_n \sin \psi(w_n)] \end{aligned} \tag{D.3}$$

where $w = 2u_i - 1$; a_i 's are the weighting factors and w_i 's are the integration points. By Equations (D.2) and (D.3), we can represent the values of ψ_i , ψ_i' , x_i , and y_i at $u_i=1$ using algebraic functions that include $\psi_i(0)$, $\psi_i'(0)$, h_i , v_i , $x_i(0)$, $y_i(0)$ as unknowns. By applying these algebraic functions and unknowns into the constraint equation formulation in Chapter 5, we can analyze a compliant mechanism by solving only algebraic equations. The unknowns are identical to those formulated using GMSM.

Although we use straight links with uniform cross-sections through out the formulation, the method itself can be applied to curved links with nonuniform cross-sections as well.

D.2 Illustrative Examples

In order to illustrate the power series method, we present here three examples. The first two examples study the effect of the order of Maclaurin's series on solution accuracy using a highly deflected link. The 3rd example compares the results of the power series method with the GSM using a four-bar mechanism. In summary, we list the parameters of those examples in Table D.1.

Table D.1 Simulation parameters for the power series method

Example 1 and 2	$EI = 0.08\text{Nm}^2, L = 101.6\text{mm}$
Example 3	$EI_1=EI_3=0.3\text{Nm}^2, EI_2 \gg EI_1, L_1=L_2=L_3=25.4\text{mm}$

Example 1: Full circle bending test. We apply a moment $\lambda\pi EI / L$ at the end of a cantilever beam as shown in Figure D.1. Since the beam only undergoes moment loads at the two ends, $\psi'(s)$ must be constant within the beam. Hence the 2nd order Maclaurin's series will be enough to exactly match those calculated using GSM as shown in Figure D.1.

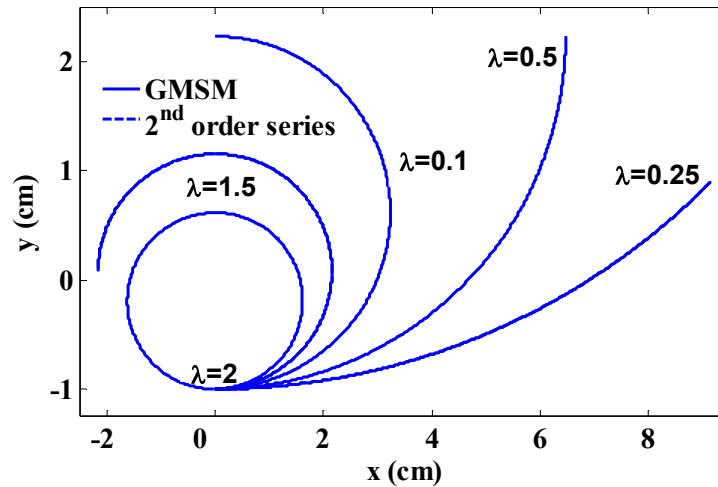


Figure D.1 Full circle bending of a cantilever beam

Example 2: A link under transverse load. The initially straight link in Figure D.2 has a displacement load δy . We compare the results of 4th and 5th order Maclaurin's series

with those obtained by GSM. The 4th order series is accurate up to $\delta y=0.6L$ while the 5th order series agrees with GSM even at very large deflection ($\delta y=0.8L$).

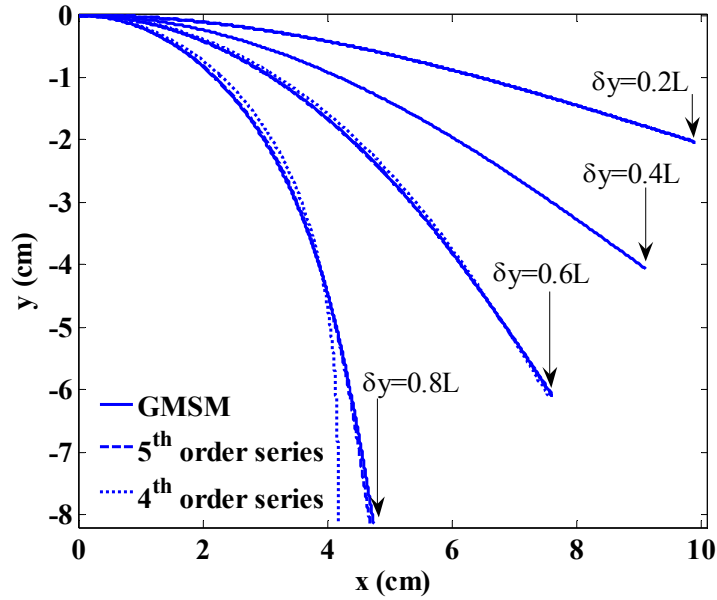


Figure D.2 A link under transverse load

Example 3: Four-bar mechanism. Consider again the four-bar mechanism shown in Figure 2.4(b). Under a δx displacement load at point A , we compare the y displacement of points A and B using GSM and the 5th order power series. As shown in Figure D.3, the results show much agreement.

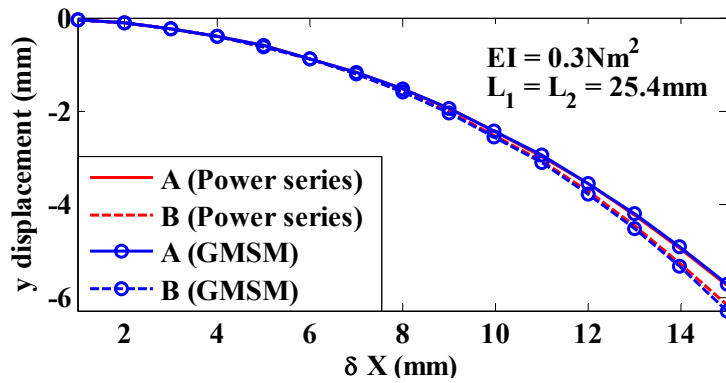


Figure D.3 Quasi-static grasping using compliant fingers

From the above three examples, it is clear that the 5th order series is accurate enough to predict the shape of a compliant mechanism.

REFERENCES

- [1] AlliedSignal Corporation, 1997, “*Modulus® Snap-Fit Design Manual*”, AlliedSignal Plastics, Morristown, NJ.
- [2] Ansel, Y., Schmitz, F., Kunz, S., Gruber, H. P., and Popovic, G., 2002, “*Development of Tools for Handling and Assembling Microcomponents*,” *Journal of Micromechanics and Microengineering*, **12**, pp.430-437.
- [3] Ascher, U. M., Mattheij, R. M. M., and Russell, R. D., 1988, *Numerical Solution of Boundary Value Problems for Ordinary Differential Equations*, Prentice-Hall, N.J.
- [4] Bar-Cohen, Y., Leary, S., Yavrouian, A., Oguro, K., Tadokoro, S., Harrison, J., Smith, J., and Su, J., 1999, “*Challenges to the Transition of IPMC Artificial Muscle Actuators to Practical Application*,” MRS Symposium, Boston, MS.
- [5] Bar-Cohen, Y., 2004, *Electroactive Polymer (EAP) Actuators as Artificial Muscles: Reality, Potential, and Challenges*, SPIE Press, Bellingham, Washington.
- [6] Bathe, K.-J., 1996, *Finite Element Procedures*, Prentice-Hall, N.J.
- [7] Bayer Corporation, 1996, “*Snap-fit Joints for Plastics, A Design Guide*”, Polymers Division, Pittsburgh, PA.
- [8] Bazaraa, M., Sherali, H., and Shetty, C., 1993, *Nonlinear Programming: Theory and Algorithms*, John Wiley & Sons, Inc.
- [9] Behdinan, K., Stylianou, M. C., and Tabarrok, B., 1998, “*Co-rotational Dynamic Analysis of Flexible Beams*,” *Computer Methods in Applied Mechanics and Engineering*, **154**, pp. 151–161.
- [10] Berry, P. S., *et al.*, 1993, “*Poultry Harvesting Assembly*,” US Patent 4,513,689, November 9.
- [11] Berzeri, M., Shabana, A. A., 2002, “*Study of the Centrifugal Stiffening Effect Using the Finite Element Absolute Nodal Coordinate Formulation*,” *Multibody System Dynamics*, **7**, pp.357-387.
- [12] Bonenberger, P. R., 2000, *The First Snap-Fit Handbook: Creating Attachments for Plastics Parts*, Hanser Gardner Publications.
- [13] Book, W. J., 1984, “*Recursive Lagrangian Dynamics of a Flexible Manipulator Arm*,” *The International Journal of Robotics Research*, **3**, pp. 87-101.
- [14] Briggs, D. V., *et al.*, 1994, “*Poultry Harvester*,” US Patent 5,325,820, July 5.
- [15] Campanelli, M., Berzeri, M., Shabana, A. A., 2000, “*Performance of the Incremental and Non-Incremental Finite Element Formulations in Flexible Multibody Problems*,” *ASME Journal of Mechanical Design*, **122**, pp. 498-507.
- [16] Clebsch, A., 1862, *Theorie der Elasticitat fester Koerper*, Leipzig.

- [17] Dechev, N., Mills, J. K., and Cleghorn, W. L., 2004, “*Mechanical Fastener Design for Use in the Microassembly of 3D Microstructures*,” ASME IMECE, Anaheim, California, USA.
- [18] Dufva, K. E., Sopanen, J. T., and Mikkola, A. M., 2005, “*A Two-dimensional Shear Deformable Beam Element Based on the Absolute Nodal Coordinate Formulation*,” *Journal of Sound and Vibration*, **280**(3-5), pp. 467-1165.
- [19] Duvant, G., Lions, J. L., 1972, *Les Inequations en Mecanique et en Physique*, Dunod, Paris.
- [20] Evans, M. S., and L. L. Howell, 1999, “*Constant-Force End-Effector Mechanism*,” IASTED Int. Conf. on Robotics and Applications, Santa Barbara, pp. 250-256.
- [21] Fichera, G., 1964, “*Problemi elastostatici con vincoli unilaterale: il problema di Signorini con ambigue condizioni al contorno*,” *Mem. Accad. Naz. Lincei, Series 8*, **7**, pp. 91.
- [22] Frisch-Fay, R., 1962, *Flexible Bars*, Butterworth, London.
- [23] Goh, C. J. and Wang, C. M., 1991, “*Generalized Shooting Method for Elastic Stability Analysis and Optimization of Structure Members*,” *Computers and Structures*, **38**(1), pp. 73-81.
- [24] Hill, T. C., and Midha, A., 1990, “*A Graphical User-Driven Newton-Raphson Technique for Use in the Analysis and Design of Compliant Mechanisms*,” *Journal of Mechanical Design, ASME*, **112**(1), pp. 123.
- [25] Hodges, D. H., 1984, “*Proper Definition of Curvature in Nonlinear Beam Kinematics*,” *AIAA Journal* **22**, pp.1825-1827.
- [26] Holsapple, R., Venkataraman, R., and Doman, D., 2003, “*A Modified Simple Shooting Method for Solving Two-Point Boundary-Value Problems*,” *IEEE Aerospace Conference*, **6**, pp. 2783-2790.
- [27] Howell, L. L., Midha, A., and Norton, T. W., 1996, “*Evaluation of Equivalent Spring Stiffness for Use in a Pseudo-Rigid-Body Model of Large-Deflection Compliant Mechanisms*,” *Journal of Mechanical Design, ASME*, **118**(1), pp. 126-131.
- [28] Howell, L. L., 2001, *Compliant Mechanisms*, John Wiley & Sons, pp. 346.
- [29] Hsiao, K. M. and Jang, J. Y., 1991, “*Dynamic Analysis of Planar Flexible Mechanism by Co-rotational Formulation*,” *Computer Methods in Applied Mechanics and Engineering*, **87**, pp. 1-14.
- [30] Huang, T. J., Brough, B., Ho, C.-M., Liu, Y., Flood, A. H., Bonvallet, P. A., Tseng, H.-R., Stoddart, J. F., Baller, M., and Magonov, S., 2004, “*A Nanomechanical Device Based on Linear Molecular Motors*,” *Applied Physics Letters*, **85**(22), pp. 5391-5393.
- [31] Javier, G. D. J., Eduardo, B., 1994, *Kinematic and Dynamic Simulation of Multibody System*, Springer-Verlag.
- [32] Johnson, K. L., 1987, *Contact Mechanics*, Cambridge Univesity Press.

- [33] Joni, H. J., 2000, "*Force Analysis of an Automated Live-bird Transfer System*," Master Dissertation, Georgia Institute of Technology.
- [34] Kalker, J. J., van Randen, Y., 1972, "*A Minimum Principle for Frictionless Elastic Contact with Application to non-Hertzian Half-space Contact Problems*," Journal of Eng. Mathematics, **6**, pp. 193.
- [35] Kane, T.R., Ryan, R.R. and Banerjee, A.K., 1987, "*Dynamics of a Cantilever Beam Attached to a Moving Base*," AIAA Journal of Guidance, Control, and Dynamics, **10**(2), pp. 139–151.
- [36] Kaneko, T., 1975, "*On Timoshenko's Correction for Shear in Vibrating Beams*," J. Phys. D: Appl. Phys., **8**, pp. 1927-1936.
- [37] Keller, H. B., 1968, *Numerical Methods for Two-Point Boundary-Value Problems*, Blaisdell publishing, Waltham, MA.
- [38] Kim, C.J., Pisano, A., and Muller, R., 1992, "*Silicon-processed Overhanging Microgripper*," Journal of Microelectromechanical Systems, **1**, pp.31-36.
- [39] Kim, C., Kota, S., 2002, "*Design of a Novel Compliant Transmission for Secondary Microactuators in Disk Drives*," ASME International Design Engineering Technical Conferences, Sept 29-Oct 2, Montreal, CA.
- [40] Kirsch, U., 1989, "*Optimal Topologies of Structures*," Applied Mechanics Reviews, **42**(8), pp. 223-239.
- [41] Laskin, R. A., Likins, P. W., Longman, R. W., 1983, "*Dynamical Equations of a Free-Free Beam Subject to Large Overall Motions*," The Journal of the Astronautical Sciences, **31**(4), pp.507-528.
- [42] Lee, K-M. and Arjunan, S., 1991, "*A Three-DOF Micro-motion In-Parallel Actuated Manipulator*," IEEE Transactions on Robotics and Automation, **7**(5), pp. 634-641.
- [43] Lee, K.-M., R. Carey, M. Lacey, and B. Webster, 1996, "*Automated Singulating System for Transfer of Live Broiler*," Proposal to US Poultry and Egg Association.
- [44] Lee, K.-M., 1999, "*On the Development of a Compliant Grasping Mechanism for On-line Handling of Live Objects, Part I: Analytical Model*," Int. Conf. on Advanced Intelligent Mechatronics Proc. (AIM'99), Atlanta, September 19-23, pp. 354-359.
- [45] Lee, K-M., 2001, "*Design Criteria for Developing an Automated Live-Bird Transfer System*," IEEE Transactions on Robotics and Automation, **17**(4), pp. 483-490.
- [46] Lee, W. H., Kang, B. H., Oh, Y. S., Stephanou, H., Sanderson, A. C., Skidmore, G., Ellis M., 2003, "*Micropeg Manipulation with a Compliant Microgripper*," IEEE Int'l Conf. on Robotics and Automation, Taipei, Taiwan.
- [47] Lobontiu, N., 2002, *Compliant Mechanisms: Design of Flexure Hinges*, CRC Press.
- [48] Maloney, J. M, Schreiber, D. S., and DeVoe, D. L, 2004, "*Large-force Electrothermal Linear Micromotors*," Journal of Micromechanics and Microengineering, **14**, pp. 226–234.

- [49] Mattiasson, K., 1981, "Numerical Results from Large Deflection Beam and Frame Problems Analyzed by Means of Elliptic Integrals," *Int. Journal for Numerical Methods in Engineering*, **17**, pp.145-153.
- [50] Mikkola, A. M. and Shabana, A. A., 2001, "A New Plate element Based on the Absolute Nodal Coordinate Formulation," ASME DETC, Pittsburgh, PA.
- [51] Monasa, F., Lewis, G., 1983, "Large Deflections of Point Loaded Cantilevers with Nonlinear Behavior," *Journal of Applied Mathematics and Physics*, **34**, pp. 395-402.
- [52] Nakabo, Yoshihiro, Mukai, T., and Asaka, K., 2005, "Kinematic Modeling and Visual Sensing of Multi-DOF Robot Manipulator with Patterned Artificial Muscle," IEEE International Conference on Robotics and Automation, Barcelona, Spain.
- [53] Newmark, N. M., 1959, "A Method of Computation for Structural Dynamics," ASCE J. of the Eng. Mechanics division, pp. 67-94.
- [54] Oh, J. S., Lewis, D. Q., Lee, D., and Gabriele, G. A., 1999, "Java™ -Based Design Calculator for Integral Snap-Fits," ASME Design Engineering Technical Conferences, Las Vegas, Nevada.
- [55] Oh, Y. S., Lee, W. H., Skidmore, G. D., 2003, "Design, Optimization, and Experiments of Compliant Microgripper," ASME IMECE, Washington, D. C.
- [56] Pai, P.F. and Palazotto, A. N., 1996, "Large-Deformation Analysis of Flexible Beams," *Int. J. of Solids and Structures*, **33**(9), pp. 1335-1353.
- [57] Paul, B., Hashemi, J., 1981, "Contact Pressure on Closely Conforming Elastic Bodies," ASME J. of Applied Mechanics, **48**, pp. 543.
- [58] Quevy, E., Bigottee, P., Collard, D., and Buchaillot, L., 2002, "Large Stroke Actuation of Continuous Membrane for Adaptive Optics by 3D Self-assembled Microplates," *Sensors and Actuators, Series A: Physical*, **95**, pp. 183-195.
- [59] Rankin, C. C. and Brogan, F. A., 1986, "An Element Independent Corotational Procedure for the Treatment of Large Rotations," ASME J. Pressure Vessel Technology, **108**, pp. 165-174.
- [60] Rao, B. N., Shastri, B. P., Rao, G. V., 1986, "Large Deflections of a Cantilever Beam Subjected to a Tip Concentrated Rational Load," *The Aeronautical Journal*, **90**, pp. 262-266.
- [61] Rao, B. N., Rao, G. V., 1989, "Large Amplitude Vibrations of a Tapered Cantilever Beam," *Journal of Sound and Vibration*, **127**(1), pp. 173-178.
- [62] Rayleigh, J. W. S., 1945, *Theory of Sound*, Vol. 1, Dover, New York.
- [63] Reddy, J. N., Singh, I. R., 1981, "Large Deflections and Large-Amplitude Free Vibrations of Straight and Curved Beams," *International Journal for Numerical Methods in Engineering*, **17**, pp. 829-852.
- [64] Reddy, J. N., 1999, *Theory and Analysis of Elastic Plates*, Taylor & Francis, Philadelphia, PA.
- [65] Reuleaux, F., 1876, *The Kinematics of Machinery*, London, Macmillan.

- [66] Shahinpoor, M., Bar-Cohen, Y., Simpson, J. O., and Smith, J., 1998, “*Ionic Polymer-metal Composites (IPMCs) as Biomimetic Sensors, Actuators and Artificial Muscles—A Review*,” *Smart Materials and Structures*, **7**, pp. R15-R30.
- [67] Salim, R., Wurmus, H., Harnisch, A., and Hulsenberg, D., 1997, “*Microgrippers created in microstructurable glass*,” *Microsystems Technology*, **4**, pp. 32-34.
- [68] Saxena, A., Ananthasuresh, G. K., 2001, “*Topology Synthesis of Compliant Mechanisms for Nonlinear Force-Deflection and Curved Path Specifications*,” *ASME Journal of Mechanical Design*, **123**, pp.33-42.
- [69] Shabana, A. A., 1996, “*Finite Element Incremental Approach and Exact Rigid Body Inertia*,” *ASME Journal of Mechanical Design*, **118**(2), pp. 171-178.
- [70] Shabana, A. A., 1998, *Dynamics of multibody systems*, Wiley, New York.
- [71] Shabana, A. A., and Yakoub, R. Y., 2001, “*Three Dimensional Absolute Nodal Coordinate Formulation for Beam Elements: Theory*,” *ASME Journal of Mechanical Design*, **123**(4), pp. 606-613.
- [72] Shampine, L. F., and Reichelt, M. W., 1997, “*The MATLAB ODE Suite*,” *SIAM Journal of Scientific Computing*, **18**, pp. 1-22.
- [73] Shampine, L. F., Reichelt, M. W., and Kierzenka, J. A., 1997, “*Solving Index-1 DAEs in MATLAB and Simulink*,” *SIAM Review*, **41**(3), pp. 538-552.
- [74] Simo, J.C., Vu-Quoc, L., 1986, “*On the Dynamics of Flexible Beams under Large Overall Motions--The Plane Case: Part I*,” *ASME Journal of Applied Mechanics*, Vol.53, pp.849-854.
- [75] Simo, J.C., Vu-Quoc, L., 1986, “*On the Dynamics of Flexible Beams under Large Overall Motions--The Plane Case: Part II*,” *ASME Journal of Applied Mechanics*, Vol.53, pp.855-863.
- [76] Stoer, J., and Bulirsch, R., 1980, *Introduction to Numerical Analysis*, pp.476-477, Springer-Verlag, New York.
- [77] Suzuki, Y., 1996, “*Flexible Microgripper and its Application to Micro-Measurement of Mechanical and Thermal Properties*,” *IEEE MEMS Proceedings 9th Annual International Workshop*, pp.406-411.
- [78] Timoshenko, S. P., 1922, “*On the Transverse Vibrations of Bars of Uniform Cross-Section*,” *Philosophical Magazine*, **43**, pp.125-131.
- [79] Tsui, K., Geisberger, A. A., Ellis, M., Skidmore, G. D., 2004, “*Micromachined End-effector and Techniques for Directed MEMS Assembly*,” *J. Micromech. Microeng.*, **14**, pp. 542-549.
- [80] Uicker, John J., Pennock, Gordon R., and Shigley, Joseph E., 2003, *Theory of Machines and Mechanisms*, 3rd Edition, Oxford University Press.
- [81] Wagner, H., 1965, “*Large-amplitude Free Vibrations of a Beam*,” *Journal of Applied Mechanics*, **32**, pp. 887-892.

- [82] Wang, C. M., and Kitipornchai, S., 1992, “*Shooting-Optimization Technique for Large Deflection Analysis of Structural Members*,” *Engineering Structures*, **14**(4), pp. 231-240.
- [83] Wallrapp, O. and Schwertassek, R., 1991, “*Representation of Geometric Stiffening in Multibody System Simulation*,” *International Journal for Numerical Methods in Engineering*, **32**, pp. 1833–1850.
- [84] Weinstock, Robert, 1974, *Calculus of Variations*, Dover Publications Inc., N.Y.
- [85] Winfrey, R. C., 1971, “*Elastic Link Mechanism Dynamics*,” *ASME Journal of Engineering for Industry*, **93**, pp. 268-272.
- [86] Wu, S.-C. and Haug, E.J., 1988, “*Geometric Non-linear Substructuring for Dynamics of Flexible Mechanical Systems*,” *International Journal for Numerical Methods in Engineering*, **26**, pp. 2211-2226.
- [87] Wu, G., Datar, R. H., Hansen, K. M., Thundat, T., Cote, R. J., and Majumdar, A., 2001, “*Bioassay of Prostate-specific Antigen (PSA) using Microcantilevers*,” *Nature Biotechnology*, **19**(9), pp. 856 – 860.
- [88] Yamakita, M., Kozuki, T., Asaka, K., and Luo, Z.-W., 2005, “*Control of Biped Walking Robot with IPMC Linear Actuator*,” *Advanced Intelligent Mechatronics*, Monterey, CA.
- [89] Yin, X., K-M. Lee, 2002, “*Modeling and Analysis of Grasping Dynamics of High Speed Transfer of Live Birds*,” 2nd IFAC Conference on Mechatronic Systems, Berkeley, CA, USA.
- [90] Yin, XueCheng, 2003, “*Modeling and Analysis of Grasping Dynamics for High Speed Transfer of Live Birds*,” Ph.D. Dissertation, Georgia Institute of Technology.
- [91] Yin, X., Lee, K.-M., and Lan, C.-C., 2004, “*Computational Models for Predicting the Deflected Shape of a Non-Uniform, Flexible Finger*,” *IEEE ICRA*, New Orleans, **3**, pp. 2963-2968.
- [92] Yoo, W.-S., Lee, J.-H., Park, S.-J., Sohn, J.-H., Dmitrochenko, O., and Pogorelov, D., 2003, “*Large Oscillations of a Thin Cantilever Beam: Physical Experiments and Simulation Using the Absolute Nodal Coordinate Formulation*,” *Nonlinear Dynamics*, **34**, pp. 3–29.
- [93] Zienkiewicz, O. C., 1977, *Finite Element Method*, McGraw-Hill, London.